

Exoplanet weather and climate regimes with clouds and thermal ionospheres

A model grid study in support of large-scale observational campaigns

Christiane Helling^{1,2,3} , Dominic Samra^{1,2} , David Lewis^{1,2} , Robb Calder², Georgina Hirst², Peter Woitke^{1,2}, Robin Baeyens⁴ , Ludmila Carone² , Oliver Herbort^{1,2,5}, and Katy L. Chubb² 

¹ Space Research Institute, Austrian Academy of Sciences, Schmiedlstrasse 6, 8042 Graz, Austria
e-mail: Christiane.Helling@oeaw.ac.at

² Centre for Exoplanet Science, School of Physics & Astronomy, University of St Andrews, North Haugh, St Andrews, KY169SS, UK

³ Institute for Theoretical Physics and Computational Physics, Graz University of Technology, Petersgasse 16/II, 8010 Graz, Austria

⁴ Institute of Astronomy, KU Leuven, Celestijnenlaan 200D, 3001 Leuven, Belgium

⁵ Institute for Astrophysics, University of Vienna, Türkenschanzstrasse 17, 1180 Vienna, Austria

Received 5 May 2022 / Accepted 10 August 2022

ABSTRACT

Context. Gaseous exoplanets are the targets that enable us to explore fundamentally our understanding of planetary physics and chemistry. With observational efforts moving from the discovery into the characterisation mode, systematic campaigns that cover large ranges of global stellar and planetary parameters will be needed to disentangle the diversity of exoplanets and their atmospheres that all are affected by their formation and evolutionary paths. Ideally, the spectral range includes the high-energy (ionisation) and the low-energy (phase-transitions) processes as they carry complementary information of the same object.

Aims. We aim to uncover cloud formation trends and globally changing chemical regimes into which gas-giant exoplanets may fall due to the host star's effect on the thermodynamic structure of their atmospheres. We aim to examine the emergence of an ionosphere as indicator for potentially asymmetric magnetic field effects on these atmospheres. We aim to provide input for exoplanet missions such as JWST, PLATO, and Ariel, as well as potential UV missions ARAGO, PolStar, or POLLUX on LUVOIR.

Methods. Pre-calculated 3D GCMs for M, K, G, F host stars are the input for our kinetic cloud model for the formation of nucleation seeds, the growth to macroscopic cloud particles and their evaporation, gravitational settling, element conservation and gas chemistry.

Results. Gaseous exoplanets fall broadly into three classes: i) cool planets with homogeneous cloud coverage, ii) intermediate temperature planets with asymmetric dayside cloud coverage, and iii) ultra-hot planets without clouds on the dayside. In class ii), the dayside cloud patterns are shaped by the wind flow and irradiation. Surface gravity and planetary rotation have little effect. For a given effective temperature, planets around K dwarfs are rotating faster compared to G dwarfs leading to larger cloud inhomogeneities in the fast rotating case. Extended atmosphere profiles suggest the formation of mineral haze in form of metal-oxide clusters (e.g. $(\text{TiO}_2)_N$).

Conclusions. The dayside cloud coverage is the tell-tale sign for the different planetary regimes and their resulting weather and climate appearance. Class (i) is representative of planets with a very homogeneous cloud particle size and material compositions across the globe (e.g., HATS-6b, NGTS-1b), classes (ii, e.g., WASP-43b, HD 209458b) and (iii, e.g., WASP-121b, WP 0137b) have a large day-night divergence of the cloud properties. The C/O ratio is, hence, homogeneously affected in class (i), but asymmetrically in class (ii) and (iii). The atmospheres of class (i) and (ii) planets are little affected by thermal ionisation, but class (iii) planets exhibit a deep ionosphere on the dayside. Magnetic coupling will therefore affect different planets differently and will be more efficient on the more extended, cloud-free dayside. How the ionosphere connects atmospheric mass loss at the top of the atmosphere with deep atmospheric layers need to be investigated to coherently interpret high resolution observations of ultra-hot planets.

Key words. planets and satellites: atmospheres – planets and satellites: gaseous planets – astrochemistry – hydrodynamics

1. Introduction

The diversity of exoplanets known so far¹ calls for concerted modelling efforts in order to optimally access the information content of the observational data. Mission concepts for deciphering rocky exoplanets and, in the ideal case, an exo-Earth (Gaudi et al. 2020; Tinetti et al. 2021; Quanz et al. 2021) are being developed and a fleet of exoplanet missions is under development at ESA² and at NASA³. The planets that can be

studied with today's observational facilities in considerable detail (i.e. atmosphere characterisation) are planets that orbit close to their host star, such as most of the known gas-giants outside the solar system. The number of directly imaged planets, i.e. those orbiting at a substantial distance from their host star, is increasing due to massive observational efforts, for example with SPHERE at the VLT (Langlois et al. 2021). Unless in discovery mode, observations will need to focus on specific objects to maximise the outcome of their instruments, for example for JWST, or future missions such as PLATO and in the UV (e.g. PolStar Scowen et al. 2022; ARAGO Neiner et al. 2019; POLLUX at LUVOIR Bouret et al. 2018). Ariel, however, will allow to observe a large ensemble of gas planets and thus to move beyond single observations towards the study of 1000

¹ <http://exoplanet.eu>

² <https://sci.esa.int/web/exoplanets>, <https://exoplanets.nasa.gov/discovery/exoplanet-catalog/>

³ <https://exoplanets.nasa.gov/exep/about/missions-instruments/>

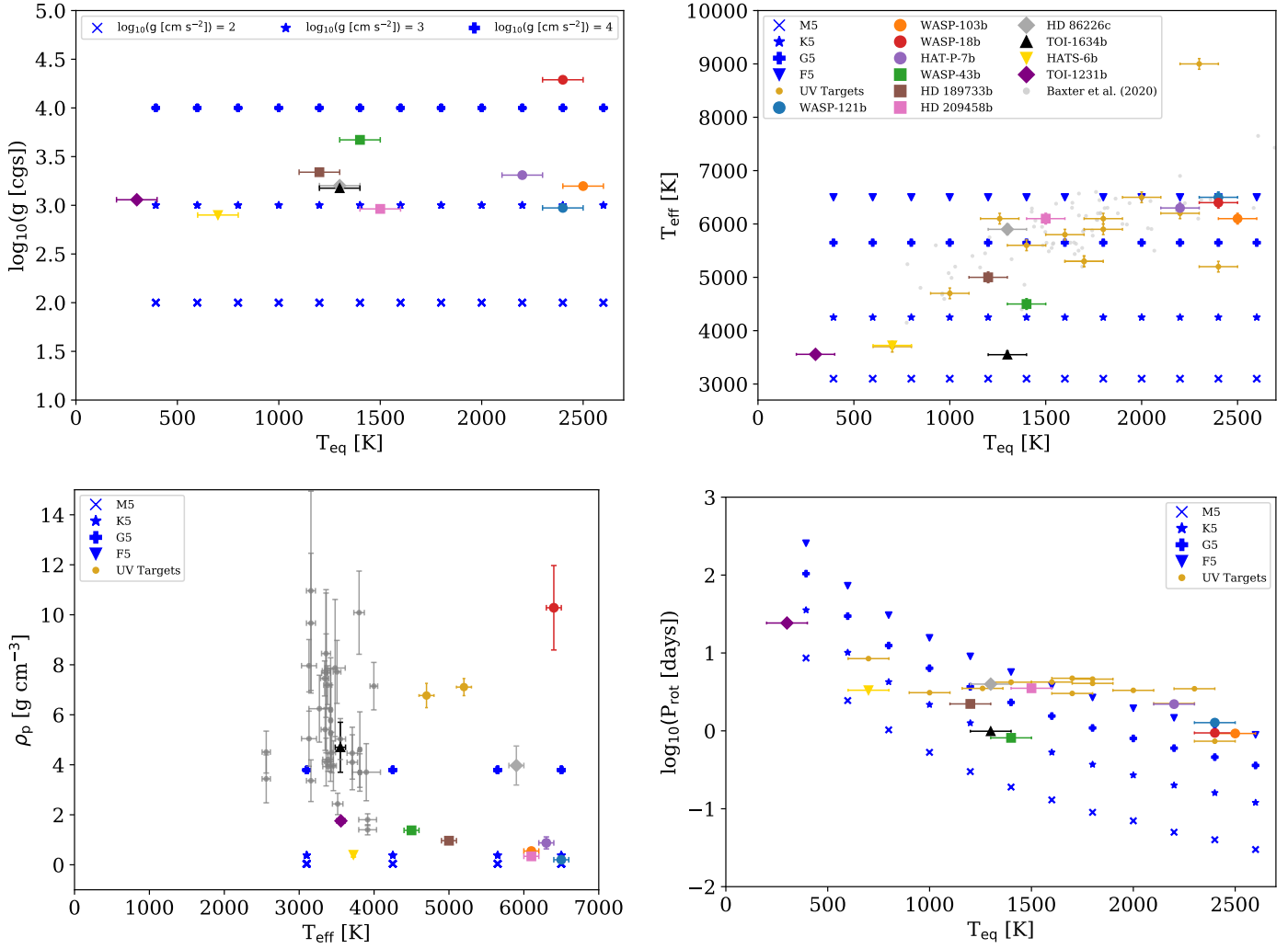


Fig. 1. System and global parameters for selected planets in comparison to the 3D GCM model grid parameter space from Baeyens et al. (2022). All model planets are tidally locked such that $P_{rot}=P_{orb}$. Selected planets include hot (WASP-43b, HD 189733b, HD 209458b) and ultra-hot (HAT-P-7b, WASP-18b, WASP-103b, WASP-121b) Jupiters, sub-Neptunes (HD 86226c, TOI-1634b), a Neptune-like planet (TOI-1231b), and a warm Saturn (HATS-6b). We also include the sample of hot and the ultra-hot Jupiters from Table 1 in Baxter et al. (2020) in the T_{eff} vs T_{eq} plot (top right) as smaller light grey points and a sample of small M dwarf orbiting planets from exoplanet.eu in the ρ_p vs T_{eff} plot (bottom left) as grey points with error bars. Potential UV targets (dark golden dots with error bars) are included for comparison (Tables C.1, C.2). The equilibrium temperature given in the literature have been rounded to the next 100 K. References: WASP-103 b: Gillon et al. (2014); WASP-121 b: Delrez et al. (2016); WASP-18 b: Hellier et al. (2009), Sheppard et al. (2017); WASP-43 b: Gillon et al. (2012); HAT-P-7 b: Van Eylen et al. (2012), Pál (2009); HD 209458 b: Torres et al. (2008); HD 189733 b: Torres et al. (2008); HD 86226 c: Teske et al. (2020); TOI-1634 b: Cloutier et al. (2021); HATS-6 b: Hartman et al. (2015); TOI-1231b: Burt et al. (2021); The rotational periods for the GCM models are taken from Baeyens et al. (2022).

transiting exoplanets and thus to comparative planetology for exoplanets. With JWST, comparative observations of several gas dominated exoplanets will be possible, for example, comparison between hot Jupiters of different equilibrium temperatures and planetary rotation orbiting K and G dwarf stars.

Modelling efforts allow to span ranges of global parameters (Parmentier et al. 2016, 2021; Baeyens et al. 2022) that are wider than what instrument target lists can afford and are therefore valuable tools to put the individually observed objects into context as demonstrated in Fig. 1. They are necessary to provide context for future ensemble studies. Questions to explore include the effect of stellar evolution on their planetary companions but also in-depth studies of the effect of host star radiation field on cloud formation and the formation of a thermal ionosphere (i.e. a region of a sufficiently high number of charges that enables plasma behaviour, for example by coupling to the ambient magnetic field; Rodríguez-Barrera et al. 2015; Helling et al. 2021b),

as well as the effect of different planetary rotation on the wind flow and thus on cloud formation. The study of cloud formation is not only key to understand the atmospheric chemistry that will be observed with space observatories such as JWST, PLATO, Ariel, LUVOIR (e.g. Min et al. 2020) but also with ground-based telescopes such as the VLT and the ELTs. Understanding cloud formation has gained further momentum due to the role that cloud particles may play in aerial biospheres (Yates et al. 2017; Seager et al. 2021).

We address the question of how cloud formation is affected by the global parameters such as planetary effective temperature and rotation period by utilizing a grid of 48 3D General Circulation Models (GCMs) that includes M, K, G and F stars as planetary host stars. Key properties, such as nucleation rate and particle sizes, are selected to study how cloud formation and the resulting global distribution of clouds change with changing global parameters of the star-planet system (global temperatures,

type of host star; Sect. 3.2). We supplement this part of our grid study by a catalogue which contains the complete set of cloud (nucleation rate, mean particles sizes, material properties, dust-to-gas ratios) and derived gas (C/O ratio, degree of ionisation, mean molecular weight) properties for all the models included in this study (Lewis et al. 2022). We follow this up by presenting integrated properties that help to discern correlated cloud property trends (Sect. 3.2). Section 4 studies three selected cases that are representative of cloud formation regimes as exoplanet tell-tale signs for weather and possible climate regimes. This specific study is followed up by addressing the effect of the outer boundary of our computational domain on our results (Sect. 5) which leads us to suggest the formation of mineral hazes in form of metal-oxide clusters in the atmospheric region of local pressure $< 10^{-8}$ bar. Section 6 presents observational implications in terms of the Transmission Spectroscopy Metric TSM, $p(\tau(\lambda) = 1)$ -levels. This paper presents all results for the planetary $\log_{10}(g [\text{cgs}]) = 3.0$. In this first cloud-grid study we focus on the interplay between 3D wind flow and temperatures for different planetary rotations and how they affect equilibrium chemistry and cloud formation. Disequilibrium chemistry will only become important for effective temperature less than 1400 K and high radiation fields. Here we address formation of mineral cloud particles from collisions dominated gases where equilibrium chemistry holds well. The C/N/O/H non-equilibrium will have little effect on our results (Helling et al. 2020).

2. Approach

2.1. 3D GCM input

We utilise the grid of 3D GCMs for tidally-locked irradiated planetary atmospheres from Baeyens et al. (2022). The grid spans host stars of spectral types M5, K5, G5 and F5, which have $T_{\text{eff}} = 3100, 4250, 5650, 6500$ K respectively, and planetary effective temperatures of $T_{\text{eff},p} = 400 \dots 2600$ K (in 200 K spacing). While the grid of Baeyens et al. (2022) also varies the gravity, the present study addresses the $\log_{10}(g [\text{cgs}]) = 3$ models only. All model planets are assumed to have the same radius of $1.35 R_{\text{Jup}}$, and a constant mean molecular weight of $\mu = 2.3$ is assumed for the atmospheric modelling.

The atmospheric circulation in the 3D climate models utilised here is driven using parametrised radiative transfer (Newtonian relaxation) towards radiative-convective equilibrium (Carone et al. 2020; Baeyens et al. 2022). As equilibrium state, chemical equilibrium abundances with solar metallicity and C/O ratio have been assumed. This Newtonian-relaxation approach results in a computationally efficient 3D model of the atmospheric circulation, which qualitatively agrees with those produced by self-consistent GCMs. As such, its use enables large grid studies of the 3D climate. For an in-depth comparison between a Newtonian-relaxed model and a GCM with self-consistent radiative coupling, see Schneider et al. (2022).

The planetary rotation is determined by its orbital period under the assumption of synchronous rotation ($P_{\text{rot}} = P_{\text{orb}}$) and ranges from $P = 0.03$ –256 days. For all except the longest orbital periods, the assumption of synchronous rotation is valid based on timescale arguments (Baeyens et al. 2022). For a given planetary equilibrium temperature, M and K dwarf planets orbit closer to their host G and F stars. As such planets around cooler stars, for example NGTS-10b (McCormac et al. 2020), HATS-6b (Hartman et al. 2015), or WASP-43b, are fast rotators, which may impact the planet’s climate. One result of fast rotation is an increased day-night temperature contrast (Carone et al. 2020;

Baeyens et al. 2022), which sets the GCMs for these planets apart from models for more typical hot Jupiter (e.g. Parmentier et al. 2018; Drummond et al. 2018; Mendonça et al. 2018). Large gas planets around M dwarfs similar to HATS-6b are rare and challenge the present understanding of planet formation (for example Kennedy & Kenyon 2008; Morales et al. 2019; Bayliss et al. 2018). Thus, such planets pose interesting targets for future characterization with JWST. The very short period corner of the parameter space may also be used to represent gas planets that orbit white dwarfs, for example WD 1856+534 b with an orbital period of 1.4 days, or brown dwarfs – white dwarfs pairs (e.g., WD 0137-349B with $P = 0.0803$ days, Lee et al. 2020).

For the grid study conducted in this paper, we extract 48 1D ($T_{\text{gas}}, p_{\text{gas}}, v(x, y, z)$) profiles per 3D GCM atmospheric model. The sampled latitudes are $\theta = 0^\circ$ (the equator) and $\theta = 45^\circ$, and the sampled longitudes span $\phi = -165^\circ$ to 180° in 15° spacing. The morning and evening terminators are given by $\phi = 270^\circ$ and $\phi = 90^\circ$ respectively.

In a small fraction of vertical temperature profiles extracted from the GCMs, spurious unphysical variations have been found, which are likely related to numerical artifacts, possibly due to the parameterized radiative forcing. Such profiles have been omitted from our cloud analysis. In the end, we included 85% of the G star profiles and 86% of the M star profiles in our investigations, as well as 100% of the 1D atmosphere profiles for the K and the F star planets.

We further note that 3D GCMs exhibit notoriously slow temperature evolution in the deep atmosphere (Carone et al. 2020; Wang & Wordsworth 2020; Schneider et al. 2022). This has largely been mitigated in the grid of Baeyens et al. (2022) by starting from a hot initial adiabatic temperature profile, but some 3D GCMs still are not fully converged for $p_{\text{gas}} > 100$ bar, leading to locally oscillating ($T_{\text{gas}}, p_{\text{gas}}$) structures in these innermost atmospheric regions. The main results in this paper will not be altered by these uncertainties since the high gas pressures do stabilise the cloud particles over a substantial temperature range at these deep atmospheric layers (see for example, Fig. 14 in Helling et al. 2021a) which sits deep in the optically thick part of the atmosphere. WASP-43b is one example where cloud formation reaches deep into these inner atmospheric regimes (Helling et al. 2021a). We include these unconverged regions nevertheless in order to explore how deep inside the atmosphere clouds could form for the different global parameters covered in our grid.

The grid’s global parameters corners. The model grid spans a large range of global parameters that has not yet been filled with existing exoplanets equivalents completely. Two corners of the grid’s parameter space are therefore pointed out that may appear as unrealistic at a first glance for the time being:

(1) Planets with $P < 35$ d can safely be assumed to be tidally locked. Longer orbital periods of tidally locked planets may occur nevertheless for older systems, for example Mercury has a period of 90 d. One should, however, expect a spin evolution for exoplanets during their migration through the planet forming disks. For example, brown dwarfs undergo a spin down evolution which may align them with planets (Scholz et al. 2018).

(2) Giant gas planets with $\log(g) = 2$ [cgs] = 100 cm s^{-2} have not been discovered so far. Nevertheless, there is a very small sub-class of objects, so-called super-puffs with very small bulk densities: for example, the Kepler-51 planets with orbital periods of 45, 85 and 130 days and with densities below 0.1 g/cm^3 (Masuda 2014; Libby-Roberts et al. 2020). While the 3D GCMs

for very low surface gravity exist, they are not included in the present cloud study.

2.2. Cloud formation and gas-phase modelling

Cloud formation has become an important piece of physico-chemistry for exoplanet research and various groups worked on understanding cloud formation in the context of atmospheric environments. Model approaches have been compared in [Helling et al. \(2008a\)](#) and within the atmosphere modelling context summarised in [Charnay et al. \(2018\)](#) and [Zhang \(2020\)](#). A discussion of the cloud formation models in the exoplanet community as well as the approach applied in the planet-forming disk community compared to the modelling approach used here can be found in the recent paper of [Samra et al. \(2022\)](#).

The local gas-phase abundances are calculated assuming chemical equilibrium by applying GGChem which is part of our cloud formation code. The gas phase is assumed to be in chemical equilibrium throughout the simulation. This, however, does not imply phase equilibrium for the condensate species considered for cloud formation. We addressed the small differences that may be imposed by kinetic gas-phase effects on the gas composition in the cloud forming regions in [Molaverdikhani et al. \(2020\)](#). Out of the total set of elements considered for the gas-phase, only 11 elements (Mg, Si, Ti, O, Fe, Al, Ca, S, K, Cl, Na) participate in the bulk growth of the cloud particles and only 6 (Ti, Si, O, K, Cl, Na) participate in the formation of cloud condensation nuclei. Within our kinetic cloud formation approach, we treat the formation of 4 nucleation species (TiO₂, SiO, KCl, NaCl) that form the cloud condensation nuclei and determine the total nucleation rate (J_* [cm⁻³ s⁻¹]). We use the modified classical nucleation theory (e.g., see [Helling & Fomins 2013](#); [Lee et al. 2018](#)) the results of which we compare for TiO₂ to a Monte Carlo approach treating individual cluster collisions ([Köhn et al. 2021](#)). The total nucleation rate determines the number of cloud particles that are forming locally and which grow to macroscopic sizes by the condensation of 16 materials through 132 gas-surface growth reactions. The cloud particle sizes are expressed as local mean cloud particle radii $\langle a \rangle$ [μm] ([Woitke & Helling 2003, 2004](#); [Helling et al. 2004, 2008b](#); [Helling & Woitke 2006](#)). For a recent review, see [Helling \(2022\)](#).

We do present our results in terms of surface averaged cloud particle radii which is more representative of their effect of the local opacity (see Sect. 3.2.2). In total, we are solving 31 ODEs in order to model the formation of cloud particles as a sequence of nucleation, surface growth/evaporation, gravitational settling, element replenishment and element conservation. The undeposited gas is assumed to be of solar composition. We have also undertaken an update of our evaporation routine. The updated modelling of the vertical mixing is described below.

2.3. Treatment of vertical mixing

Atmospheric transport processes remain challenging in combination with cloud formation modelling. Within a hydrodynamic framework, there is advective but also diffusive transport. Both components, gas and cloud particles, will move with the same velocity if the cloud particles are frictionally coupled to the gas phase. Cloud particles move with different velocities than the gas if an additional force, such as gravity, causes a frictional decoupling. Gravitational decoupling is treated as a consistent part of our kinetic cloud model ([Woitke & Helling 2003](#)). Hydrodynamic transport processes that cause a vertical transport, however, are either parameterized (e.g. [Parmentier et al. 2013](#);

[Helling et al. 2019, 2021a](#); [Steinrueck et al. 2021](#)) or derived from the hydrodynamic velocity field as described in Appendix B. In this paper, we apply two different approaches for two different domains:

(a) Within the 3D GCM computational domain ($p_{\text{gas}} > 10^{-4}$ bar): the cloud modelling within the computational domain of the whole grid of 3D models applies a different treatment of the vertical mixing source term than in previous papers ([Helling et al. 2019, 2021a](#)), calculating the standard deviation based on adjacent grid cells. The details are outlined in Appendix B. The respective mixing time scale is calculated from Eq. (B.26).

(b) Above the 3D GCM computational domain ($p_{\text{gas}} < 10^{-4}$ bar; Sect. 5): no information about the local velocity fields are available outside the computational domain of the 3D GCMs. Hence, we adopt the final value for the original non-extrapolated profile for the vertical velocity within the extrapolated regime to such that the velocity is constant. We demonstrate the validity of the hydrodynamic assumptions within the extrapolated atmosphere profiled in Appendix A. The hydrodynamic assumption would break down at $p_{\text{gas}} \approx 10^{-9}$ bar if the collisional processes within the atmospheric gas were only due to neutral molecules (here: H₂). This threshold moves to pressures as low as $p_{\text{gas}} \approx 10^{-15}$ bar if the atmospheric gas is ionised (also [Debrecht et al. 2020](#)). The increased degree of ionisation in exoplanet (and brown dwarf) atmospheres has been demonstrated in [Barth et al. \(2020\)](#) due to photochemical effects as well as due to Lyman continuum ionisation by the interstellar radiation field ([Rodríguez-Barrera et al. 2018](#)).

3. Results

The leading aim of this study is to identify global cloud formation trends (Sect. 3.2) and globally changing chemical regimes (Sect. 3.3) depending on the global parameters of the star-planet system with view of upcoming space missions such as JWST, PLATO and Ariel, but also for potential missions in the UV. The respective mission host stars are covered by the model grid that is utilised here. We concentrate on the stellar effective temperature and the orbital period as global system parameters.

The orbital period does determine the planetary effective (or global) temperature and the stellar spectral type is represented by the stellar effective temperature. An overview of the parameter range can be found in Figs. 1–3. A secondary aim is to provide a first insight regarding the potential of magnetic coupling by investigating the general trend of thermal ionisation with global parameters in comparison to the cloud location (Sect. 3.4). We hope to stimulate follow-up studies in magnetic coupling effects beyond the assumption of an ideal MH flow that assumes a constant coupling for changing thermodynamic conditions.

Our 3D grid study supports the transition found between hot and ultra-hot Jupiters for $T > 1800$ K (e.g. [Baxter et al. 2020](#); [Keating et al. 2019](#); [Showman et al. 2020](#); [Parmentier et al. 2021](#)): The dayside of ultra-hot planets are cloud-free (Fig. 3), which leads to a low bond albedo (and thus efficient dayside irradiation). Further, the day-to-nightside heat circulation is very inefficient in the 3D GCMs (see also [Perna et al. 2012](#); [Komacek et al. 2017](#)), leading to strong horizontal temperature gradients (Fig. 2). Low bond albedo at the dayside and inefficient heat circulation in combination lead to particularly large day-to-nightside emission differences. We note, however, that faster rotators, that is, the M and K dwarf planets are prone to have an even more pronounced day-to-nightside dichotomy in temperatures and cloudiness than slower rotators, that is the G and F planets. We note here that we do not have cloud-feedback on the

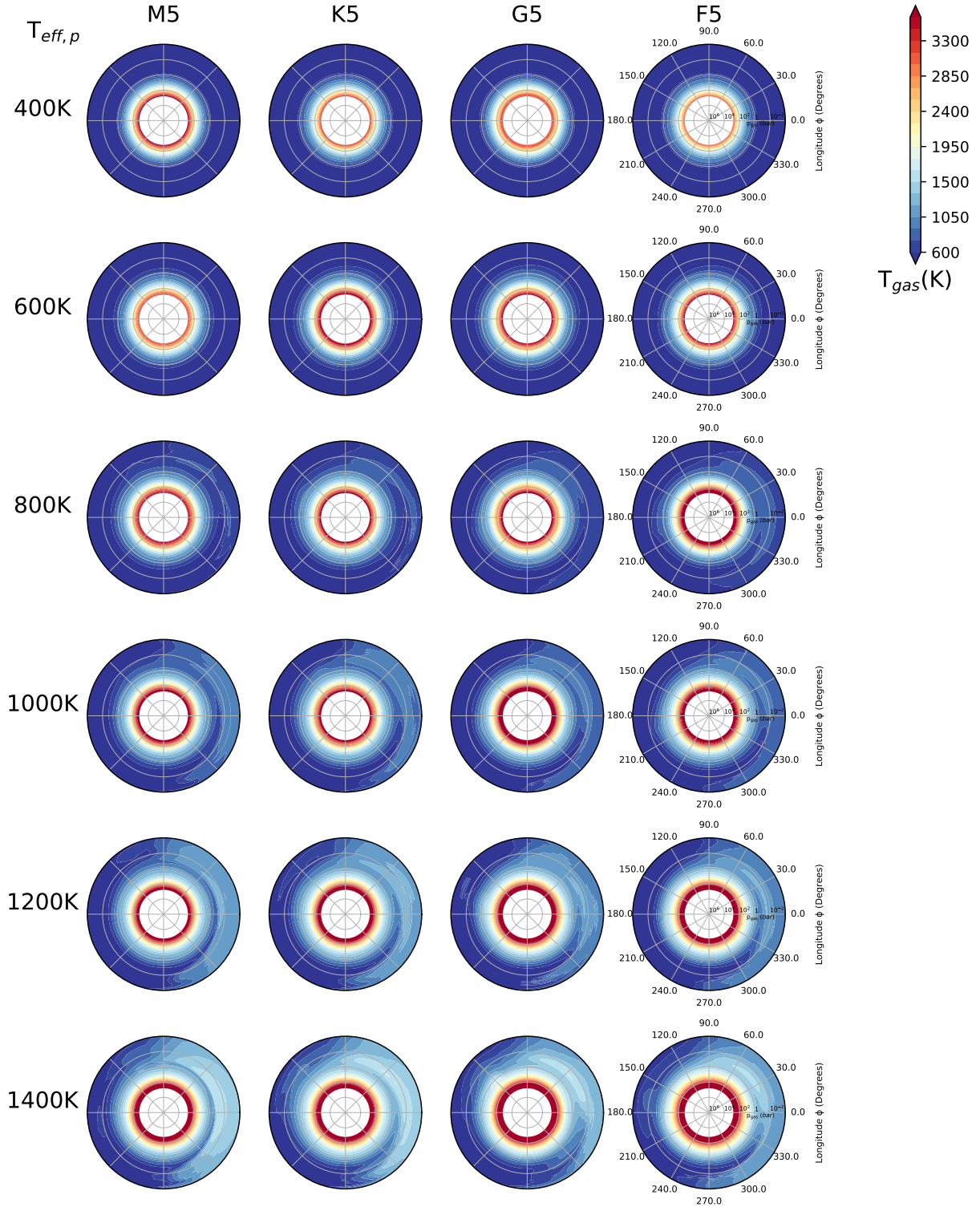


Fig. 2. Equatorial temperature maps: 2D cut through the equatorial plane ($\theta = 0^\circ$) showing the $(T_{\text{gas}}, p_{\text{gas}})$ distribution for each 3D GCM model (Baeyens et al. 2022). The planetary effective temperature ranges from $T_{\text{eff}} = 400 \dots 1400$ K shown for all stellar types and $\log_{10}(\text{g} [\text{cgs}]) = 3$.

temperatures that may lead to even less heat circulation in ultra-hot Jupiters (Parmentier et al. 2021). However, Parmentier et al. (2021) used a simpler cloud model than used in this study. A future study that will also incorporate cloud-feedback will show if this effect can be reproduced also with the microphysical cloud model. Further assumptions may alter the exact temperature threshold between hot and ultra-hot Jupiters since 3D atmosphere modelling did require further assumption to enable the

simulations. One such assumption is the mean molecular weight which we address in Sect. 3.3.2.

3.1. Host star trends of planetary $(T_{\text{gas}}, p_{\text{gas}})$ -structures

A summary of the change in the 3D $(T_{\text{gas}}, p_{\text{gas}})$ -structures demonstrates first trends that will translate into trends in the global cloud structure of these planetary atmospheres. A detailed

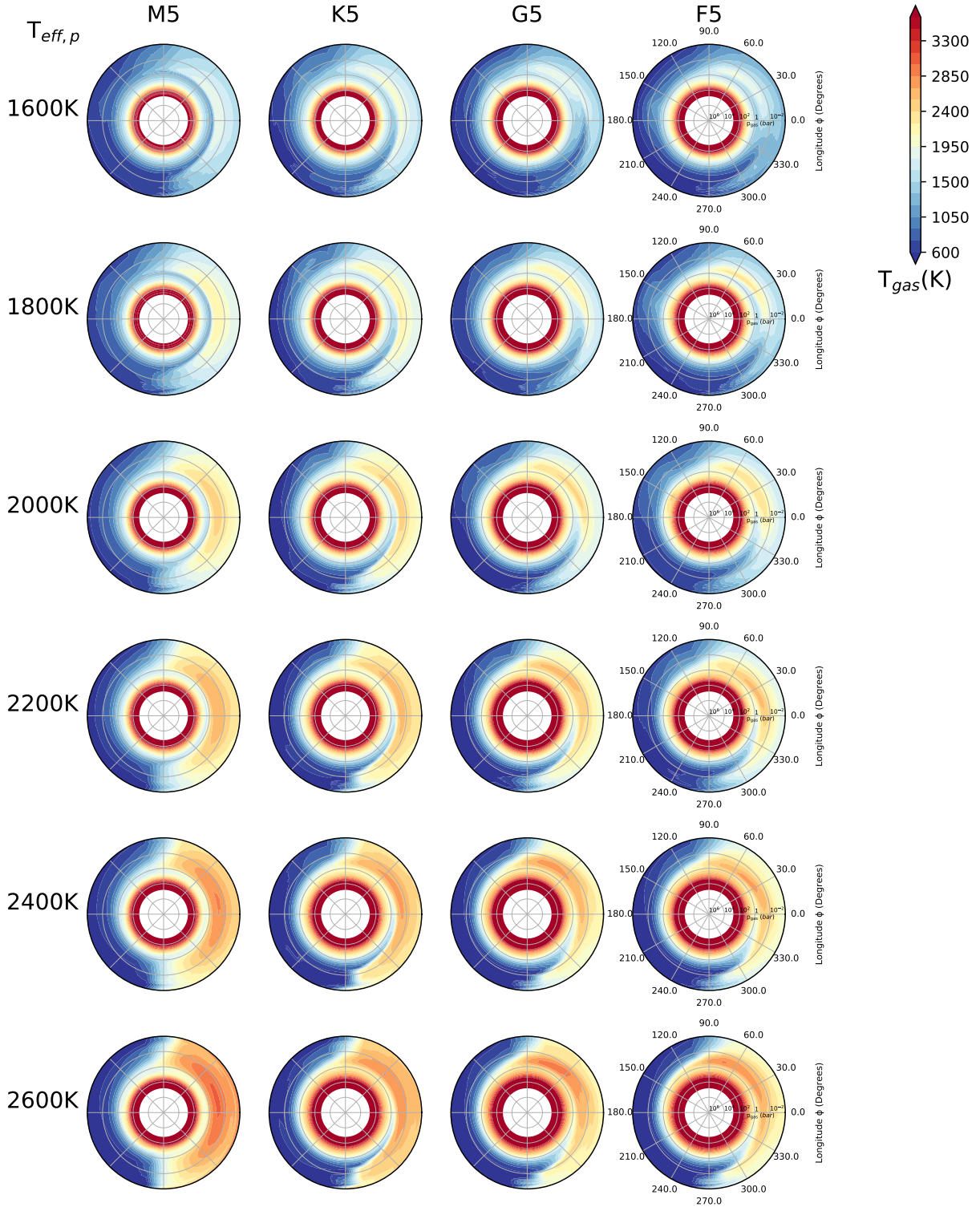


Fig. 3. Equatorial temperature maps: 2D cut through the equatorial plane ($\theta = 0^\circ$) showing the (T_{gas} , p_{gas}) distribution for each 3D GCM model (Baeyens et al. 2022). The planetary effective temperature ranges from $T_{\text{eff}} = 1600 \dots 2600$ K for all stellar types and $\log_{10}(g [\text{cgs}]) = 3$.

analysis is presented in Baeyens et al. (2022) and we focus on global trends only. Figures 2 and 3 show the thermal structure of the equatorial plane ($\theta = 0^\circ$) for all the $\log(g) = 3$ [cgs] models, and how the local atmosphere temperature changes when the planet orbits closer to its host star (increasing $T_{\text{eff,P}}$).

All models with $T_{\text{eff,P}} \leq 800$ K have a horizontally/zonally/longitudinally homogeneous temperature distribution. The

day-night asymmetry emerges at $T_{\text{eff,P}} = 800$ K and is more pronounced for the faster rotating stellar types. For hotter planets ($T_{\text{eff,P}} \geq 1600$ K), advection of cooler air from the nightside onto the dayside can be seen, extending across the evening terminator at 1 bar. This structure is more extended for the F and the G star models, and it does not appear at all for the M star planets. The JWST targets NGTS-10b, HD 209458b

(pink square, Fig. 1), HD 189733b (brown square) and WASP-63b have equilibrium temperature between 1200 K and 1600 K orbiting G and K stars, hence represent the transitional regime from homogeneous temperature distributions to pronounced day-night temperature differences (e.g. HAT-P-7b (purple filled circle)) in the 3D GCM grid utilized here. The super-Saturn HATS-6b (yellow triangle) that orbits an M1V host star ($d = 148.4(\pm 3.3)$ pc) at a distance of $a = 0.03623$ AU with a period of $P = 3.325$ d ($M_P = 0.319 M_{\text{Jup}}$, $R_P = 0.998 R_{\text{Jup}}$) would be represented by the model of $T_{\text{eff,P}} = 600$ K, $g = 10$ m s⁻¹ and M-type host star. A homogeneous temperature structure can, hence, be expected for HATS-6b.

3.2. Cloud regimes with changing global system parameters

The formation of clouds is triggered by a gas-phase transition leading to the formation of newly formed cloud condensation nuclei (nucleation), unless meteoritic dust re-condenses or the planet under consideration has a rocky surface from which sand particles are transported into the atmosphere. The chemical processes that lead the nucleation process are only partially known (e.g., Köhn et al. 2021 and references therein) and extensive studies are ongoing. The nucleation process is key to where clouds can form and it is determined by the local thermodynamic conditions. It is therefore important to be able to determine where in the atmosphere nucleation occurs with which efficiency as this is already indicative for changing cloud regimes with changing global stellar-planetary parameters (Sect. 3.2.1). The nucleation rate determines the number of cloud particles that eventually make up the whole cloud (and their distribution), hence, it also influences the size of the cloud particles. Due to element conservation (mass conservation), it is reasonable to generally expect large cloud particles in regions of low nucleation efficiency (Sect. 3.2.2).

3.2.1. The formation of cloud condensation nuclei

The total nucleation rate indicates the efficiency at which nucleation seeds form spontaneously from the gas phase, and is therefore used to identify the cloud formation regime. We consider here the nucleation of four species: TiO₂, SiO, KCl, NaCl. We calculate the total nucleation rate as $J_{*,\text{tot}} = \sum J_{*,i}$ ($i = \text{TiO}_2, \text{SiO}, \text{KCl}, \text{NaCl}$). The equatorial distribution of the total nucleation rate is presented for all models with $\log(g) = 3$ [cgs] in Figs. 4, 5.

There are crudely two nucleation regimes: one where nucleation occurs throughout the whole atmosphere across the whole globe ($T_{\text{eff,P}} \leq 1200$ K), the globally homogeneous nucleation regime, and one where nucleation occurs intermittently or asymmetrically distributed in the atmosphere ($T_{\text{eff,P}} > 1200$ K), the partial nucleation regime.

The lowest global temperature corner of the globally homogeneous nucleation regime is characterised by an extremely efficient nucleation process. In the upper atmosphere of the $T_{\text{eff,P}} = 400$ K model the total nucleation has an initial value of approximately 10^{-3} cm⁻³ s⁻¹ which rises to a peak of 10^3 cm⁻³ s⁻¹ by $p_{\text{gas}} = 10^{-2}$ bar. This is due to the delayed onset of SiO nucleation, which begins at 10^{-3} bar and dominates significantly over the TiO₂ nucleation between $10^{-2.5}$ bar and $10^{-0.5}$ bar. In the deep atmosphere at pressures greater than $p_{\text{gas}} = 10^{-0.5}$ bar the efficiency of the SiO nucleation decreases such that TiO₂ becomes the dominant nucleation species.

Nucleation occurs across almost the entire equatorial plane for the models $T_{\text{eff,P}} \leq 1200$ K, with the dayside nucleation

generally reduced compared to the nightside with a strong day-night asymmetry emerging with increasing planetary temperature. This asymmetry becomes most apparent in the models with $T_{\text{eff,P}} \geq 1400$ K where regions of the dayside atmosphere do not exhibit nucleation. The extent of the dayside atmosphere where nucleation is not possible increases with the global planetary temperature $T_{\text{eff,P}}$, starting east of the substellar point and varies in size between the four stellar types M, K, G and F. The size of the decreased nucleation region on the dayside is larger for the faster rotating planets at a given temperature, i.e. largest for the M star and smallest for the F stars. The location of this dayside reduction in nucleation coincides with the temperature hot spot which is offset from the substellar point due to the equatorial jet. Nucleation still occurs on the dayside of these hotter models, however, this only occurs where cool air has been carried across the morning terminator by the jet. In hotter planetary atmospheres, the radiative response becomes shorter and cold air is efficiently heated as it reaches the dayside. For $T_{\text{eff,P}} \geq 2000$ K there is essentially no nucleation on the dayside of the M star orbiting planets, and the extension of the nucleation across the morning terminator is similar for the K, G and F stars. The nucleation rate will not only be affected by the global planetary temperature but also by the gravity which determines the density structure of the atmosphere. Higher gravity will shift the nucleation emergence towards higher temperature due to an increased thermal stability as result of a higher collision rate for increased gas densities.

To enable the comparison of the nucleation efficiency across the whole grid of global parameters, column integrated values are considered. We note that the integration column does vary for different planetary atmospheres due to the varying cloud extension as result of the local thermodynamic conditions (e.g. Fig. 16).

Figure 6 shows the column integrated total nucleation rate for each of the model planets for each stellar type to allow for a comparison of nucleation activity across the whole 3D GCM grid. The range of values for the column integrated nucleation rates is very narrow for both the $T_{\text{eff,P}} = 400$ K ($\sim 10^8$ – 10^{10} cm⁻² s⁻¹) and $T_{\text{eff,P}} = 600$ K ($\sim 10^6$ – 10^{10} cm⁻² s⁻¹) models for all stellar types. For warmer models the range in values widens and the divide between dayside and nightside becomes more apparent. The range of values is larger for the M and K stars ($\sim 10^3$ – 10^{10} cm⁻² s⁻¹) compared to the G and F stars ($\sim 10^5$ – 10^{10} cm⁻² s⁻¹) for planetary effective temperatures $T_{\text{eff,P}} = 800$ – 1200 K. The small spread of values is representative for the globally homogeneous nucleation regime where the formation of cloud condensation nuclei is most efficient and possible across the globe. For models $T_{\text{eff,P}} = 1400, 1600, 1800$ K that range increases slightly and again separation between day and nightside becomes clearer and it is apparent that nucleation is less efficient for the higher $\theta = 45^\circ$ latitude compared to the equator for these models. Such a spread in values is representative for the partial nucleation regime, the largest spread will represent the atmospheres with the largest cloud formation asymmetry. The largest thermodynamic, and hence, nucleation asymmetry occurs for $T_{\text{eff,P}} \geq 2000$ K.

For all models the spread of values for the column integrated total nucleation rate is smaller for the nightside than the dayside. This is a reflection of the homogeneous local gas temperature of the nightside, whereas there is more variation in the temperatures on the dayside. The range of values on the dayside is reasonably consistent at $\sim 10^{-13}$ – 10^5 cm⁻² s⁻¹ for the $T_{\text{eff,P}} = 1400, 1600$ K models, and there is still significant overlap between the day and nightside values. A ‘cone’ of diverging integrated nucleation

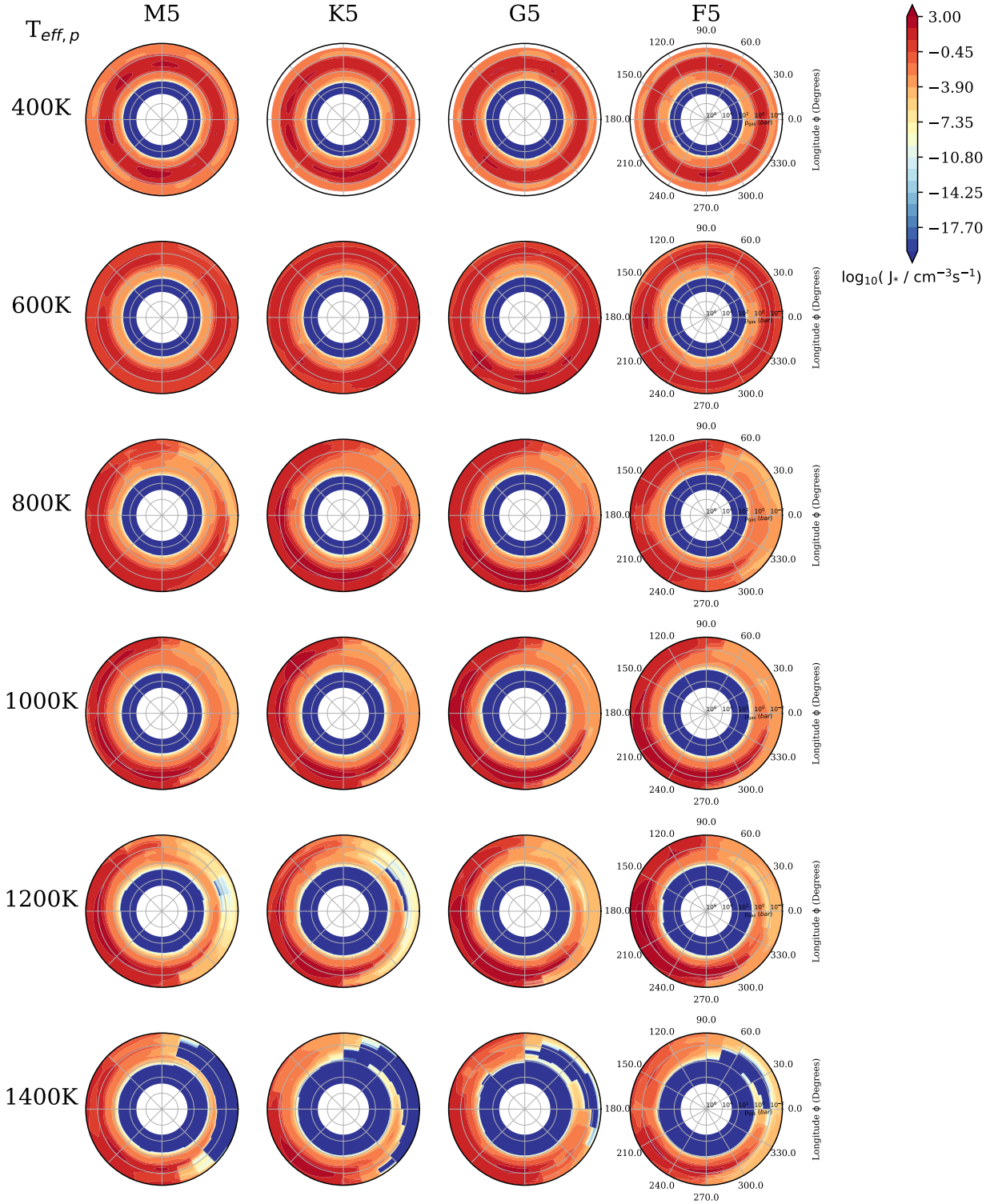


Fig. 4. Total nucleation rate, $J_* = \sum_i J_i$ [$\text{cm}^{-3} \text{s}^{-1}$], $i = \text{TiO}_2, \text{SiO}, \text{NaCl}, \text{KCl}$, in the 2D equatorial plane ($\theta = 0^\circ$) for the 1D profiles extracted from the 3D GCM models for $\log_{10} g = 3$ [cgs]. The same cold model atmospheres similar to Fig. 2 are depicted. In this grid, the $T_{\text{eff},p} = 1400$ K orbiting an K or G star is representative of NGTS-10b/WASP-43b and HD 209458b respectively. The $T_{\text{eff},p} = 1200$ K orbiting the K dwarf may represent HD 189733b, $T_{\text{eff},p} = 1600$ K orbiting the K star for WASP-63b.

rates emerges as function of the stellar effective temperature where the upper limit of integrated nucleation rate remains roughly similar ($10^{10} \text{cm}^{-2} \text{s}^{-1}$). A ‘bifurcation’ occurs at the hotter end $T_{\text{eff},p} > 1400$ K, most clear for the M5 host star, where there is a clear separation between the dayside and nightside nucleation efficiency.

We conclude that no one value of nucleation rate is sufficient to describe the first step for cloud formation in exoplanet atmospheres. Only for the coolest atmospheres one might describe the nucleation rate reasonably by one value. Here, the [Ackerman & Marley \(2001\)](#) model may well be suited to speed up GCM efficiency.

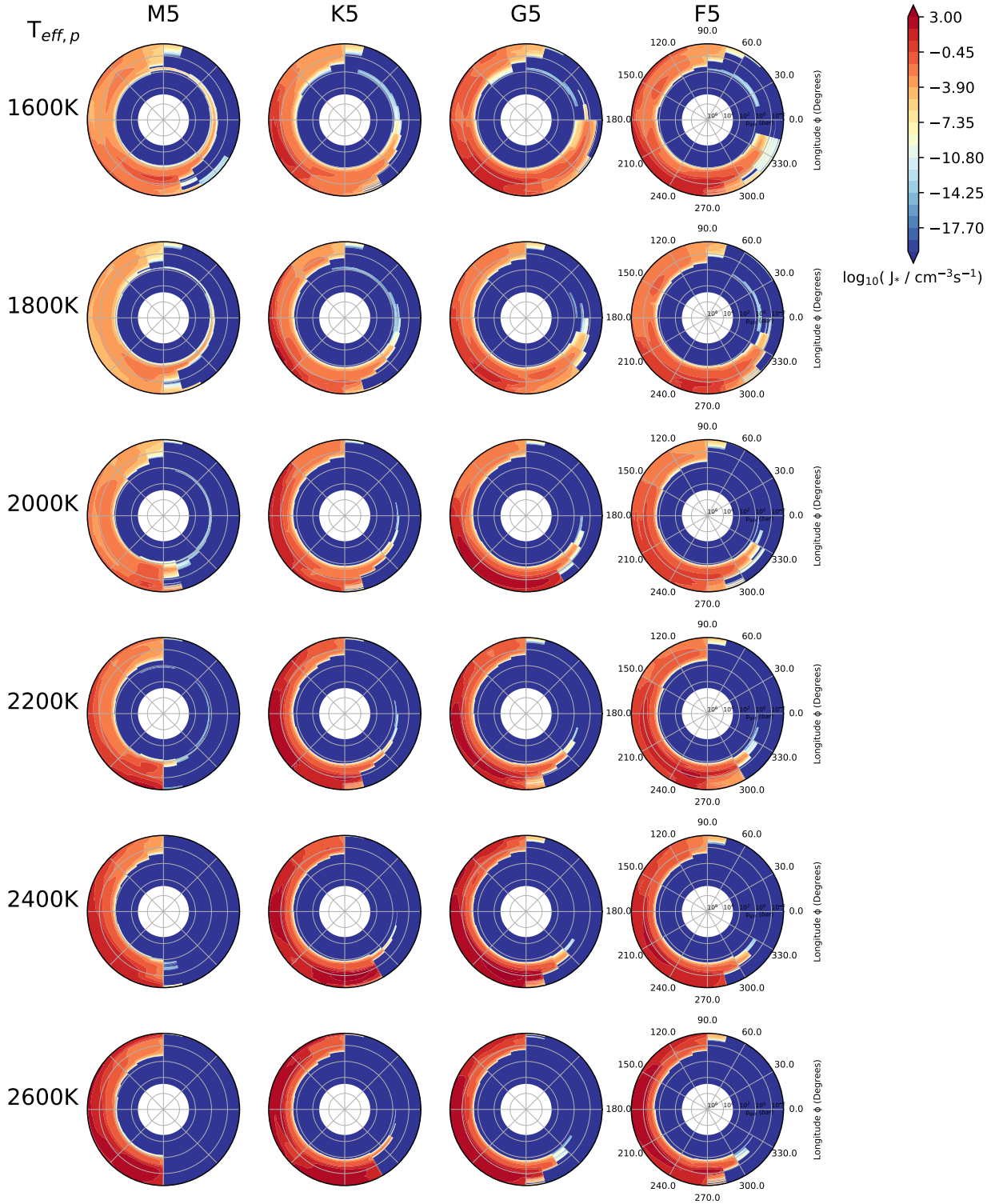


Fig. 5. Total nucleation rate, $J_* = \sum_i J_i$ [$\text{cm}^{-3}\text{s}^{-1}$], $i = \text{TiO}_2, \text{SiO}, \text{NaCl}, \text{KCl}$, in the 2D equatorial plane ($\theta = 0^\circ$) for the 1D profiles extracted from the 3D GCM models for $\log_{10}g = 3$ [cgs]. The same warm model atmospheres similar to Fig. 3 are depicted.

3.2.2. Mean particle size and dust-to-gas ratio

Cloud particles sizes are essential to calculate the cloud opacity and are often seen as observationally accessible test of cloud properties and of cloud models, for example Griffith et al. (1998); Marley et al. (2002); Cushing et al. (2006); Lee et al. (2013); Hiranaka et al. (2016); Benneke et al. (2019); Lacy & Burrows (2020). We re-iterate previous results of that exoplanet

and brown dwarf clouds cannot be characterised by one particle size only (Helling & Woitke 2006; Helling et al. 2017; Helling 2019a). Here, however, the focus is on potential trends that might serve as input for automated retrieval efforts. We therefore chose to represent the mean cloud particle size in terms of surfaced averaged mean particle size, $\langle a \rangle_A$. The dust-to-gas ratio is a helpful property to locate the cloud mass

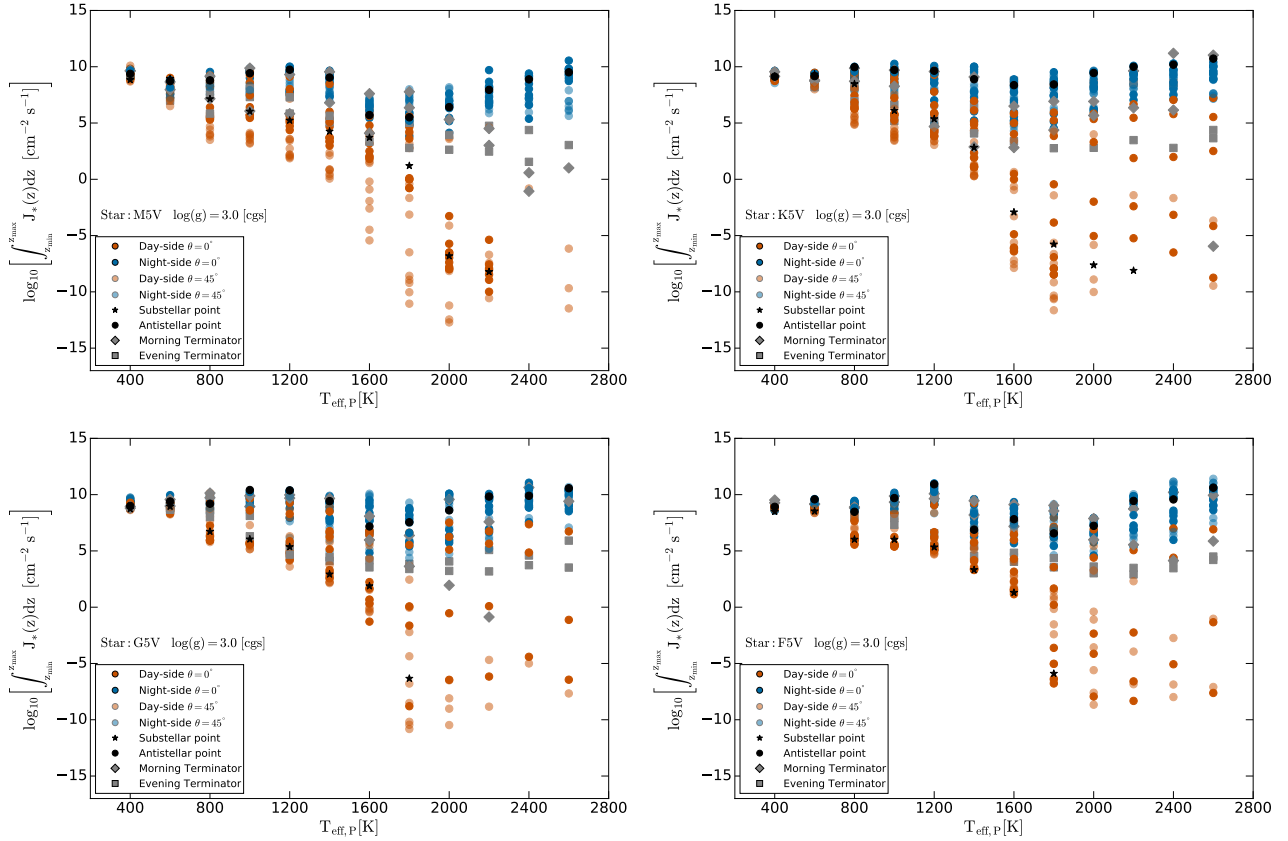


Fig. 6. Column-integrated nucleation rates for the $\log(g) = 3$ [cgs] grid models and different stellar types. No one value suffices to describe the rate at which cloud particles form. At approximately 1600 K or 1800 K, the overall spread is much larger for all host stars.

load and to compare to other astrophysical objects where condensation processes take place (e.g. AGB stars, Wolf-Rayet stars, SNs).

The surfaced averaged mean particle size, $\langle a \rangle_A$ [cm], is

$$\langle a \rangle_A = \sqrt[3]{\frac{3}{4\pi} \frac{L_3}{L_2}}, \quad (1)$$

with L_2 and L_3 the second and third dust moments (Eq. (A.1) in Helling et al. 2020). Further discussion of the mean particle size and the differing definitions can be found in Appendix A of Helling et al. (2020). The column integrated, number density weighted, surface averaged mean particle size is

$$\langle \langle a \rangle_A \rangle = \frac{\int_{z_{\min}}^{z_{\max}} n_d(z) \langle a \rangle_A(z) dz}{\int_{z_{\min}}^{z_{\max}} n_d(z) dz} \quad \text{with} \quad n_d(z) = \frac{\rho(z) L_3(z)}{4\pi \langle a(z) \rangle_A^3 / 3}. \quad (2)$$

The column-integrated properties are used to compare the cloud particle size within the grid of 3D GCM model atmospheres.

All detailed results for $\langle a \rangle_A$ as well as for the dust-to-gas ratio, ρ_d/ρ_{gas} , are provided in the supplementary catalogue (Lewis et al. 2022). A summary is given here as link for the understanding of the column integrated plots as well as for the comparison with the degree of thermal ionisation in Sect. 3.4.

The surfaced averaged mean particle size, $\langle a \rangle_A$, range from $10^{-2} \mu\text{m}$ to $\approx 10^4 \mu\text{m}$. The largest particle sizes correlate with either low nucleation rates (in hot planetary atmospheres) or very high local densities (inside the planetary atmospheres). The local cloud particle distribution covers a larger volume of the

planetary atmosphere than the nucleation rate due to transport processes such as gravitational settling.

For all models with $T_{\text{eff,P}} \geq 800$ K, cloud particles on the dayside, where they exist, are on average larger than that of the nightside by 2–3 orders of magnitude. Cloud particles are generally not found on the dayside for models with $T_{\text{eff,P}} \geq 2000$, except where the deep equatorial jet permits some cloud formation at 10^{-2} bar.

Figure 7 shows the global distribution of the average particle sizes in terms of their column integrated, number density weighted values. The results complement the nucleation rate results in Fig. 6: In regions of low nucleation efficiency the average particle sizes are large. The range of integrated average particle sizes spans several orders of magnitude $\langle \langle a \rangle_A \rangle \sim 10^{-3} - 10^5 \mu\text{m}$. The distribution follows the same ‘cone’ like divergence structure of the average dayside particle size compared to the nightside which are consistently in the range $10^{-3} - 10^{-1} \mu\text{m}$.

For the colder models, the dust-to-gas mass ratio (Figs. 7 and 8 in the supplementary catalogue in Lewis et al. 2022) is lower across the dayside, especially near the morning terminator, hence, demonstrating the lower cloud formation efficiency in these atmospheric regions. For models with $T_{\text{eff,P}} \geq 1600$ K, the dayside cloud formation is limited to the morning terminator regions on the dayside. This layer of cloud formation is more extended in the pressure scale for the slower rotators. As the planetary effective temperature increases, this structure reduces in size until there is only limited dayside cloud formation near the evening terminator for the slower rotators and none whatsoever for the M star model. There are also inversions in the dust to gas mass ratio for the M star models with $T_{\text{eff,P}} = 1600 \text{ K} - 2000 \text{ K}$

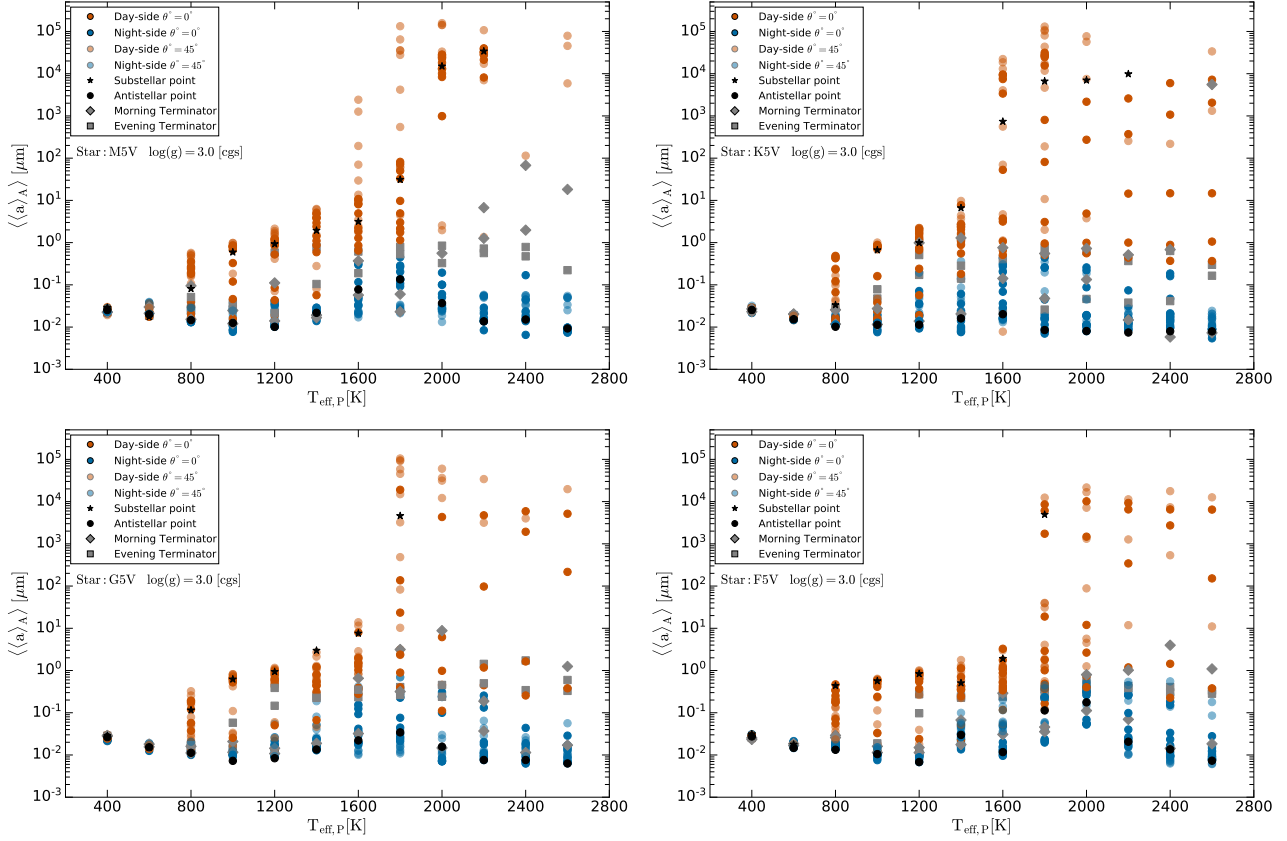


Fig. 7. Column integrated, number density weighted surface averaged mean particle size, $\langle\langle a \rangle_A\rangle$ [μm], for the $\log(g) = 3$ [cgs] grid models and different stellar types.

3.2.3. Material composition of cloud particles

Another property used to characterise cloud particles is the material composition of the cloud particles. It has been stated elsewhere that cloud particles change their material composition throughout their life time if they get transported into atmospheric regions of different thermodynamic conditions (for example, Helling & Woitke 2006; Helling et al. 2017; Helling 2019a). The global distribution of the individual materials for the whole 3D grid that we address here is included in the supplementary catalogue (Lewis et al. 2022). Here, we explore the material composition of the cloud particles which form in the atmosphere in terms of material groups. The bulk growth of 16 condensate species is considered here, and for the purpose of extracting trends in types of material condensate, similarly to Helling et al. (2021a), we split the condensates into four groups: high temperature condensates, metal oxides, silicates, and salts. The condensate species included and the group they are assigned to are shown in Table 1. We choose to focus here on a comparison between the M and G stellar type models, with further discussion on the K and F stellar types and the equatorial distribution of material composition in Lewis et al. (2022).

Figure 8 shows the normalised column integrated volume fractions with s is a particular condensate species group,

$$\langle V \rangle_{\text{norm}} = \frac{\int_{z_{\text{min}}}^{z_{\text{max}}} \frac{V_s(z)}{V_{\text{tot}}(z)} dz}{\sum_i \int_{z_{\text{min}}}^{z_{\text{max}}} \frac{V_i(z)}{V_{\text{tot}}(z)} dz}, \quad (3)$$

and i runs through all the condensate species groups (Table 1), with the integrated, number density weighted, surface averaged

Table 1. Bulk materials considered in our model are grouped in 4 categories.

Condensate group	Species included
Metal oxides	SiO[s], SiO ₂ [s], MgO[s], FeO[s], Fe ₂ O ₃ [s]
Silicates	MgSiO ₃ [s], Mg ₂ SiO ₄ [s], CaSiO ₃ [s], Fe ₂ SiO ₄ [s]
High temperature Condensates	TiO ₂ [s], Fe[s], Al ₂ O ₃ [s], CaTiO ₃ [s], FeS[s]
Salts	KCl[s], NaCl[s]

Notes. [s] indicates condensate materials.

mean particle size (Eq. (2)) for the substellar, antistellar, equatorial morning and evening terminator of the models with M and G stellar type host stars.

The antistellar points for both the M and G star are similar with small cloud particles ($\langle\langle a \rangle_A\rangle \sim 10^{-2}$ – 10^{-1} μm) which are dominated in composition by silicates (~ 40 – 50%) forming for all model planets. The remaining volume is approximately equally distributed between the high temperature condensates and metal oxides (each ~ 20 – 25%). This is similarly the case for the morning terminator, excepting the highest temperature models, $T_{\text{eff}} \geq 1800$ K, planets orbiting the M5V star where the silicates comprise ~ 55 – 60% of the total volume, and the high temperature condensates dominate over the metal oxides by more than 10% . The highest temperature model where clouds form for the M star, $T_{\text{eff}} = 2400$ K, has high temperature condensates

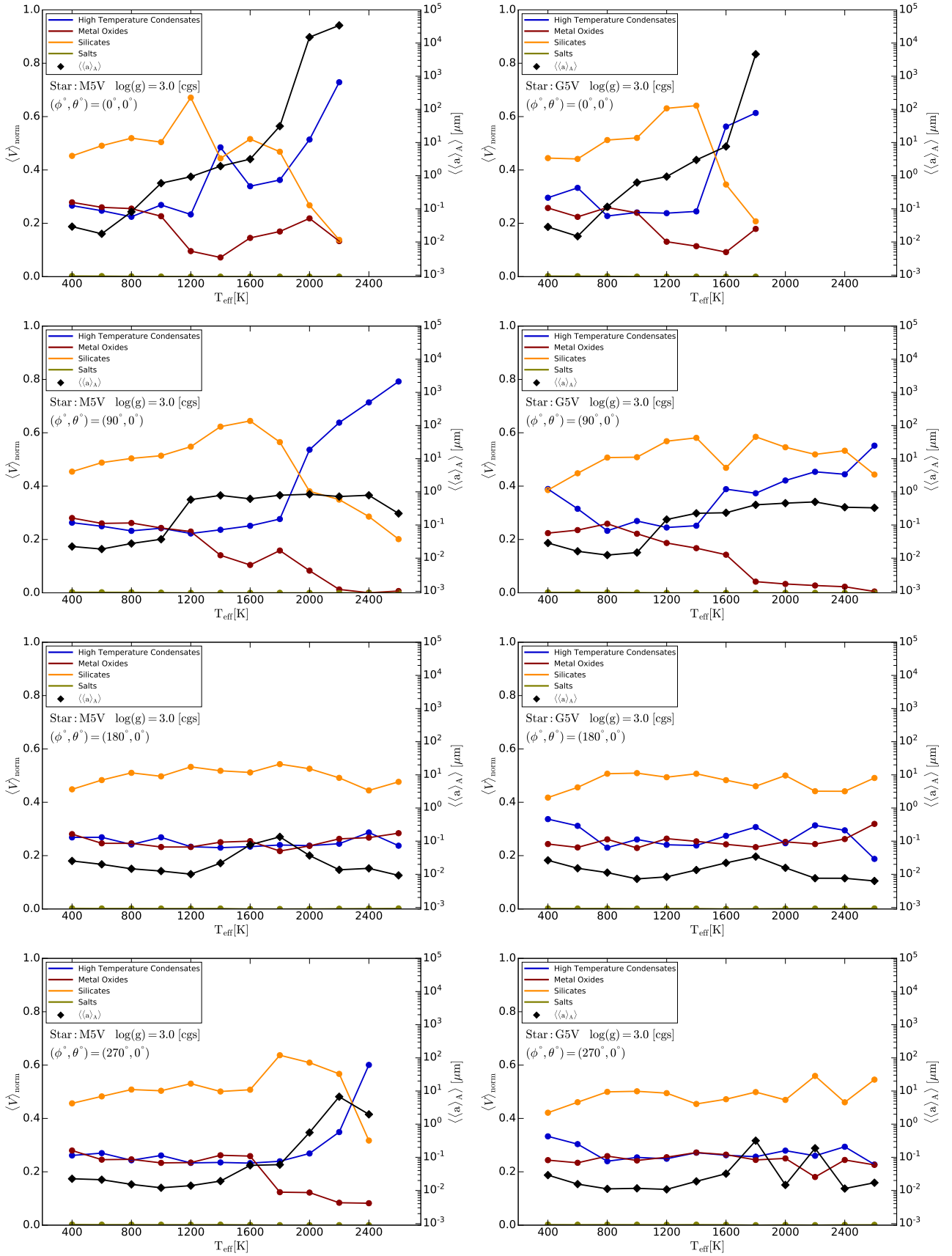


Fig. 8. Normalised column integrated volume fractions and integrated number density weighted surface averaged mean particle size for the sub-stellar point (first row), equatorial evening terminator (second row), antistellar point (third row), and equatorial morning terminator (fourth row) for the M (left) and G (right) stellar types.

as the largest contributor to the cloud particle load by volume at $\sim 60\%$, with the remaining volume comprised of silicates ($\sim 35\%$) and metal oxides ($\sim 5\%$). The average value for $\langle\langle a \rangle_A\rangle$ increases gradually with increasing planet temperature for the M star planets, compared to an almost consistently small particle size for the G star.

At the substellar point the coolest planets exhibit a similar pattern of material composition as is found at the antistellar and morning terminator points, however, the range of values for the integrated number density weighted surface averaged mean particle size is larger here, $\langle\langle a \rangle_A\rangle \sim 10^{-2} - 10^0 \mu\text{m}$. For the hottest temperature planets (M: $T_{\text{eff}} \geq 1800 \text{ K}$, G: $T_{\text{eff}} = 1800 \text{ K}$) there are temperature inversions between $p_{\text{gas}} = 10^{-1} \dots 10^{0.5-1} \text{ bar}$ which are sufficiently large to reduce the temperature such that TiO nucleation can occur and the supersaturation ratios of certain material condensates are large, $S \gg 1$. Of the species which can condense in these regions to form the bulk composition of the cloud particle Fe[s], Al_2O_3 [s], CaTiO_3 [s], Mg_2SiO_4 [s], CaSiO_3 [s] and SiO[s] are the most dominant. The nucleation is particularly inefficient for the daysides of the hottest models ($\log_{10}(J_{*,\text{tot}}) \leq -13 \dots -15 \text{ cm}^{-3} \text{ s}^{-1}$) resulting in larger average particle sizes ($\langle\langle a \rangle_A\rangle \sim 10^{3.7} \dots 10^5 \mu\text{m}$). Hence, clouds forming in the deeper atmosphere at the substellar point are comprised of large particles made of high temperature condensates and silicates. For models with $T_{\text{eff,P}} > 1800 \text{ K}$, no cloud particles exist at the substellar point for the G star orbiting planets as the atmospheres are too warm to permit any cloud formation.

The planetary atmosphere clouds differ most significantly at the equatorial evening terminator. For the cooler planets the material composition is similar to that of the other three points previously discussed, with silicates dominating and the high temperature condensates and metal oxides contributing equally to the remaining volume. With increasing planetary global temperature, $T_{\text{eff,P}} \geq 1800 \text{ K}$ there is significant drop in the fraction of metal oxide condensates in favour of high temperature condensates. For the G star orbiting planets, silicates remain the dominant contributing species, excepting the hottest $T_{\text{eff,P}} = 2600 \text{ K}$ model where high temperature condensates dominate. For the M star orbiting planets, however, the fraction of high temperature condensates increases and the fraction of silicates decreases with increasing model temperature. The average particle size in the atmospheric clouds is similar between both stellar types.

The salts (KCl[s], NaCl[s]) do not contribute significantly to the average cloud particle volume composition at any point for any of the stellar types and planetary temperatures.

We note that carbonaceous materials have not been considered in the cloud formation model applied here because the undepleted element abundance was considered solar, hence, oxygen rich. The effect of element depletion/enrichment by cloud formation will be addressed in Sect. 3.3. Carbon-rich materials in form of condensates (not hazes) have been discussed in the literature to study the effect of non-solar elemental abundances on the cloud structure and composition (Helling et al. 2017; Mahapatra et al. 2017; Helling 2019a; Herbort et al. 2022). The formation of hydrocarbon hazes (which are not condensates) may be a potential explanation for radii that maybe 1.5–2 \times larger in the UV than in the optical (Corrales et al. 2021). This, however, requires to free the necessary carbon which is chemically blocked by CO and/or CH_4 in an oxygen-rich gas. While photochemically triggered hydrocarbon hazes can form in the upper atmosphere, their optical depth

may not be large enough compared to mineral cloud particles (Helling et al. 2020).

Our systematic study has demonstrated that atmospheric thermodynamic structures lead to the formation of clouds that differ in particle sizes and numbers, and to a lesser extent, in their material composition. This finding is based on a cloud formation model in contrast to Parmentier et al. (2021) who use particle sizes as parameters for their study of individual cloud materials. The suggestion of nightside clouds being similar for different planets promoted in Gao & Powell (2021) cannot be supported by our simulations, nor ‘the simple explanation that hot Jupiters all have the same species of nightside clouds’ (Keating et al. 2019).

3.3. Changing C/O regimes with changing global system parameters

Cloud formation affects the local atmospheric chemistry in two ways. First, through the opacity feedback onto the temperature structure, and second, by element depletion of all elements that participate. Since cloud radiative feedback is not included in the GCMs that represent the input state for our cloud models, we focus here on the latter effect. Specifically, we only refer to the effect on the oxygen abundance (which affects the carbon-to-oxygen ratio) and the mean molecular weight, and the major effects will be summarised below. The detailed spatial results can be found in the accompanying catalog (Lewis et al. 2022). Extensive studies regarding other elements have been presented in previous papers of our group.

3.3.1. The carbon-to-oxygen ratio

The carbon-to-oxygen ration (C/O) can be used as a fingerprint for the two nucleation regimes of exoplanet atmospheres introduced in Sect. 3.2.1: the exoplanets that are covered in clouds homogeneously globally (e.g., HATS-6b) and those with a partial cloud coverage some of which feature strong day-night asymmetries (e.g., WASP-18b). These characteristic are:

- the undepleted (e.g., solar) C/O on cloud-free hot daysides,
- increased C/O ratio close to 0.75–0.8 where clouds form in the cool upper nightside atmosphere,
- decreased C/O with increased pressure as cloud particles evaporate and replenish the gas phase with oxygen that was trapped in silicates and metal oxides.

The C/O threshold of 0.8 matches result of Helling et al. (2021a) and provides confirmation of findings by Baxter et al. (2020) for hot and ultra-hot Jupiters to have $\text{C/O} < 0.8$.

The changes in C/O are a direct consequence of depletion of the oxygen by the nucleation and the surface growth. The carbon abundance is not affected as all planetary atmosphere considered here are assumed to be oxygen rich, hence, all carbon will be locked in CO (or CH_4). Mixing processes can only affect C/O (any local element abundance) if the respective processes are faster than the chemical processes involved in cloud formation.

3.3.2. Mean molecular weight

A constant mean molecular value, μ , is typically assumed when running 3D GCMs to reduce the computational demands of the simulations (Drummond et al. 2018). A constant mean molecular weight of 2.3 is likewise adopted in the GCMs underlying this study, in agreement with an atmospheric composition dominated by H_2 and He. However previous work has shown that this

assumption may not be valid for all planets and generally for the whole atmosphere. We show in [Helling et al. \(2021a\)](#) that in the case of ultra-hot Jupiters (e.g. HAT-P-7b, WASP-121b), where the day and nightside temperatures can differ by greater than 1500 K, there are substantial differences in the ionisation state of the atmospheric gas phase. The dayside is dominated by atomic and ionised species compared to a nightside dominated by molecular species.

Different classes of exoplanet atmosphere can therefore be expected to be characterised by different mean molecular weight regimes. In this paper, these classes are determined by the irradiation the planet receives and which affects the local thermal ionisation.

For the grid models with $T_{\text{eff,P}} \leq 1600$ K the entire planet maintains a constant value of $\mu = 2.35$ which is consistent with a molecular hydrogen dominated atmosphere. The nightside of all model planets has a constant $\mu = 2.35$. The hotter models ($T_{\text{eff,P}} \geq 1800$ K) show a decrease in μ only on the dayside initially, at the hottest region, offset from the substellar point. With increasing model temperature μ is decreased across more of the upper atmosphere on the dayside. The lowest value of mean molecular weight achieved is $\mu = 1.8$ and is centred around the substellar point in the upper atmosphere of the hottest $T_{\text{eff,P}} = 2400, 2600$ K models which orbit the M and K stars. The maximum value of the decrease is $\mu = 1.8$ and is centred around the substellar point in the upper atmosphere of the hottest $T_{\text{eff,P}} = 2400, 2600$ K models which orbit the M and K stars. For the G and F stars, $\mu \geq 1.95$ across the dayside.

We conclude that it is reasonable to assume a constant mean molecular weight consistent with a H_2 -dominated atmosphere for planets with $T_{\text{eff,P}} \leq 1600$ K, such as warm Saturn or some hot Jupiter class planets, but not for hotter planets. The implication of the changing mean molecular weight due to the dissociation of H_2 is demonstrated in [Roth et al. \(2021\)](#).

3.4. Thermally driven ionospheres and the emergence of exoplanetary global electric circuits

The degree of thermal ionisation ($f_e = p_e / (p_{\text{gas}} + p_e)$, where p_e is the electron pressure) may be used to indicate plasma-like behaviour of the atmosphere, and by extension the potential for a thermally driven ionosphere to exist. [Rodríguez-Barrera et al. \(2015\)](#) propose that values of $f_e \geq 10^{-7}$ mark the transition between gas to plasma behaviour which is relevant for discussing the magnetic coupling of exoplanet atmospheres (e.g., [Beltz et al. 2022](#)). Here we are also interested in comparing the extension and location of the ionised part of the atmosphere to the location of the clouds. A net electron flux may be established that causes the cloud particles to gain a net electrical charge in an ionised atmosphere, and more generally, a global electric circuit will establish if sufficient global background ionisation is available ([Helling 2019b](#)).

Figures 9 and 10 present the thermal degree of ionisation in comparison to the global distribution of the exoplanet clouds. We utilize the mean particle sizes in 2D equatorial slices for our comparison to regions of high ionisation based on thermal ionisation. The $f_e \geq 10^{-7}$ threshold is shown as solid contour line and the location of $f_e \geq 10^{-6}$ (dashed contour line) indicates the region where the thermal ionisation increases. The degree of ionisation resulting from thermal processes can be of the same magnitude as the degree of ionisation resulting from other processes such as cosmic rays and UV radiation if the temperature is high enough ([Barth et al. 2020](#)). The Lyman-continuum irradiation in star forming regions may be considerably higher than

thermal effects in the very rarefied gases of the outer atmosphere of planets ([Rodríguez-Barrera et al. 2018](#)).

The degree of thermal ionisation never exceeds $f_e = 10^{-7}$ in the upper atmosphere for any of the model planets where $T_{\text{eff,P}} \leq 1600$ K. For $T_{\text{eff,P}} = 1800$ K, a dayside ionosphere emerges for all models, though it is more extended for the slower rotators. For the F, G and K star models, there is some overlap between the dayside cloud layers and the edge of the ionosphere, with the K star models having the most overlap. The most overlap for all stellar types occurs at $T_{\text{eff,P}} = 2400$ K; beyond this planetary effective temperature the overlap decreases due to the reduction in the size of the dayside cloud layers.

While the day-night asymmetry in f_e begins to appear at $T_{\text{eff,P}} = 1000$ K, the thermal degree of ionisation does not reach 10^{-7} in the outer atmosphere until $T_{\text{eff,P}} = 1400$ K, but only for the M and the F stars. Larger cloud particles ($\langle a \rangle_A \geq 10^{2.2} \mu\text{m}$) form at pressures below this level of ionisation ($\leq 10^{-2}$ bar). Such cool exoplanets are therefore unlikely to have a thermally driven ionospheres. At $T_{\text{eff,P}} = 1600$ K and $T_{\text{eff,P}} = 1800$ K, the ionisation level exceeds 10^{-7} above 10^{-1} bar across the dayside for the M and the K star exoplanets. However, there is no cloud formation in these regions in the M and the K star exoplanet atmospheres. The G and the F star exoplanets with $T_{\text{eff,P}} = 1600$ K form medium sized cloud particles in their atmospheres ($\langle a \rangle_A \geq 10^{0.8} \mu\text{m}$) in regions (near the evening terminator) where $f_e \geq 10^{0.7}$. A electron flux induced cloud particle charging may occur in these atmospheres. Above $T_{\text{eff,P}} = 1800$ K, what little clouds remain form in regions where $f_e < 10^{-7}$.

It is not clear yet what effect the dayside ionization has on the wind flow and thus the 3D thermodynamics of ultra-hot Jupiters. [Tan & Komacek \(2019\)](#) propose that reduced molecular mean weight at the dayside, which we neglect in the 3D GCM here, leads to larger wind speeds. Further, the thermal effect of hydrogen dissociation at the dayside and re-combination at the nightside reduces the horizontal temperature gradient. The first was proposed to lead to dayside cooling and the latter to nightside warming. However, [Tan & Komacek \(2019\)](#) did not consider cloud formation and their results seem to contradict [Baxter et al. \(2020\)](#). The latter study find a particularly large dayside emission, which the authors attribute to low dayside albedo and inefficient heat circulation, as we also re-produce in this study.

[Beltz et al. \(2022\)](#) suggest that coupling between the ionized wind and magnetic fields of 3 G can disrupt wind jets at the dayside completely, in particular for the upper atmosphere ($p < 0.01$ bar), leading instead to equatorial-to-polar flow, greatly diminishing heat circulation between nightside and dayside. It is not clear yet how such a flow regime may affect vertical transport and cloud formation at the nightside.

In any case, it is quite clear that the daysides of ultra-hot Jupiters are fundamentally different from those of colder planets and that further work is needed here to study wind flow and cloud formation in the context of dayside ionization and magnetic field coupling. Further implications of atmospheric ionisation are discussed in Sect. 4.2.

We conclude that all gaseous exoplanets can be expected to have a thermally ionised inner atmosphere for pressure ≥ 10 bar where, therefore, magnetic coupling of the atmosphere can occur. Exoplanet atmospheres with $T_{\text{eff,P}} > 2000$ K can be expected to have deep thermally driven ionospheres on their dayside. This ionosphere reached into the terminator regions the hotter the planetary atmosphere is. We therefore conclude that these exoplanets have (a) a geometrically more extended, cloud-free dayside compared to their nightside

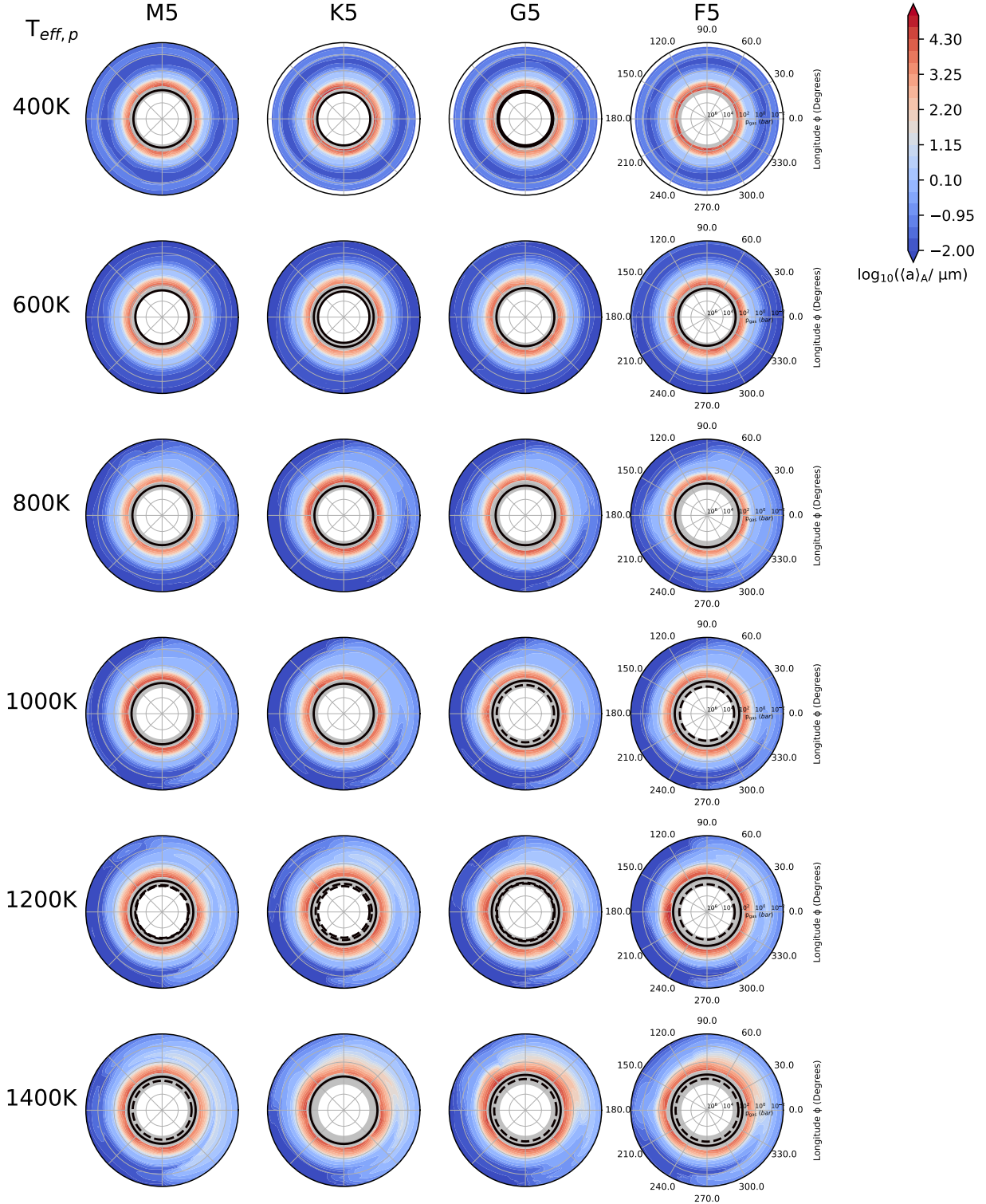


Fig. 9. Surface averaged mean particles size, $\log_{10}(\langle a \rangle_A / \mu\text{m})$, in 2D equatorial slices ($\theta = 0^\circ$) superimposed with degree of ionisation threshold of $f_e = 10^{-7}$ (solid; $f_e = 10^{-6}$ is dashed line) for the $\log_{10}g = 3$ [cgs] 3D GCM models for $T_{\text{eff},p} = 400 \dots 1400$ K for all stellar types. The outer limit for the pressure is fixed at $10^{-3.5}$ bar for all models.

which (b) can undergo magnetic coupling to a global planetary magnetic field should it exist, and (c) that a global electric circuit may determine the charge distribution within the atmosphere longitudinally, i.e. east-west-ward. Both, the global and local extension of the ionosphere and the global electric circuit will increase if additional ionisation processes

occur. We further conclude that both regimes of exoplanet atmospheres, those with a globally homogeneous cloud coverage and those with an intermittent or asymmetric cloud coverage will undergo different degrees of magnetic coupling inside their atmospheres and, hence, may exhibit different magnetic field geometries.

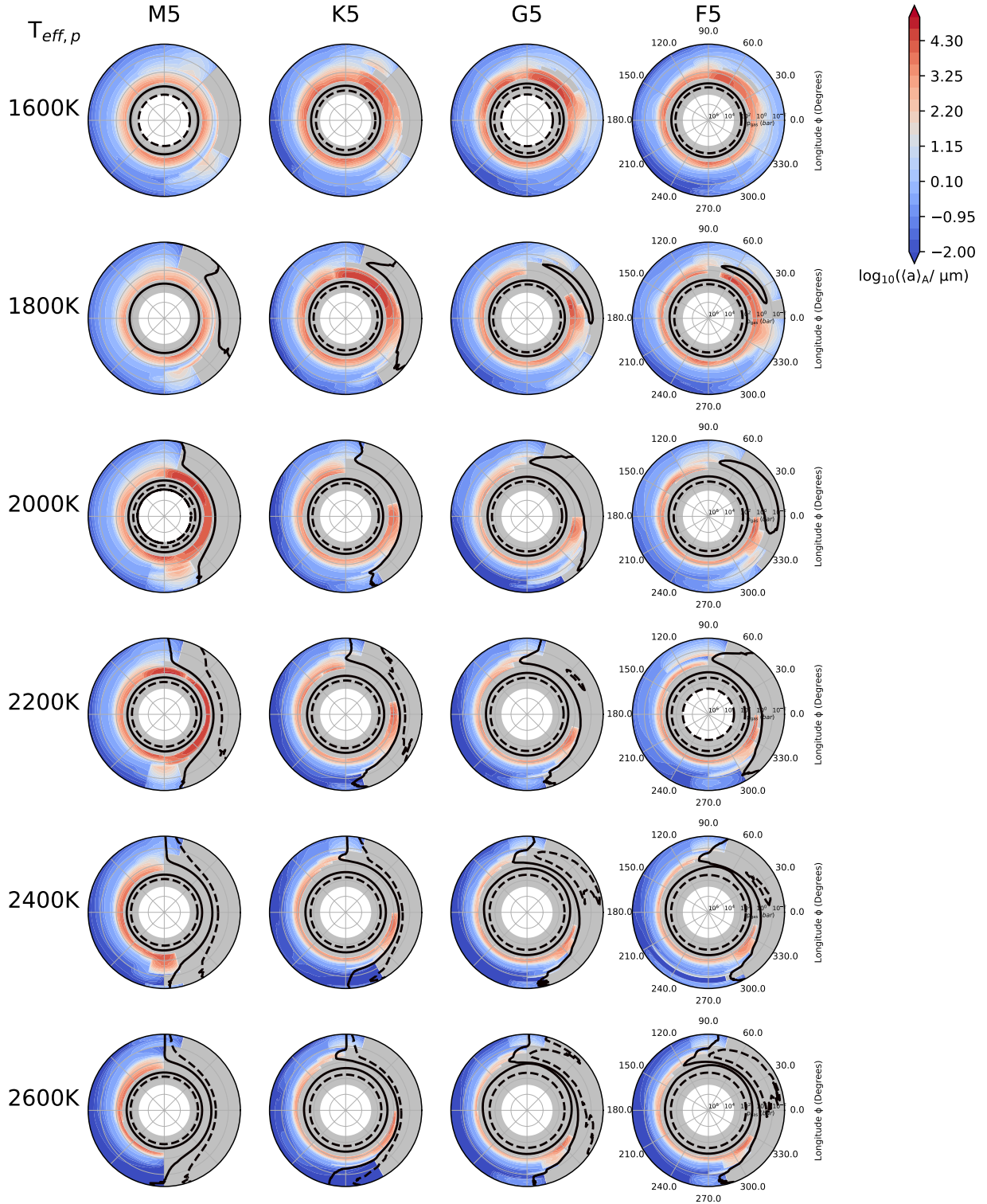


Fig. 10. Surface averaged mean particles size, $\log_{10}((a)_A/\mu\text{m})$, in 2D equatorial slices ($\theta = 0^\circ$) superimposed with degree of ionisation threshold of $f_e = 10^{-7}$ (solid; $f_e = 10^{-6}$ is dashed line) for the $\log_{10}g = 3$ [cgs] 3D GCM models for. $T_{\text{eff,P}} = 1600 \dots 2600$ K for all stellar types. The outer limit for the pressure is fixed at $10^{-3.5}$ bar for all models.

4. Exoplanet weather/climate regimes: the cool, the transient and the hot exoplanet atmospheres

The previous sections have presented a global picture of cloud formation in gaseous extrasolar planets that orbit M, K, G and F host stars at different distances. Most of the details for individual models, such as the individual nucleation rates or material

compositions of the cloud particles, have been left to a supplementary catalogue. Now we provide a comparison of three groups of exoplanets of the same planetary effective temperature that orbit different host stars at different distances.

A closer inspection of the 3D GCM model grid shows that the planetary model atmospheres fall into three cloud formation regimes, which we call classes, separated by planetary

temperature: class i) the cool planets ($T_{\text{eff,P}} \leq 1200$ K), class ii) the transition planets ($T_{\text{eff,P}} = 1400\text{--}1800$ K), and class iii) the hot planets ($T_{\text{eff,P}} \geq 2000$ K). The temperature thresholds should be considered as approximate and may shift by ± 200 K due to modelling uncertainties and additional parameter dependencies (e.g., $\log(g)$). These cloud forming regimes are representative of weather regimes on short timescales but also of climate regimes if understood for longer time scales. Example objects for class (i) include HATS-6b and NGTS-1b, for class (ii) WASP 43b, NGTS-10b and HD 209458b, and for class (iii) WASP-18b, WASP-121b, WASP-103b and also brown dwarfs in close orbits around white dwarfs similar to WD 0137b and EPIC 2122B. We note here that, young objects excepted, brown dwarfs may have a stronger internal heating than giant gas planets at a similar age. The overall trend, however, can be expected to be very similar with respect to the large day-night difference in cloud presence, the far stronger ionisation on the day side, as well as the lower mean molecular weight in the night side. This hypothesis is supported by the finding that Baeyens et al. (2022) shows that the mentioned BD-WD pairs are in general agreement in circulation regimes with Lee et al. (2020); Tan & Showman (2021).

To provide an overview of each of these three regimes we select a specific temperature planet model which is representative of the whole regime, these are $T_{\text{eff,P}} = 800, 1600, 2400$ K. The transition and hot planet temperatures line up with the approximate temperature space occupied by the hot and ultra-hot Jupiter class planets (Table 1 in Helling et al. 2021a). The cool planets represent the homogeneous regime from previous sections, while the transient and the hot planets represent the regime of intermittent cloud formation. In the following, we will confirm that the intermittent regime is the best suitable to look for morning/evening terminator differences (Baeyens et al. 2022) which is greatly amplified by the cloud distribution.

4.1. Asymmetric cloud coverage

The complex interplay between dynamics and irradiation is reflected by the asymmetric cloud coverage. Further, for a given global (equilibrium or effective) temperature, planets around K dwarfs are substantially faster rotators than G dwarf planets. Thus, K dwarf planets tend to have more asymmetric and smaller dayside cloud coverage compared to G dwarf planets of the same global temperature. This is particularly apparent for $T_{\text{eff,P}} = 1200 \dots 1600$ K (classes i) and ii)), of which several will be observed by JWST to investigate differences in evening/morning clouds (WASP-63b and HD 189733b). We note that the cloud layers will be able to extend into deeper atmospheric layers for planets with higher masses where the increasing pressure increases the thermal stability of the cloud particles despite the increasing local temperature. This effect can be manipulated for low-mass planets by the choice of the inner boundary for the computational domain in 3D GCMs (see Sect. 6 in Helling et al. 2021a).

Nightside cloud coverage. In all three classes (i, ii, iii), clouds do form on the nightside. This is an essential result because the greenhouse feedback of the nightside clouds will reduce the heat redistribution in the atmosphere. This affects the atmospheric temperature structure of the whole planet and the observed phase curves (Parmentier et al. 2021). We conclude that the nightside clouds play a particularly large role for exoplanets in the intermediate temperature regime (class ii). In case of an increasing nightside

temperature due to radiative transfer effects, for example Schneider et al. (2022), the location of thermally stable materials will change somewhat. Other effects need a more detailed consideration: a decrease of local density may not affect the cloud's optical depth due to an increased geometrical extension of the cloud, for example.

Dayside cloud coverage. The dayside cloud coverage distinguishes the cool, the transition and the hot planets in their global weather and climate appearance. A nearly homogeneous cloud coverage emerges for the coolest planets (case i), a partial or transient cloud coverage for class (ii) and a cloud-free dayside with considerable ionisation for the hot planets of class (iii). The details of these cloud layers have been discussed in Sects. 3.2.1–3.2.3. Associated with these changing cloud coverage are effects on the local chemistry which we presented in terms of the local C/O and the mean molecular weight (Sect. 3.3). The dayside of the cool planetary regime will, hence, show a strongly depleted set of element abundances and a C/O that differs from the undepleted, pristine value. Planets in the transient regime will show such depleted elements in regions where cloud formation occurs which will be near the morning terminator. Hence, the dayside of these planets will be determined by a mix of depleted and undepleted areas. The dayside of planets in the hot regime show a mainly undepleted set of element abundances and therefore a solar (or pristine) C/O in combination with a decreased mean molecular weight due to the thermal instability of H_2 in such hot atmospheres. Large day-nightside temperature differences further result into a different geometrical extension of the dayside as well as the terminator regions. Hence, the cold planets in our grid (class i) are likely to have no large geometrical asymmetries between the day- and the nightside, while the hot class (iii) planets may have a substantial geometrical asymmetry already within the atmosphere below $p_{\text{gas}} < 10^{-8}$ bar as footpoint of a planetary mass loss.

The dayside cloud coverage for planets of similar global temperature may well be different for different host stars. This is the case for the class (ii) planets, WASP-43b/NGTS-10b (Fig. 12) that orbit an K dwarf and HD 209458b (Fig. 13) that orbits a G star. WASP-43b and NGTS-10b have a 10 times greater surface gravity compared to HD 209458b which, in addition, leads to cloud extending deeper into the atmosphere.

We note that recent WFC3/UVIS-HST observations in scattered light between 346–822 nm of WASP-43b are interpreted as seeing a (very dark) cloud-free dayside for pressure >1 bar (Fraie et al. 2021). This may be supported by the fast rotation models presented here. Conversely, observations of HD 209458b that canonically concluded it to be very cloudy would only pick up the very cloudy half of the dayside and not the cloud-free region that occur towards the evening terminator as suggested in Fig. 13. Extensive modelling studies are conducted for HD 209458b (e.g., Lines et al. 2018b; Schneider et al. 2022) which may enable a detailed modelling comparison.

Class (ii) enables further to study the effects of rotation on the cloud patterns that characterise the weather and climate of these gaseous exoplanets. For example, planets with $T_{\text{eff,P}} = 1600$ K that orbit a cooler star (M dwarf; Fig. 11) need to orbit their host star at a smaller orbital separation of 0.13 days compared to a planet of the same effective temperature orbiting a G star orbiting with 1.55 days (Fig. 13). Our simulations therefore support our hypothesis that WASP-43b and NGTS-10b around K dwarf may indeed show rotational deviations compared to G dwarf planets similar to HD 209458b of the same temperature but with much slower rotation.

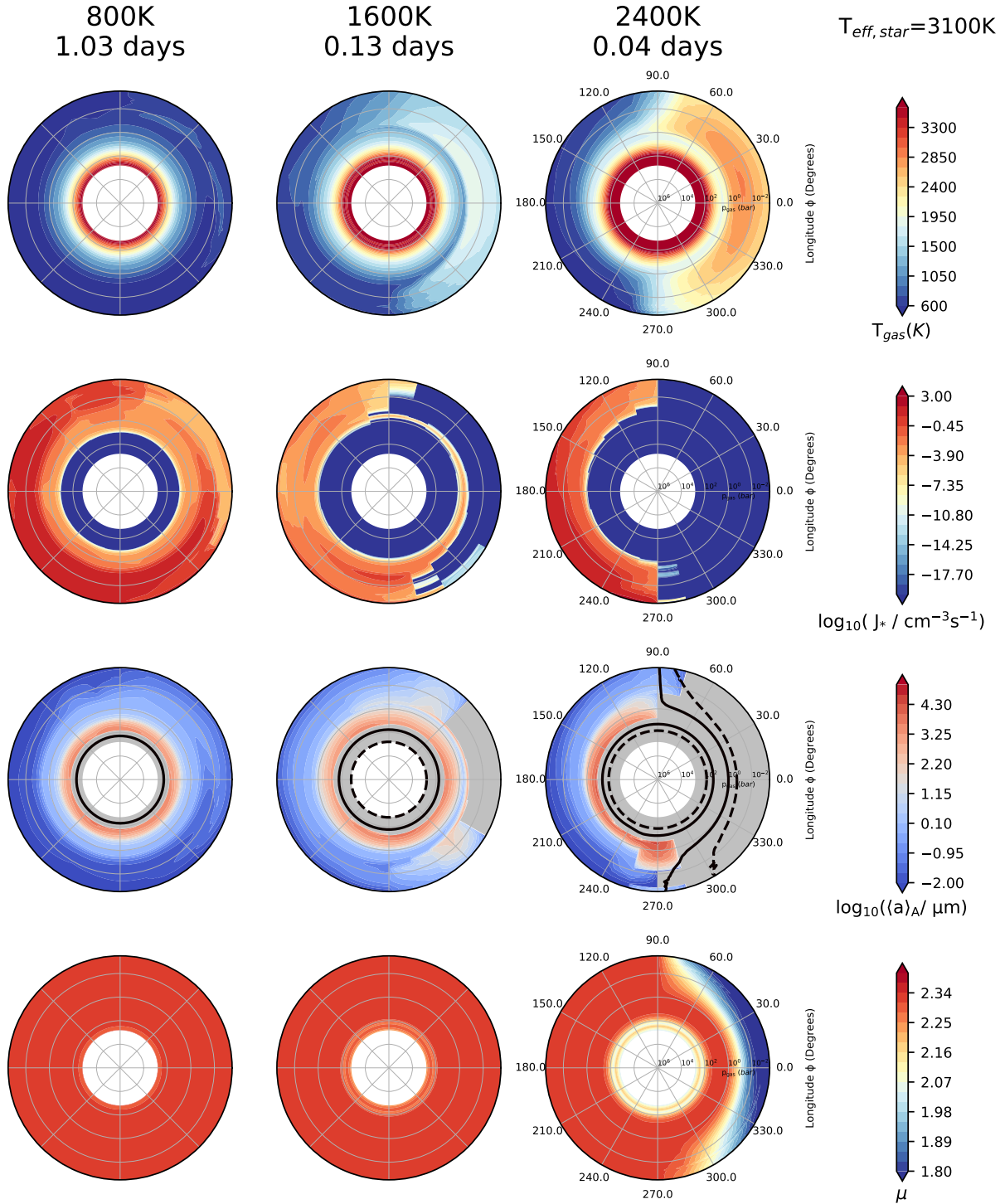


Fig. 11. Cool ($T_{\text{eff,P}} = 800$ K; e.g. HATS-6b, NGTS-1b), the transient ($T_{\text{eff,P}} = 1600$ K; e.g. WASP-43b, NGTS-10b), the hot ($T_{\text{eff,P}} = 2400$ K; brown dwarfs WD 0137 and EPIC 2122) exoplanet atmospheres ($\log_{10} g = 3$ [cgs]) with an M dwarf host star. 2D equatorial plane slices ($\theta = 0^\circ$) for the 1D profiles extracted from the 3D GCM models (Baeyens et al. 2022) show the main cloud formation properties: local gas temperature [K] (first row), total nucleation rate $\log_{10}(J_*/\text{cm}^{-3}\text{s}^{-1})$ (second row), surface averaged mean particle size $\log_{10}(\langle a \rangle_A/\mu\text{m})$ overlaid with $f_c = 10^{-7}$ (solid line; $f_c = 10^{-6}$ (dashed); third row), mean molecular weight (fourth row). The outer limit for the pressure is fixed at $10^{-3.5}$ bar for all models.

We note that the transition class (ii) of cloud climates arises because of a tight interplay between the thermal stability and the thermal background, which depends itself on the heat redistribution and wind field. Direct horizontal advection of cloud species is not included in our models, and could thus smear out the boundaries of the partial cloud coverage. This smearing will be limited by the thermal stability of the cloud particle in particular towards high-temperature regions similar to the dayside. GCMs

with 3D cloud-coupling (e.g. Lines et al. 2018a) may be used to refine the boundaries of the classes defined in this work.

4.2. The asymmetry of the thermal ionosphere

How does the deep ionosphere affect vertical transport of elements observed with high resolution observations? Can we readily compare observed abundances in the upper atmosphere

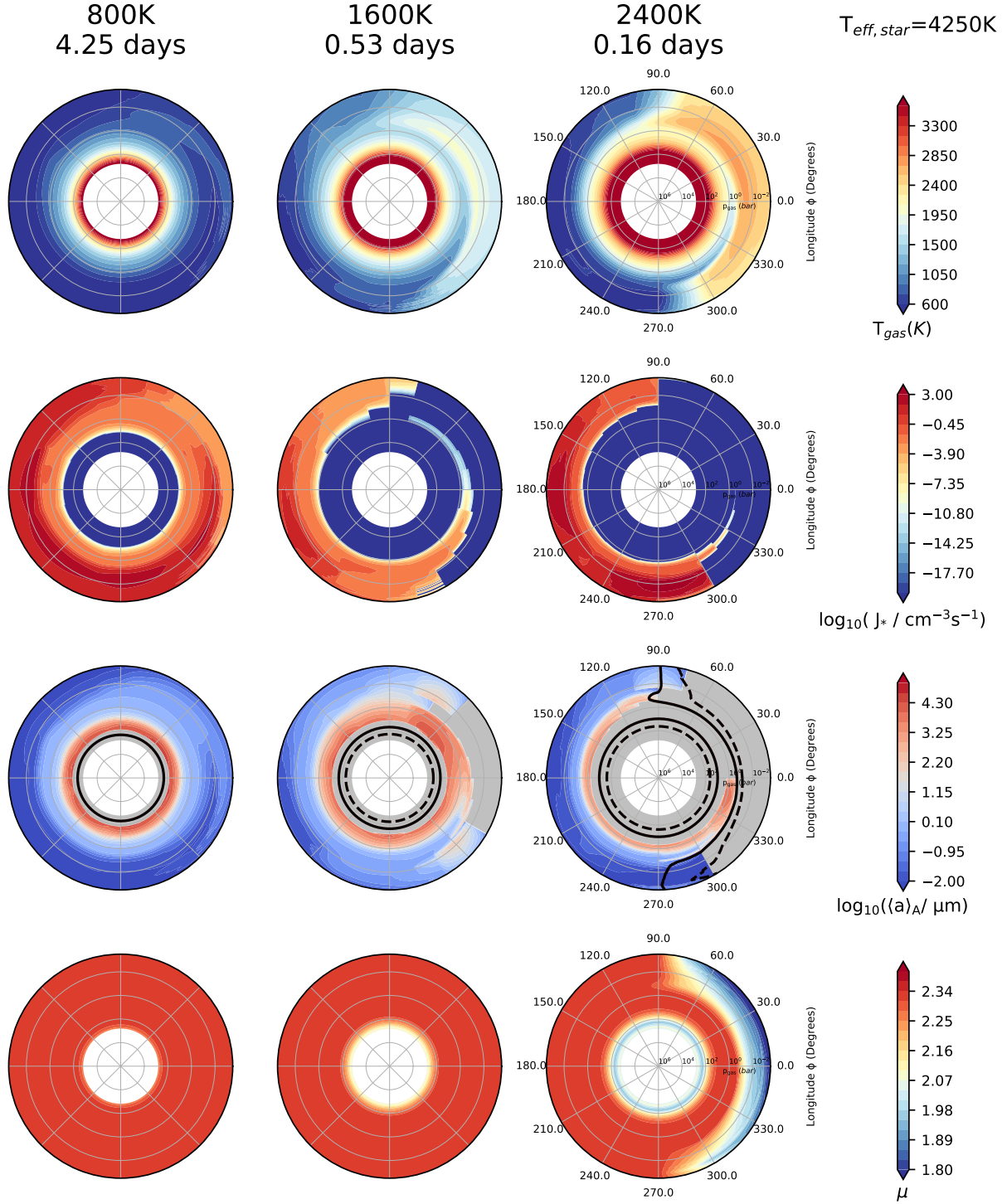


Fig. 12. Cool ($T_{\text{eff,P}} = 800\text{ K}$), the transient ($T_{\text{eff,P}} = 1600\text{ K}$), the hot ($T_{\text{eff,P}} = 2400\text{ K}$) exoplanet atmospheres ($\log_{10}g = 3$ [cgs]) with an K dwarf host star. 2D equatorial plane slices ($\theta = 0^\circ$) for the 1D profiles extracted from the 3D GCM models (Baeyens et al. 2022) show the main cloud formation properties: local gas temperature [K] (first row), total nucleation rate $\log_{10}(J_*/\text{cm}^{-3}\text{s}^{-1})$ (second row), surface averaged mean particle size $\log_{10}((a)_A/\mu\text{m})$ overlaid with $f_e = 10^{-7}$ (solid line; $f_e = 10^{-6}$ (dashed); third row), mean molecular weight (fourth row). The outer limit for the pressure is fixed at $10^{-3.5}$ bar for all models.

of (partly) ionized planets with those of un-ionized planets? While these questions are outwith the scope of this paper, we shortly review them with respect to the introduced cloud formation regimes that are characteristic for potentially distinct weather and climate scenarios. Weather and climate scenarios are determined by the thermo- and hydrodynamics behaviour of the atmosphere which does determine the global and local gas

phase and cloud characteristics, but also secondary processes such as ionisation and the emergence of global electric circuits (GEC) (Helling et al. 2016). The conditions for the emergence of an exoplanet GEC (eGEC) include a sufficient ionisation of the atmosphere and the presence of clouds that may produce lightning (Helling 2019b). Little to no eGEC effects are expected on the atmosphere structure for the solar system planets

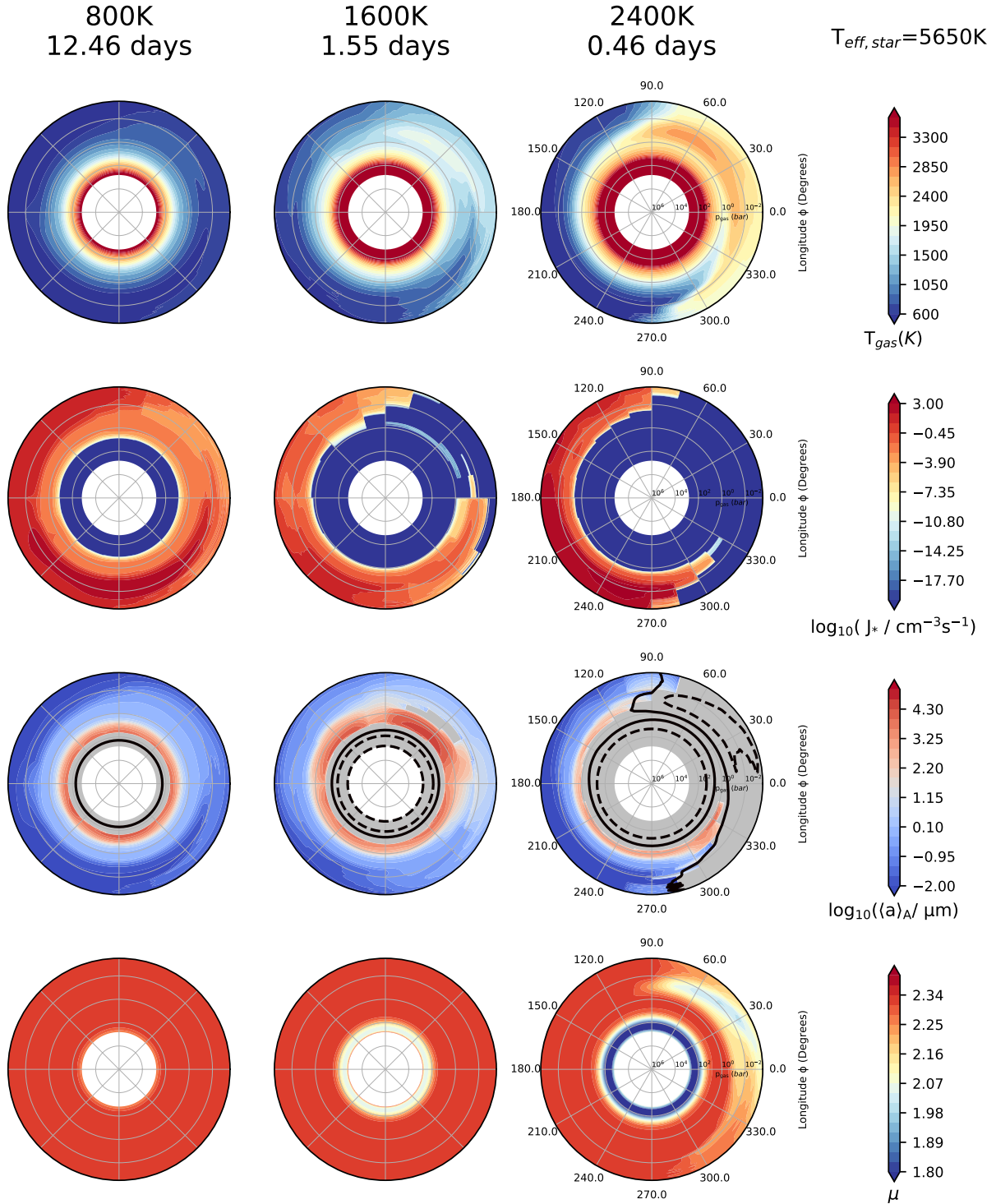


Fig. 13. Cool ($T_{\text{eff,P}} = 800$ K), the transient ($T_{\text{eff,P}} = 1600$ K; e.g., HD 209458b), the hot ($T_{\text{eff,P}} = 2400$ K) exoplanet atmospheres ($\log_{10}g = 3$ [cgs]) with a G-type host star. 2D equatorial plane slices ($\theta = 0^\circ$) for the 1D profiles extracted from the 3D GCM models (Baeyens et al. 2022) show the main cloud formation properties: local gas temperature [K] (first row), total nucleation rate $\log_{10}(J_* / \text{cm}^{-3} \text{s}^{-1})$ (second row), surface averaged mean particle size $\log_{10}(\langle a \rangle_A / \mu\text{m})$ overlaid with $f_c = 10^{-7}$ (solid line; $f_c = 10^{-6}$ (dashed); third row), mean molecular weight (fourth row). The outer limit for the pressure is fixed at $10^{-3.5}$ bar for all models.

(Aplin et al. 2020), a conclusion that most likely can be extrapolated to extrasolar planets. The ionisation processes that drive the eGEC, however, do affect the local chemistry and may support the formation of cloud condensation nuclei in particular in the photo-dominated uppermost atmosphere layers in analogy to processes on Earth (Svensmark et al. 2017; Tomicic et al. 2018).

We therefore seek to build our understanding of where in the atmosphere which ionisation processes act and how this may help to understand the global weather and climate on exoplanets. Based on the modelling framework of this paper, we concentrate on the thermal ionisation in what follows. Figure 1 contextualises the model grid that we explore here with respect to a selection of

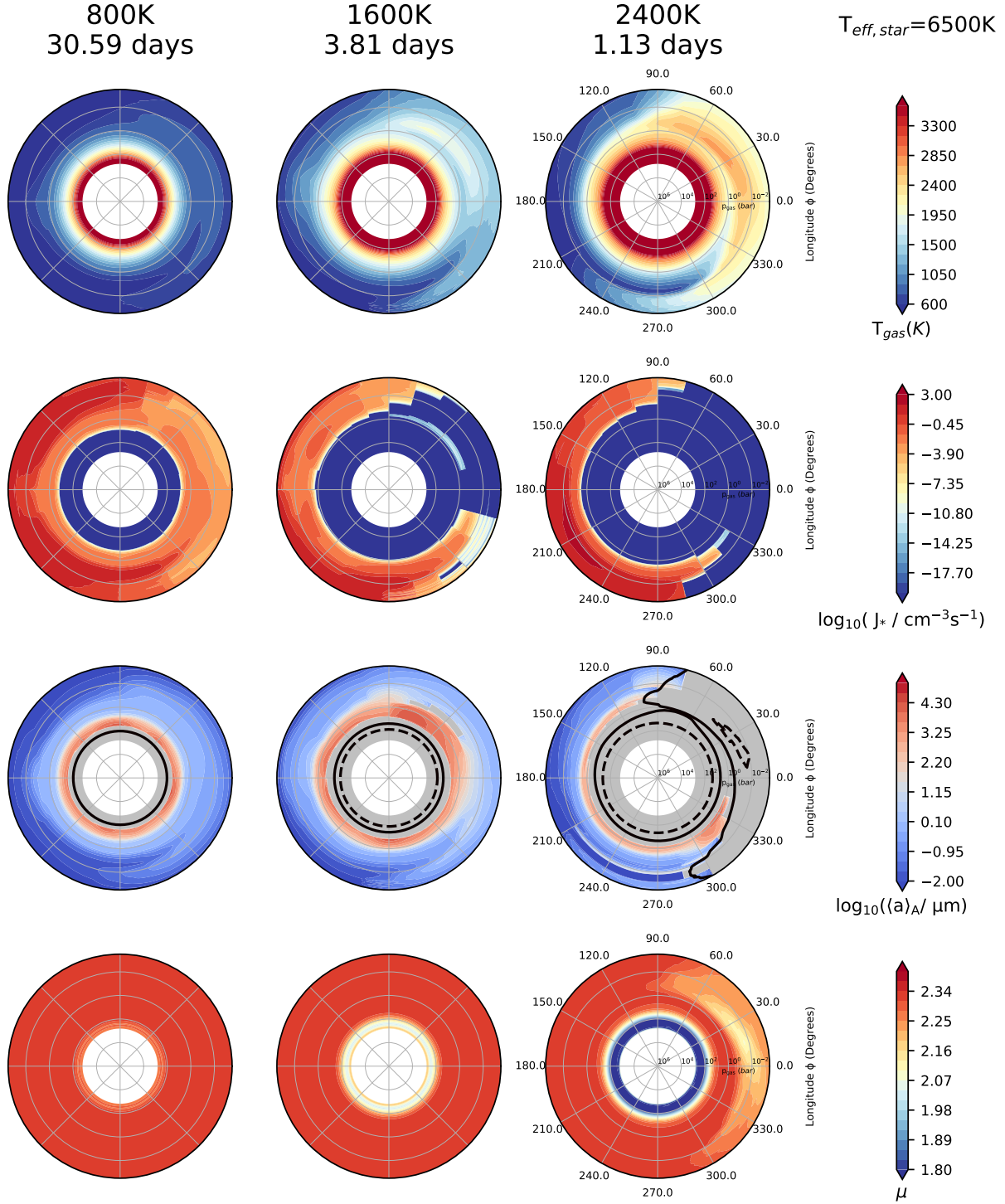


Fig. 14. Cool ($T_{\text{eff,P}} = 800$ K), the transient ($T_{\text{eff,P}} = 1600$ K), the hot ($T_{\text{eff,P}} = 2400$ K) exoplanet atmospheres ($\log_{10} g = 3$ [cgs]) with an F type host star. 2D equatorial plane slices ($\theta = 0^\circ$) for the 1D profiles extracted from the 3D GCM models (Baeyens et al. 2022) show the main cloud formation properties: local gas temperature [K] (first row), total nucleation rate $\log_{10}(J_* / \text{cm}^{-3} \text{s}^{-1})$ (second row), surface averaged mean particle size $\log_{10}((a)_A / \mu\text{m})$ overlaid with $f_e = 10^{-7}$ (solid line; $f_e = 10^{-6}$ (dashed); third row), mean molecular weight (fourth row). The outer limit for the pressure is fixed at $10^{-3.5}$ bar for all models.

possible candidates (dark golden dust with error bars; candidate data from Tables C.1, C.2) for future UV missions, for example ARAGO (Neiner et al. 2019), PolStar (Scowen et al. 2022) or POLLUX on LUVOIR (Bouret et al. 2018).

It was suggested by Tan & Komacek (2019), Helling et al. (2021b) and Beltz et al. (2022) that the degree of ionization at the dayside of ultra-hot Jupiter would promote very

efficient coupling between the ionized wind flow and the planetary magnetic field if it is of the order of a few Gauss. For example, Rodríguez-Barrera et al. (2018) demonstrate that the magnetic flux threshold value for where the cyclotron frequency exceeds the local gas collisional frequencies decreases to well below 1G in the upper, low-density atmospheric layers. For the high-density atmosphere at >1 bar, a local magnetic flux of

> 100 G may be required. Consequently, the efficient magnetic field coupling of the atmospheric gas could lead to a very sharp transition from efficient day-to-nightside heat transport and very inefficient day-to-nightside heat transport as soon as a sufficient dayside ionization occurs. Thus, the transition between the intermediate and ultra-hot temperature regime would be affected by its degree of ionization. We find, however, that while the ionization can penetrate deep into the planet's atmosphere, the degree of ionization may not be sufficient to allow for efficient coupling between ionized gas and magnetic fields. In that case, the transition between intermediate and ultra-hot regime could occur for different temperature depending on rotational period, where faster rotators would exhibit a transition at cooler global temperature than slower rotators. That is, planets orbiting an K dwarf would transit at lower global temperatures than planet around F dwarf stars.

Observationally, phase curves of exoplanets around the 1800–2000 K temperature transition between case (ii) and (iii) with different orbital periods could be compared to determine if they exhibit differences in heat circulation and cloud distribution. Transiting planets orbiting bright stars with global temperatures around the case (ii) and (iii) transition between intermediate and ultra-hot Jupiters are e.g. K2-31b ($P = 1.26$ days, G type, Grziwa et al. 2016⁴), WASP-14b ($P = 2.2$ days, F type, Raetz et al. 2015; Southworth 2012; Wong et al. 2015 and for $T_p = 2000$ K WASP-19b ($P = 0.78$ days, G type, see e.g. Hebb et al. 2010; Maxted et al. 2013). Reduced hot spot shift with rotation period for both intermediate and hot Jupiters have been verified very recently by a systematic study of *Spitzer* data (May et al. 2022).

4.3. Concluding discussion

The grid study presented here supports and complements the ensemble of observational study of gas planets across different temperatures and rotation periods in preparation of the PLATO and the Ariel space missions. Such complex models are needed to move on from single-case models for specific planets which does require a considerable adjustment in various physical and numerical parameters to fit the observational data (e.g., inner and outer boundary of computational domain, viscose damping, ...).

Roman et al. (2021) have also performed a grid study with a 3D GCM and clouds. These authors, however, started with 1400 K, thus missing HD 189733b (with 1200 K). Both, Roman et al. (2021) and Parmentier et al. (2021) utilise simplified cloud models in contrast to our kinetic, multi-process approach, and they focus on only one rotational period. These authors conclude, that when radiative feedback of clouds is included, the dayside-to-nightside temperature differences increase and the eastward hot spot offset decreases.

For $T_{\text{gas}}=2000 - 3500$ K, both authors see an apparent westward shift for phase curves in the optical wavelength range (<1 micron). This apparent westward shift in the optical phase curves is associated with a pile-up of clouds on the morning terminator and due to enhanced reflection of stellar light over these regions. This "westward shift" is thus mainly a radiative effect and only visible in optical wavelength ranges. Roman et al. (2021) excluded planetary rotation as a modifying factor in cloud feedback for phase curves on the basis that irradiation on the planet is not modified by planetary rotation. Parmentier et al. (2021) did not investigate the impact of planetary rotation.

⁴ Its grazing transit will make this planet, however, difficult to characterize.

However, May et al. (2022) have shown that planetary rotation period definitely plays a role in moderating eastward shift and even allows the on-set of westward shift as observed in the IR *Spitzer* data. Thermal westward phase curve shifts, in contrast to optical westward phase shifts, can only be brought about by dynamical effects, that is, changes in the wind jet from eastward to westward flow. Carone et al. (2020) predicted that westward flow tendency on an intermediate Jupiter could appear for $P_{\text{orb}} < 1.5$ days in agreement with the observations reported by Charnay et al. (2022). For hotter planets, the westward shift already appears for $P_{\text{orb}} < 2$ days according to May et al. (2022). Thus, radiative effects alone are not sufficient when discussing cloud feedback and their effects on planetary phase curves. In this study, westward flow at the dayside is also included in the GCMs used here for intermediate to hot planets around M and K dwarf stars (see Baeyens et al. 2022, Fig. 2) but here we have not yet included the full radiative feedback.

Similar to Roman et al. (2021) and Parmentier et al. (2021), our result suggest a morning cloud pile-up for ultra-hot Jupiters for G, F and K planets, but not for M dwarf planets. Thus, while the cloud pile-up effect found is not sufficient to explain all aspects of phase curves for intermediate to Jupiters, it is probably amplifying the underlying westward flow tendency due to dynamical effect on the optical phase curves.

The closest analogues to ultra-hot Jupiters around M dwarfs in our simulations will also be important to consider to understand cloudy exoplanet phase curves. While ultra-hot Jupiters around M dwarfs do not exist, ultra-hot brown dwarfs in close orbit around a white dwarf star were detected: WD 0137B (2400 K, $P = 0.0803$ days, Lee et al. 2020) and EPIC 2122B (4000 K, $P = 0.047$ days). Observations by Zhou et al. (2022) indicate no asymmetries across the limbs. In addition, the 3D GCM of Lee et al. (2020) is very close to our ultra-hot Jupiters around M dwarf simulations in its strong day-night temperature dichotomy.

Interestingly, for WD 0137B water absorption was observed on the nightside. This may indicate that the nightside clouds lie deeper in the atmosphere in these two highly irradiated brown dwarfs due to the higher surface gravity of brown dwarfs compared to Jupiter mass planets as demonstrated, for example by the 1D DRIFT-PHOENIX models that solve cloud formation consistently as part of the whole atmosphere simulation (Fig. 2 in Witte et al. 2009). Recent results show that cloud particles and either magnetic drag or modified dynamics are needed to explain the phase curves of these objects (Lee et al. 2022a). Large modelling studies similar to this work and those of Roman et al. (2021); Parmentier et al. (2021) that cover similar global parameters but consider different physical effects are thus highly timely and vital to interpret detailed observational studies with JWST and Ariel. Fully consistent radiation transfer solutions are required and progress is being made (e.g., Schneider et al. 2022; Lee et al. 2022b). Only then can we identify which factors shape the phase curves of intermediate to hot Jupiters: radiative, dynamical, and magnetic effects and how clouds modify these.

5. Clouds beyond: The formation of mineral hazes

The gas pressure domain over which a 3D GCMs are simulated may differ for different authors. For example, Parmentier et al. (2018) simulate the gas pressure ranging from 200 bar to $2 \mu\text{bar}$, and Helling et al. (2021a) from 0.1 mbar to 700 bar. We began to explore the impact of inner pressure boundary of the GCM on the

formation of clouds for the specific case of hot Jupiter WASP-43 b (Helling et al. 2021a), showing that the increased thermal stability associated with higher pressures permits cloud formation to occur deeper in the atmosphere towards the hotter inner boundary. Here, we address the upper, low pressure boundary of the GCM simulations.

We extrapolate a log-equidistant pressure grid and calculate corresponding temperatures using a parameterisation based on Madhusudhan & Seager (2009). We chose to extrapolate four profiles (substellar and antistellar point, equatorial morning and evening terminators) for on selected exoplanet atmosphere configuration (host star: G5V, $T_{\text{eff}, p} = 1600$ K, $\log_{10}(g) = 3$ [cgs]) to form the basis of the discussion on the potential for cloud formation outside of the commonly used computational domain. The final temperature approached by the temperature parameterisation, $T_{\text{gas,outer}}$, of the substellar extrapolated profiles is 10 000 K following works by García Muñoz (2007); Yelle (2004). The antistellar extrapolated profile has a fixed $T_{\text{gas,outer}} = 100$ K. We note that the exact value of the outermost temperatures do not affect the result presented here since cloud formation stops at lower pressures in both cases because of too high temperatures or too low collision rates. The terminator points are assumed to have an isothermal temperature structure for $p_{\text{gas}} \geq 10^{-3}$ bar where the temperature is fixed to the final value of the original 1D profile. The lowest pressure considered in this extrapolation is 10^{-12} bar. The gas can safely be considered as a neutral hydrodynamic fluid to gas pressures as low as 10^{-8} bar (Appendix A). If the gas can be assumed to be sufficiently ionised (see Sect. 3.4) such that the collisional cross section increases accordingly, the validity shift to lower pressures of 10^{-15} bar. Such low pressures are still not without challenge since they imply very low particle growth rates as well as very little frictional interaction between the cloud particle and the gas. The transition from the original 3D GCM ($T_{\text{gas}}, p_{\text{gas}}$) domain into the extrapolated pressure domain is depicted by the transition from dark grey to light grey solid line in Fig. 15 and occurs at $p_{\text{gas}} \approx 10^{-3}$ bar.

The extended 1D profiles are shown in Fig. 15, and despite the possible crudity of our first-order extrapolation, it becomes clear that the trends of the inner atmosphere with respect to their cloudiness will continue into the upper atmosphere. Figure 15 demonstrates that the atmospheric range where cloud formation is triggered by the formation of condensations seeds (TiO_2 , SiO , KCl , NaCl), extends into the very low pressure range for the terminators and the nightside profile. TiO_2 (dark blue dashed) and SiO (brown dashed) remain the dominating nucleation species. Figure 15 further re-emphasizes that nucleation only occurs if the local gas temperature drops below the temperature where thermal stability (i.e. supersaturation ratio $S = 1$) occurs. This explains the difference in cloud extension between the two terminators with the evening terminator ($\phi = 90^\circ$) being somewhat hotter than the morning terminator. Furthermore, the nightside ($\phi = 180^\circ$) and the morning terminator ($\phi = 270^\circ$) profile probed here could have mineral clouds extending even into higher atmospheric regions where $p_{\text{gas}} < 10^{-12}$ bar.

Figure 16 presents the combined information about the clouds that form beyond the 3D GCM computational domain. The significant increase in the extension of clouds into the low pressure, upper atmosphere ($p_{\text{gas}} < 10^{-4}$ bar) is apparent for the two terminators and antistellar point. Figure 15 shows that the efficient nucleation in the low-pressure, extrapolated atmosphere enables the formation of a layer of mineral hazes in the form of metal oxide clusters and cloud condensation nuclei. The correspondingly low local densities do not enable efficient bulk growth until $p_{\text{gas}} \approx 10^{-8}$ bar (Fig. 16). This suggests that

the observation of these very upper atmospheric regions with $p_{\text{gas}} < 10^{-8}$ bar, which are accessible through high resolution transmission spectroscopy, might allow to study the nucleation process in more detail by searching for the spectroscopic signatures of $(\text{TiO}_2)_N$, $(\text{SiO})_N$ clusters as proposed in Köhn et al. (2021). This mineral haze layer would be expected to be extant to $p_{\text{gas}} \approx 10^{-8}$ bar, below which first mixed-material particles occur. A clear difference in cloud particle sizes may occur between evening and morning terminator due to different nucleation efficiencies. The nightside temperature is the lowest such that the nucleation efficiency is the highest, hence, the cloud particles remain the smallest in these extrapolated, low-pressure atmospheres.

The computational efforts of 3D GCM requires sensible approximations and the assessment of those. Within the hierarchical approach that this paper and Helling et al. (2021a) have followed, it can be concluded that the extension of the derived cloud layers is affected by the location of the inner and the outer boundary of the computational domain. An inner boundary at higher pressures will stabilise the cloud particles such that the cloud's backwarming can stronger affect the temperature in atmosphere-core transition region.

An extended upper boundary allows the mineral cloud formation to contribute in the domain that so far was understood as photochemically driven to form hydrocarbon hazes. This conclusion, however, is based on simulations that did not include the formation of metal-oxide clusters so far. A first comparison of their different efficiency was presented in Helling et al. (2020).

The limitation of our approach is that the simulations are not consistent, instead, the radiation hydrodynamics does not include the cloud formation effects nor the kinetic gas-phase effects. These are clearly topics for future work. It is, however, reasonable to expect that photochemical effects will not only occur for the C/N/O/H/S chemistry but also for the metal-oxide chemistry. Gobrecht et al. (2021) demonstrate, however, that the ionisation energies of $(\text{TiO}_2)_N$ clusters (N being the number of TiO_2 monomers forming the cluster) exceed the atomic ionisation energy of Ti. $(\text{SiO})_N$ is suggested as a better candidate for cluster ionisation but one can only reasonably expect the UV part of the stellar radiation field to affect the ionisation state of these clusters which contribute to the formation of cloud condensation nuclei. We further note that the stability of these clusters may be affected by their fall speed within these low-pressure regimes. The gravitational settling speed is rather high as little frictional interaction occurs. Hence, once such an interaction does occur, the kinetic energy of such interactions will be high.

6. Observational implications

6.1. Transmission Spectroscopy Metric

We calculate a Transmission Spectroscopy Metric (TSM) (Kempton et al. 2018) for each of the grid model planets to give an indication on how amenable the planets would be to transmission spectroscopy observations. The TSM is calculated as

$$\text{TSM} = \text{SF} \cdot \frac{R_p^3 T_{\text{eq}}}{M_p R_*^2} \cdot 10^{-\frac{m_J}{5}} \quad (4)$$

where R_p and M_p are the radius and mass of the planet in Earth units, T_{eq} is the planetary equilibrium temperature in Kelvin, R_* is the radius of the host star, m_J is the apparent magnitude of the host star in the J -band, and SF is a scaling factor.

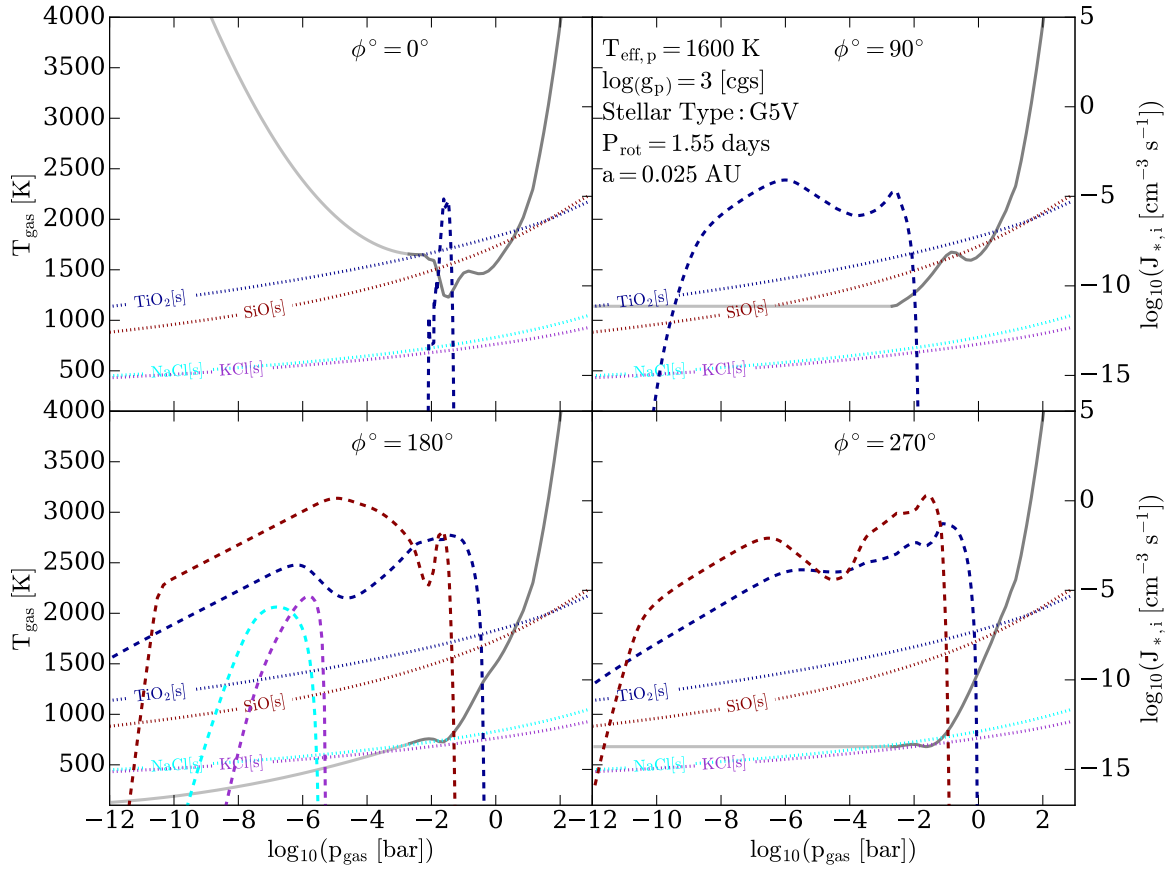


Fig. 15. Nucleation rates, $J_{*,i}$ [$\text{cm}^{-3} \text{s}^{-1}$] (dashed lines), in the extended, low-pressure extrapolated substellar, antistellar, and equatorial morning and evening terminator ($T_{\text{gas}}, p_{\text{gas}}$)-profiles (solid dark grey lines) for the G star planet atmosphere ($T_{\text{eff,p}} = 1600 \text{ K}$, $\log(g) = 3$ [cgs]). The nucleation rates for TiO_2 (dark blue), SiO (brown), KCl (magenta), NaCl (cyan) and the thermal stability curves (supersaturation ratio $S = 1$ for solar element abundances; dotted lines) for their respective solid condensates are shown. The $S_i = 1$ curves do not represent our full kinetic model approach and are provided here for the purpose of visualisation only.

Table 2. J -band magnitudes for stellar types M5V, K5V, G5V and F5V.

Stellar Type	Absolute Magnitude (M_J)	Distance (pc)	Apparent Magnitude (m_J)
M5V	9.09	50	12.58
		100	14.09
		200	15.6
K5V	5.10	50	8.59
		100	10.1
		200	11.61
G5V	3.73	50	7.22
		100	8.73
		200	10.24
F5V	2.52	50	6.01
		100	7.52
		200	9.03

Notes. The absolute magnitudes are taken from [Pecaut & Mamajek \(2013\)](#) and the apparent magnitudes are calculated ($m_J = 5 \log_{10}(d/10 \text{ pc}) + M_J$) for three distances $d = 50, 100, 200 \text{ pc}$.

Whilst the radius of the model planets ($1.35 R_J$) falls outside of the radius bins of the planets analysed by [Kempton et al. \(2018\)](#), we opt to use the scale factor $\text{SF} = 1.15$ calculated for

the $4.0 < R_p < 10 R_E$ range. A J -band (central wavelength $\sim 1.2 \mu\text{m}$) apparent magnitude is used as the wavelength is closest to the centre of the NIRISS bandpass. We calculate the J -band apparent magnitudes of each of the host stars using the absolute magnitudes of [Pecaut & Mamajek \(2013\)](#) for three distances of $d = 50, 100, 200 \text{ pc}$. Both the absolute magnitudes of [Pecaut & Mamajek \(2013\)](#) and the calculated apparent magnitudes are listed in Table 2.

Figure 17 compares the 3D GCM grid TSM with those for various gas-giants and ultra-hot Jupiters. Since the transmission spectroscopy metric $\propto H_p \propto \frac{T}{g}$, planets with high T_{eq} and low $\log(g)$ similar to HD 189733b, HD 209458b but maybe also HATS-6b, WASP-121b and HAT-P-7b are deemed to be easier observable through transmission spectroscopy.

6.2. Where the clouds gets optically thick: the $p(\tau = 1)$ levels

Figure 18 shows the atmospheric gas pressure levels where the optical depth reaches one for $0.1 \dots 100 \mu\text{m}$, $p(\tau(\lambda = 1))$ [bar]. The atmosphere will be blocked by the clouds for higher pressures being equivalent to lower altitudes. For the calculation, we follow the same approach as in [Helling et al. \(2021a\)](#) (Sect. 7). Here, we focus on how the mineral absorption features change for planets within the cool (800 K), transition (1600 K) and the hot (2400 K) exoplanet atmosphere regime for F-type host stars in Fig. 18 which represent the cases shown in Fig. 14. The results for the M, G and K stars are presented in the Appendix (Fig. C.1)

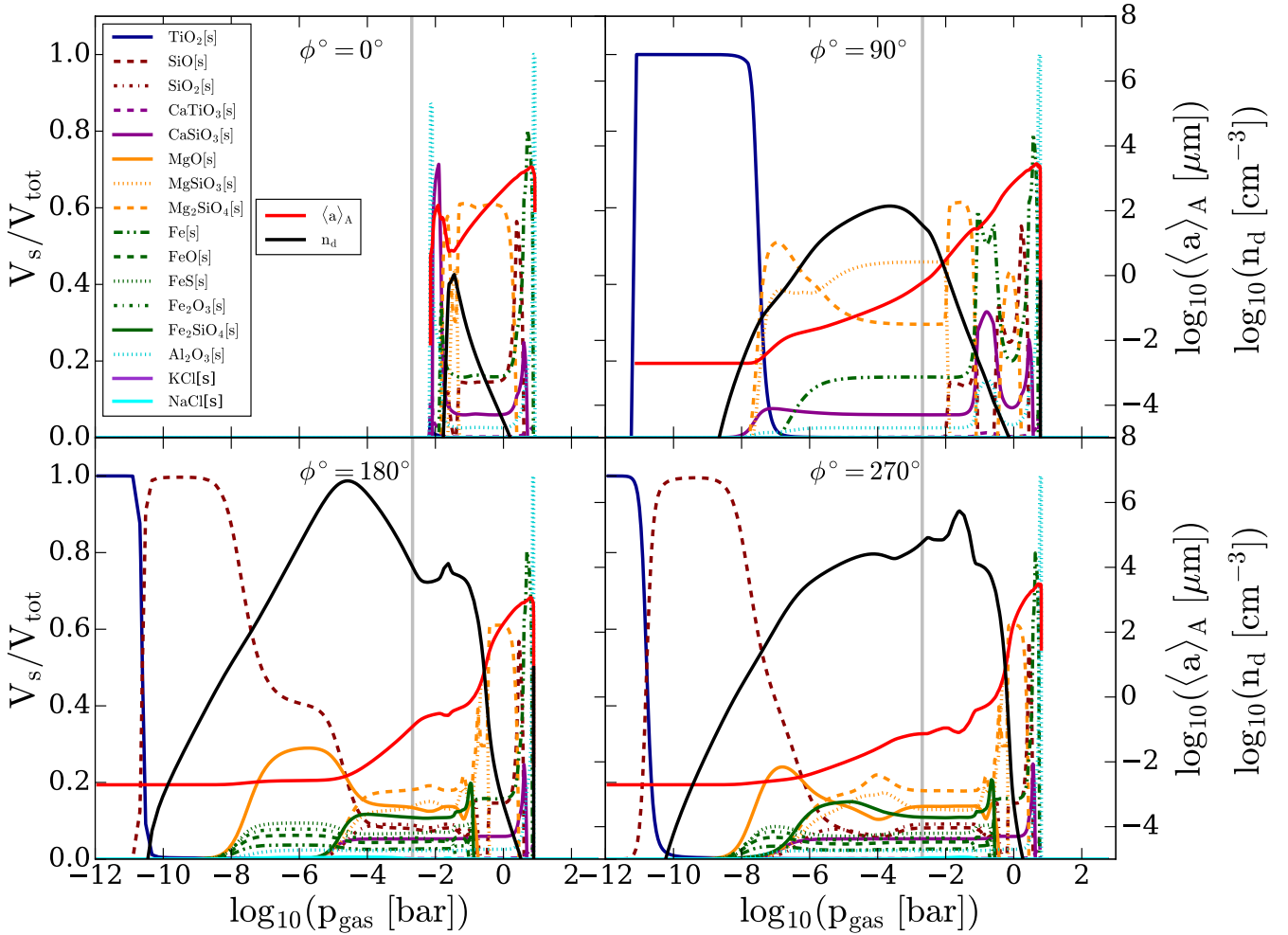


Fig. 16. Material volume fractions (V_s/V_{tot} , color coded), surface averaged mean particle size ($\langle a \rangle_A [\mu\text{m}]$, solid red), and cloud particle number density ($n_d [\text{cm}^{-3}]$, solid black) at the low-pressure extrapolated substellar, antistellar, and equatorial morning and evening terminator points for the G star planet ($\log(g) = 3 [\text{cgs}]$, $T_{\text{eff}} = 1600 \text{ K}$) atmosphere. Both $\langle a \rangle_A$ and n_d use the right-hand axis.

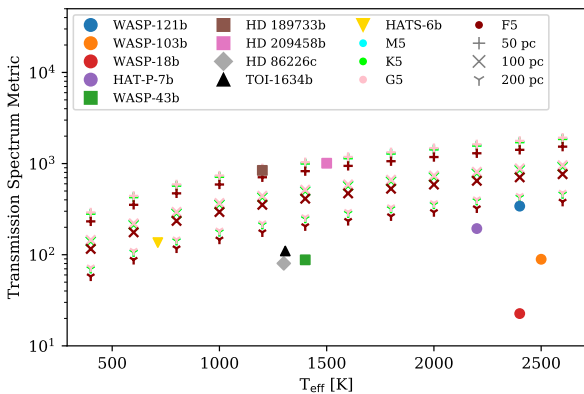


Fig. 17. Transmission spectrum metric (TSM) (Kempton et al. 2018) for selected planets and $\log g = 3 [\text{cgs}]$ grid models. The TSMs for the grid models are calculated using the J-band apparent magnitudes listed in Table 2.

for the those models shown in Figs. 12–14. The comparison of the $p(\tau(\lambda) = 1)$ for different host stars is shown in Fig. 33 in the supplementary catalogue (Lewis et al. 2022). All figures depict the sub-stellar (dayside: $\phi = 0.0^\circ$), the anti-stellar (nightside: $\phi = 180.0^\circ$) and the two terminator profiles (evening: $\phi = 90.0^\circ$; morning $\phi = 270.0^\circ$) at the equator ($\theta = 0.0^\circ$).

The most suitable wavelength region for cloud investigation is $\lambda > 1 \mu\text{m}$. In this region, the silicate features appear and the differentiation between compact and more agglomerate-like cloud particles can be made. The atmosphere becomes optically thick already at the cloud top at shorter wavelength such that the cloud provides a grey background opacity in the optical spectral region. Figure 18 suggest that the nightside would be almost indistinguishable for all three exoplanet regimes, but the considerable differences in the spectral range of the mineral features emerge on the dayside as well as in the terminator regions. The evening terminator, where the hot dayside gas flows towards the nightside, appears particular amenable to distinguish the three regimes.

For the terminators in the mid-infrared the cloud optical depth for all planets is dominated by the silicate spectral features and therefore the profiles are largely indistinguishable for different planetary effective temperatures. However, for the hot exoplanet regime ($T_{\text{eff,p}} = 2400 \text{ K}$) irregularly shaped particles, modelled through a Distribution of Hollow Spheres (DHS, see Min et al. 2005, Samra et al. 2020) appears to produce a flat, higher optically thick cloud pressure level, compared with the compact case. Including a DHS has the effect of increasing the optical depth of clouds in general, although for all other wavelengths and planetary effective temperatures the difference is relatively minor.

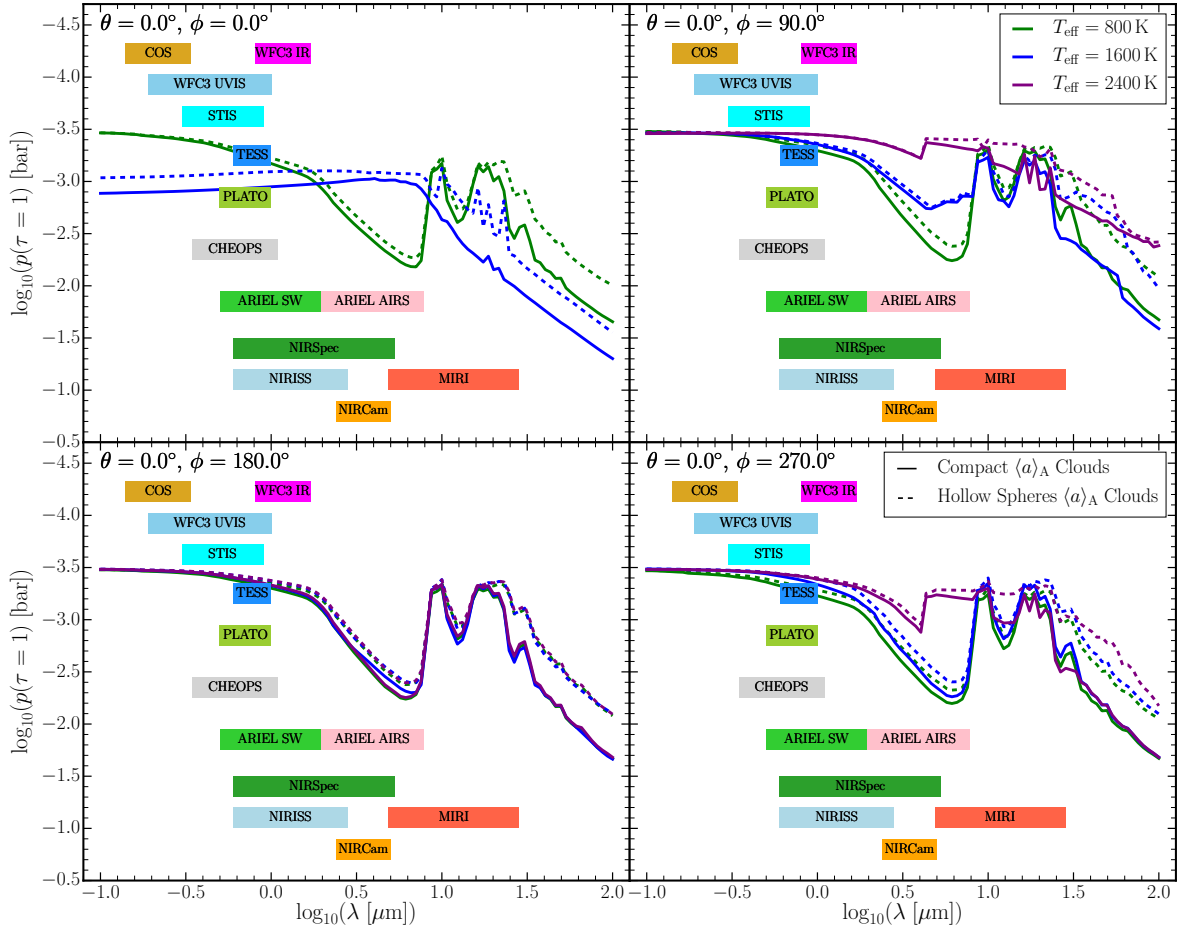


Fig. 18. Wavelength-dependent pressure levels, $p_{\text{gas}} = p(\tau_{\lambda} = 1)$, at which the optical depth due to cloud particles becomes unity, $\tau = 1$, for a grid model planet with an F-type host star, at $T_{\text{eff,P}} = 800, 1600$ and 2400 K, $\log(g) = 3$ [cgs].

It is a different story in the near-infrared, the region covered by JWST NIRSpec and the Ariel infra-red spectrograph (AIRS). In the near-IR are substantial (at greatest an order of magnitude in pressure) differences in the optically thick pressure level of the clouds for different planetary effective temperatures. Phase curve observations were used to infer cloud properties (e.g. [Armstrong et al. 2016](#); [Oreshenko et al. 2016](#); [Stevenson et al. 2017](#); [Cubillos et al. 2021](#)). This provides a good incentive to investigate near-IR phase curves for a wide variety of planetary effective temperatures, as such observations could tease out details of cloud formation as affected by stellar installation and wind flow. Such a survey of phase curves is proposed for Ariel for ~ 50 exoplanets ([Charnay et al. 2022](#)). Furthermore the differences in the optical depth between the near-IR region and the optical may also allow for better constraints on the pressure-temperature structure of these planets, especially for hot gas-giants and transition temperature gas-giants. At such wavelengths, deeper pressure levels are observable, potentially providing information about the local gas temperatures which is unavailable to visible and UV observations. The near-infrared provides a ‘window’ through the clouds to the deeper atmosphere below the observable cloud deck at other wavelengths.

The cloud’s optical depth at the substellar points ($\phi = 0^\circ$) differs dramatically for planet of different global temperatures because hot gas-giants have no clouds at $\phi = 0^\circ$ (case i and iii) and cool gas-giants exhibiting a cloud deck (case i). This strongly affects the dayside albedo. Reflected light observations

of WASP-43b have suggested a dark dayside ([Fraine et al. 2021](#)), and reflected light in visible wavelengths for Kepler-7b have been found to also potentially discriminate between material composition of the clouds ([Webber et al. 2015](#)).

Finally, the effect of the stellar spectral type does also impact these conclusions. For the evening terminator ($\phi = 90^\circ$) of M-type host star planets (Fig. C.1), the cloud optically thick pressure level is dramatically different for the three effective temperatures in the mid-IR. The silicate features are absent for planets in the hot planet regime (case iii).

Figure 19 tests in how far the limit of the computational domain may affect our conclusions regarding the mineral spectra features: $p(\tau(\lambda = 1))$ is compared for the original profile (black and similar to Fig. 18) to results for the extend atmosphere profile (blue) as discussed in Sect. 5. The horizontal thin, red line indicates the upper boundary in pressure space of the 3D GCM computational domain. It can be concluded that the $p(\tau(\lambda = 1))$ -level moves higher into the atmosphere due to cloud particles being able to form higher in the atmosphere and that the feature depth increases around $\lambda \approx 8\mu\text{m}$. The cloud’s optical depth is also affected in the optical and UV by the shifted upper boundary of the computational domain. The $p(\tau(\lambda = 1))$ increases steeper with increasing wavelength until $\lambda \approx 0.6\mu\text{m}$ for the terminators and antistellar points due to the extended cloud decks to higher altitudes (lower pressures) but also due to the smaller average size of the mineral haze at these pressures.

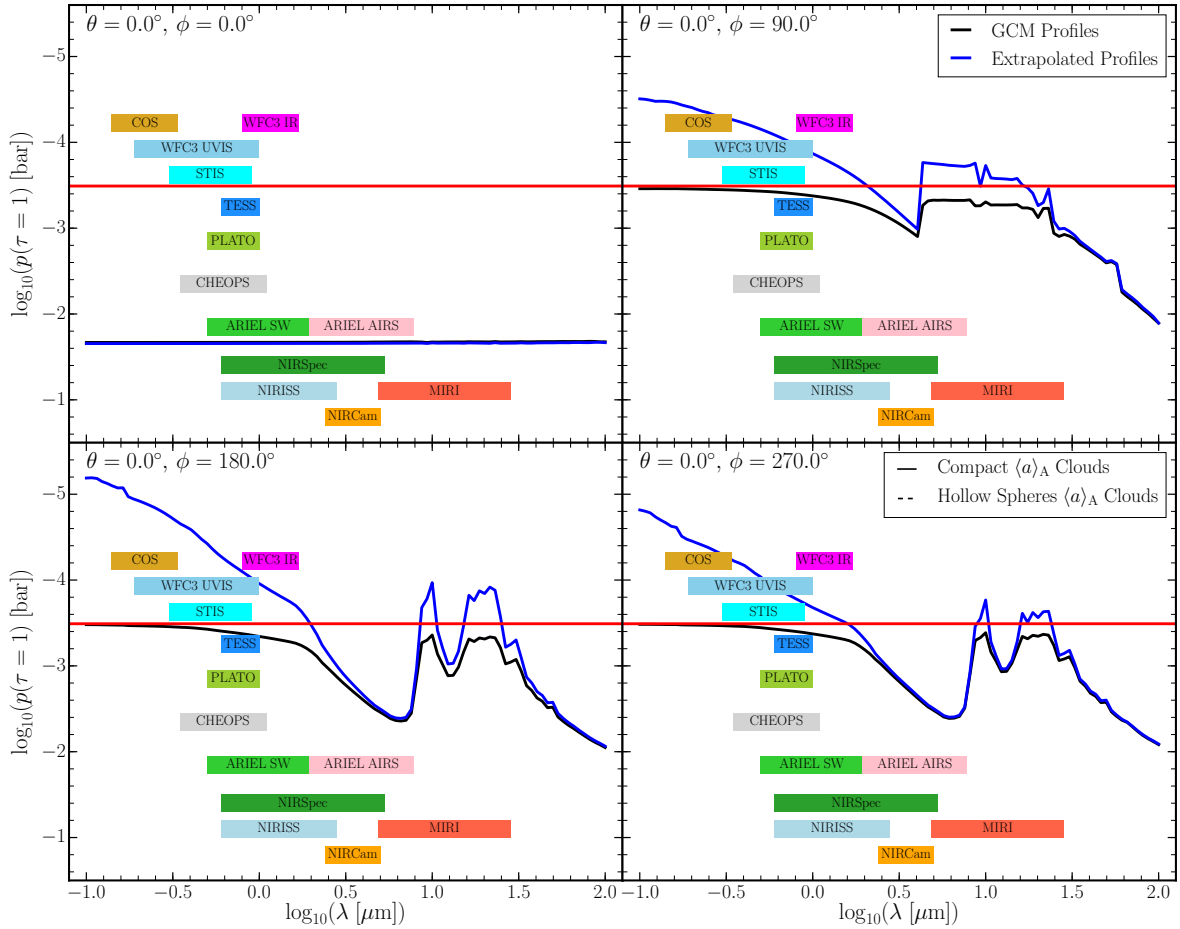


Fig. 19. Wavelength-dependent pressure level, $p_{\text{gas}} = p(\tau_{\lambda} = 1)$, at which the optical depth due to cloud particles becomes unity, $\tau = 1$, for the grid model planet $T_{\text{eff,P}} = 1600$ K, $\log(g) = 3$ [cgs], with a G-type host star. The most suitable wavelength region for cloud investigation is $\lambda > 1 \mu\text{m}$. The solid black lines show the results based on the original 1D profile extracted from the Baeyens et al. (2022) 3D GCM grid, and the blue lines show the results based on the extrapolated profiles. Only the hollow-spheres opacity are shown to demonstrate the maximum effects of the cloud opacity. The horizontal thin, red line indicates the upper boundary in pressure space of the 3D GCM computational domain. The atmosphere becomes optically thick already at the cloud top at shorter wavelength. The horizontal blue line indicates that the cloud is optically thick at $p > 10^{-2}$ bar at the substellar point.

7. Conclusions

We propose to characterise the weather and climate on exoplanets by three classes that exhibit characteristic cloud and gas-phase chemistry with clear implications for atmospheric asymmetries:

- class i) the cool planets ($T_{\text{eff,P}} \leq 1200$ K; e.g., HATS-6b, NGTS-1b) are characterised by:
 - globally homogeneous nucleation, hence, a globally homogeneous cloud coverage,
 - globally depleted element abundances, hence, increasing C/O in cloud forming layers,
 - homogeneous mean molecular weight,
 - globally low thermal ionisation,
 - metal-oxide clusters form a homogeneous haze layer.
- class ii) the transition planets ($T_{\text{eff,P}} = 1400\text{--}1800$ K; e.g., ASP 43b, NGTS-10b, HD 209458b) are characterised by:
 - intermittent nucleation, hence, intermittent cloud coverage,
 - intermittent element depletion and, hence, intermittent C/O across observable planet disk,

- cloud and gas chemistry emphasise day-night terminator difference,
- homogeneous mean molecular weight,
- intermittent increases in thermal ionisation,
- metal-oxide clusters may form mineral hazes on the nightside and on the morning terminator.
- class iii) the hot planets ($T_{\text{eff,P}} \geq 2000$ K; e.g., WASP-18b, WASP-121b, WASP-103b, brown dwarfs similar to WD 0137b and EPIC 2122B) are characterised by:
 - nightside confined nucleation,
 - cloud-free dayside with undepleted element abundances,
 - differences in day-night mean molecular weight implies a larger, geometrical extension of the dayside atmosphere, hence, a strong geometrical day-night asymmetry,
 - dayside exhibits an ionosphere that extends into the high-pressure, inner atmosphere suggesting a highly asymmetric magnetic coupling of these atmospheres,
 - metal-oxide clusters form mineral hazes on the nightside.

We, hence, conclude that for the cool planets (case i), 1D simulations suffice for the atmosphere up to 10^{-5} bar. The homogeneity of the cloud cover suggest that the inferences of the C/O ratio

based on observations of molecules over one planetary location is representative for the whole atmosphere. Combined with the evidence that atmospheric mixing processes homogenize the chemical composition of cool planets (Baeyens et al. 2022), this further means that the non-detection of methane in cool gas planets as inferred from observations of WASP-107b (Kreidberg et al. 2018) (800 K, G type), WASP-117b (800 K, F type) (Carone et al. 2021) and HD 102195 b (800 K, K type) (Gandhi et al. 2020) indeed represent the atmosphere composition and are indicative of methane quenching. Consequently, the presence of multiple carbon and nitrogen bearing species as inferred for HD 209458b (Giacobbe et al. 2021), which lies in the intermediate regime (1400 K, G type), should not be interpreted in the 1D framework to represent the whole planet due to the complex interplay between 3D dynamics, chemistry and cloud formation.

The intermediate temperature regime, not just hot extrasolar planets, may need substantial efforts to treat particularly the cloud distribution in three dimensions, or at the very least, with two profiles for asymmetric terminators for transmission retrieval efforts.

Acknowledgements. Ch.H. and P.W. acknowledge funding from the European Union H2020-MSCA-ITN-2019 under Grant Agreement no. 860470 (CHAMELEON). D.L. and G.H. acknowledge the School of Physics & Astronomy at the university of St Andrews for financial support of the summer project. R.C. acknowledges the Laidlaw Foundation. D.S. acknowledges financial support from the Science and Technology Facilities Council (STFC), UK for his PhD studentship (project reference 2093954). O.H. acknowledges PhD funding from the St Andrews Center for Exoplanet Science. D.S. and O.H. acknowledge financial support from the Österreichische Akademie der Wissenschaften. R.B. acknowledges support from the KU Leuven IDN/19/028 grant ESCHER. L.C. acknowledges the Royal Society University Fellowship URF R1 211718 hosted by the University of St Andrews. K.L.C. acknowledges STFC funding under project number ST/V000861/1.

References

- Ackerman, A. S., & Marley, M. S. 2001, *ApJ*, 556, 872
- Aplin, K. L., Fischer, G., Nordheim, T. A., et al. 2020, *Space Sci. Rev.*, 216, 26
- Armstrong, D. J., de Mooij, E., Barstow, J., et al. 2016, *Nat. Astron.*, 1, 0004
- Baeyens, R., Konings, T., Venot, O., Carone, L., & Decin, L. 2022, *MNRAS*, 512, 4877
- Barth, P., Helling, C., Stüeken, E., et al. 2020, *MNRAS*
- Baxter, C., Désert, J.-M., Parmentier, V., et al. 2020, *A&A*, 639, A36
- Bayliss, D., Gillen, E., Eigmüller, P., et al. 2018, *MNRAS*, 475, 4467
- Beltz, H., Rauscher, E., Roman, M. T., & Guilliat, A. 2022, *AJ*, 163, 35
- Benneke, B., Knutson, H. A., Lothringer, J., et al. 2019, *Nat. Astron.*, 3, 813
- Berger, T. A., Huber, D., Gaidos, E., & van Saders, J. L. 2018, *ApJ*, 866, 99
- Bonomo, A. S., Desidera, S., Benatti, S., et al. 2017, *A&A*, 602, A107
- Borsa, F., Scandariato, G., Rainer, M., et al. 2015, *A&A*, 578, A64
- Bouret, J.-C., Neiner, C., de Castro, A. I. G., et al. 2018, *Proc. SPIE*, 10699, 851
- Burt, J. A., Dragomir, D., Mollière, P., et al. 2021, *AJ*, 162, 87
- Butler, R. P., Marcy, G. W., Williams, E., Hauser, H., & Shirts, P. 1997, *ApJ*, 474, 115
- Butler, R. P., Wright, J. T., Marcy, G. W., et al. 2006, *ApJ*, 646, 505
- Carone, L., Baeyens, R., Mollière, P., et al. 2020, *MNRAS*, 496, 3582
- Carone, L., Mollière, P., Zhou, Y., et al. 2021, *A&A*, 646, A168
- Charnay, B., Bézard, B., Baudino, J. L., et al. 2018, *ApJ*, 854, 172
- Charnay, B., Mendonça, J. M., Kreidberg, L., et al. 2022, *Exp. Astron.*, 53, 417
- Cloutier, R., Charbonneau, D., Stassun, K. G., et al. 2021, *AJ*, 162, 79
- Corrales, L., Ravi, S., King, G. W., et al. 2021, *AJ*, 162, 287
- Cubillos, P. E., Keating, D., Cowan, N. B., et al. 2021, *ApJ*, 915, 45
- Curiel, S., Cantó, J., Georgiev, L., Chávez, C. E., & Poveda, A. 2011, *A&A*, 525, A78
- Cushing, M. C., Roellig, T. L., Marley, M. S., et al. 2006, *ApJ*, 648, 614
- Debrecht, A., Carroll-Nellenback, J., Frank, A., et al. 2020, *MNRAS*, 493, 1292
- Delrez, L., Santerne, A., Almenara, J. M., et al. 2016, *MNRAS*, 458, 4025
- Drummond, B., Mayne, N. J., Manners, J., et al. 2018, *ApJ*, 869, 28
- Evans, T. M., Aigrain, S., Gibson, N., et al. 2015, *MNRAS*, 451, 680
- Fraine, J., Mayorga, L. C., Stevenson, K. B., et al. 2021, *AJ*, 161, 269
- Fuhrmann, K., Pfeiffer, M. J., & Bernkopf, J. 1998, *A&A*, 336, 942
- Gandhi, S., Brogi, M., Yurchenko, S. N., et al. 2020, *MNRAS*, 495, 224
- Gao, P., & Powell, D. 2021, *ApJ*, 918, L7
- García Muñoz, A. 2007, *Planet. Space Sci.*, 55, 1426
- Gaudi, B. S., Seager, S., Mennesson, B., et al. 2020, ArXiv e-prints [arXiv:2001.06683]
- Giacobbe, P., Brogi, M., Gandhi, S., et al. 2021, *Nature*, 592, 205
- Gillon, M., Triaud, A. H. M. J., Fortney, J. J., et al. 2012, *A&A*, 542, A4
- Gillon, M., Anderson, D. R., Collier-Cameron, A., et al. 2014, *A&A*, 562, A3
- Gobrecht, D., Sindel, J. P., Lecoq-Molinos, H., & Decin, L. 2021, *Universe*, 7, 243
- Griffith, C. A., Yelle, R. V., & Marley, M. S. 1998, *Science*, 282, 2063
- Grziwa, S., Gandolfi, D., Csizmadia, S., et al. 2016, *AJ*, 152, 132
- Hartman, J. D., Bayliss, D., Brahm, R., et al. 2015, *AJ*, 149, 166
- Hebb, L., Collier-Cameron, A., Triaud, A. H. M. J., et al. 2010, *ApJ*, 708, 224
- Hellier, C., Anderson, D. R., Collier-Cameron, A., et al. 2009, *Nature*, 460, 1098
- Helling, C. 2019a, *Annu. Rev. Earth Planet. Sci.*, 47, 583
- Helling, C. 2019b, *J. Phys. Conf. Ser.*, 1322, 012028
- Helling, C. 2022, ArXiv e-prints [arXiv:2205.00454]
- Helling, C., & Fomins, A. 2013, *Philos. Trans. Roy. Soc. Lond. A*, 371, 10581
- Helling, C., & Woitke, P. 2006, *A&A*, 455, 325
- Helling, C., Klein, R., Woitke, P., Nowak, U., & Sedlmayr, E. 2004, *A&A*, 423, 657
- Helling, C., Ackerman, A., Allard, F., et al. 2008a, *MNRAS*, 391, 1854
- Helling, C., Woitke, P., & Thi, W.-F. 2008b, *A&A*, 485, 547
- Helling, C., Harrison, R. G., Honary, F., et al. 2016, *Surv. Geophys.*, 37, 705
- Helling, C., Tootill, D., Woitke, P., & Lee, G. 2017, *A&A*, 603, A123
- Helling, C., Iro, N., Corrales, L., et al. 2019, *A&A*, 631, A79
- Helling, C., Kawashima, Y., Graham, V., et al. 2020, *A&A*, 641, A178
- Helling, C., Lewis, D., Samra, D., et al. 2021a, *A&A*, 649, A44
- Helling, C., Worters, M., Samra, D., Molaverdikhani, K., & Iro, N. 2021b, *A&A*, 648, A80
- Herbort, O., Woitke, P., Helling, C., & Zerkle, A. L. 2022, *A&A*, 658, A180
- Hiranaka, K., Cruz, K. L., Douglas, S. T., Marley, M. S., & Baldassare, V. F. 2016, *ApJ*, 830, 96
- Keating, D., Cowan, N. B., & Dang, L. 2019, *Nat. Astron.*, 3, 1092
- Keenan, P. C., & McNeil, R. C. 1989, *ApJS*, 71, 245
- Kempton, E. M. R., Bean, J. L., Louie, D. R., et al. 2018, *PASP*, 130, 114401
- Kennedy, G. M., & Kenyon, S. J. 2008, *ApJ*, 682, 1264
- Köhn, G., Helling, C., Bødker Enghoff, M., et al. 2021, *A&A*, 654, A120
- Komacek, T. D., Showman, A. P., & Tan, X. 2017, *ApJ*, 835, 198
- Kreidberg, L., Line, M. R., Thorngren, D., Morley, C. V., & Stevenson, K. B. 2018, *ApJ*, 858, L6
- Lacy, B. I., & Burrows, A. S. 2020, *A&A*, 641, A123
- Langlois, M., Gratton, R., Lagrange, A. M., et al. 2021, *A&A*, 651, A71
- Lee, J.-M., Heng, K., & Irwin, P. G. J. 2013, *ApJ*, 778, 97
- Lee, G. K. H., Blecic, J., & Helling, C. 2018, *A&A*, 614, A126
- Lee, G. K. H., Casewell, S. L., Chubb, K. L., et al. 2021, *MNRAS*, 496, 4674
- Lee, E. K. H., Lothringer, J. D., Casewell, S. L., et al. 2022a, *MNRAS*, submitted [arXiv:2203.09854]
- Lee, E. K. H., Wardenier, J. P., Prinoth, B., et al. 2022b, *ApJ*, 929, 180
- Lewis, D., Helling, C., Calder, R., et al. 2022, TU Graz repository: <https://graz.pure.elsevier.com/en/publications/the-supplementary-catalogue-exoplanet-weather-and-climate-regimes>
- Libby-Roberts, J. E., Berta-Thompson, Z. K., Désert, J.-M., et al. 2020, *AJ*, 159, 57
- Lines, S., Manners, J., Mayne, N. J., et al. 2018a, *MNRAS*, 481, 194
- Lines, S., Mayne, N. J., Boutle, I. A., et al. 2018b, *A&A*, 615, A97
- Lo Curto, G., Mayor, M., Clausen, J. V., et al. 2006, *A&A*, 451, 345
- Lund, M. B., Rodriguez, J. E., Zhou, G., et al. 2017, *AJ*, 154, 194
- Madhusudhan, N., & Seager, S. 2009, *ApJ*, 707, 24
- Mahapatra, G., Helling, C., & Miguel, Y. 2017, *MNRAS*, 472, 447
- Marley, M. S., Seager, S., Saumon, D., et al. 2002, *ApJ*, 568, 335
- Masuda, K. 2014, *ApJ*, 783, 53
- Maxted, P. F. L., Anderson, D. R., Doyle, A. P., et al. 2013, *MNRAS*, 428, 2645
- May, E. M., Stevenson, K. B., Bean, J. L., et al. 2022, *AJ*, 163, 256
- McCormac, J., Gillen, E., Jackman, J. A. G., et al. 2020, *MNRAS*, 493, 126
- Mendonça, J. M., Tsai, S.-m., Malik, M., Grimm, S. L., & Heng, K. 2018, *ApJ*, 869, 107
- Ment, K., Fischer, D. A., Bakos, G., Howard, A. W., & Isaacson, H. 2018, *AJ*, 156, 213
- Mikal-Evans, T., Sing, D. K., Goyal, J. M., et al. 2019, *MNRAS*, 488, 2222
- Min, M., Hovenier, J. W., & de Koter, A. 2005, *A&A*, 432, 909
- Min, M., Ormel, C. W., Chubb, K., Helling, C., & Kawashima, Y. 2020, *A&A*, 642, A28
- Molaverdikhani, K., Helling, C., Lew, B. W. P., et al. 2020, *A&A*, 635, A31
- Morales, J. C., Mustill, A. J., Ribas, I., et al. 2019, *Science*, 365, 1441
- Morris, B. M., Mandell, A. M., & Deming, D. 2013, *ApJ*, 764, L22
- Neiner, C., Morin, J., Bouret, J.-C., & Fossati, L. 2019, *BAAS*, 51, 219

- Oreshenko, M., Heng, K., & Demory, B.-O. 2016, *MNRAS*, **457**, 3420
- Pál, A. 2009, PhD thesis, Department of Astronomy, Eötvös Loránd University, Hungary
- Parmentier, V., Showman, A. P., & Lian, Y. 2013, *A&A*, **558**, A91
- Parmentier, V., Fortney, J. J., Showman, A. P., Morley, C., & Marley, M. S. 2016, *ApJ*, **828**, 22
- Parmentier, V., Line, M. R., Bean, J. L., et al. 2018, *A&A*, **617**, A110
- Parmentier, V., Showman, A. P., & Fortney, J. J. 2021, *MNRAS*, **501**, 78
- Pecaut, M. J., & Mamajek, E. E. 2013, *ApJS*, **208**, 9
- Perna, R., Heng, K., & Pont, F. 2012, *ApJ*, **751**, 59
- Quanz, S. P., Absil, O., Benz, W., et al. 2021, *Exp. Astron.*, submitted [arXiv:1908.01316]
- Raetz, S., Maciejewski, G., Seeliger, M., et al. 2015, *MNRAS*, **451**, 4139
- Rodríguez-Barrera, M. I., Helling, C., Stark, C. R., & Rice, A. M. 2015, *MNRAS*, **454**, 3977
- Rodríguez-Barrera, M. I., Helling, C., & Wood, K. 2018, *A&A*, **618**, A107
- Roman, M. T., Kempton, E. M. R., Rauscher, E., et al. 2021, *ApJ*, **908**, 101
- Rosenthal, L. J., Fulton, B. J., Hirsch, L. A., et al. 2021, *ApJS*, **255**, 8
- Roth, A., Drummond, B., Hébrard, E., et al. 2021, *MNRAS*, **505**, 4515
- Salz, M., Schneider, P. C., Czesla, S., & Schmitt, J. H. M. M. 2015, *A&A*, **576**, A42
- Samra, D., Helling, C., & Min, M. 2020, *A&A*, **639**, A107
- Samra, D., Helling, C., & Birnstiel, T. 2022, *A&A*, **663**, A47
- Schneider, A. D., Carone, L., Decin, L., et al. 2022, *A&A*, **664**, A56
- Scholz, A., Moore, K., Jayawardhana, R., et al. 2018, *ApJ*, **859**, 153
- Scowen, P. A., Gayley, K., Ignace, R., et al. 2022, *Ap&SS*, **367**, 121
- Seager, S., Petkowski, J. J., Günther, M. N., et al. 2021, *Universe*, **7**, 172
- Sheppard, K. B., Mandell, A. M., Tamburo, P., et al. 2017, *ApJ*, **850**, L32
- Showman, A. P., Tan, X., & Parmentier, V. 2020, *Space Sci. Rev.*, **216**, 139
- Shporer, A., Wong, I., Huang, C. X., et al. 2019, *AJ*, **157**, 178
- Slater, J. C. 1964, *J. Chem. Phys.*, **41**, 3199
- Southworth, J. 2012, *MNRAS*, **426**, 1291
- Southworth, J., & Evans, D. F. 2016, *MNRAS*, **463**, 37
- Stassun, K. G., Collins, K. A., & Gaudi, B. S. 2017, *AJ*, **153**, 136
- Stassun, K. G., Oelkers, R. J., Paegert, M., et al. 2019, *AJ*, **158**, 138
- Steinrueck, M. E., Showman, A. P., Lavvas, P., et al. 2021, *MNRAS*, **504**, 2783
- Stevenson, K. B., Line, M. R., Bean, J. L., et al. 2017, *AJ*, **153**, 68
- Svensmark, H., Enghoff, M. B., Shaviv, N. J., & Svensmark, J. 2017, *Nat. Commun.*, **8**, 2199
- Talens, G. J. J., Justesen, A. B., Albrecht, S., et al. 2018, *A&A*, **612**, A57
- Tan, X., & Komacek, T. D. 2019, *ApJ*, **886**, 26
- Tan, X., & Showman, A. P. 2021, *MNRAS*, **502**, 2198
- Teske, J., Díaz, M. R., Luque, R., et al. 2020, *AJ*, **160**, 96
- Tinetti, G., Eccleston, P., Haswell, C., et al. 2021, *ArXiv e-prints* [arXiv:2104.04824]
- Tomicic, M., Bødker Enghoff, M., & Svensmark, H. 2018, *Atmos. Chem. Phys.*, **18**, 5921
- Torres, G., Winn, J. N., & Holman, M. J. 2008, *ApJ*, **677**, 1324
- Udry, S., Mayor, M., Naef, D., et al. 2000, *A&A*, **356**, 590
- Van Eylen, V., Kjeldsen, H., Christensen-Dalsgaard, J., & Aerts, C. 2012, *Astron. Nachr.*, **333**, 1088
- Vogt, S. S., Wittenmyer, R. A., Butler, P. R., et al. 2010, *ApJ*, **708**, 1366
- Wang, H., & Wordsworth, R. 2020, *ApJ*, **891**, 7
- Webber, M. W., Lewis, N. K., Marley, M., et al. 2015, *ApJ*, **804**, 94
- Witte, S., Helling, C., & Hauschildt, P. H. 2009, *A&A*, **506**, 1367
- Woitke, P. & Helling, C. 2003, *A&A*, **399**, 297
- Woitke, P., & Helling, C. 2004, *A&A*, **414**, 335
- Wong, I., Knutson, H. A., Lewis, N. K., et al. 2015, *ApJ*, **811**, 122
- Yates, J. S., Palmer, P. I., Biller, B., & Cockell, C. S. 2017, *ApJ*, **836**, 184
- Yelle, R. V. 2004, *Icarus*, **170**, 167
- Zhang, X. 2020, *Res. Astron. Astrophys.*, **20**, 099
- Zhou, Y., Apai, D., Tan, X., et al. 2022, *AJ*, **163**, 17

Appendix A: Testing validity of hydrodynamics regime

Here we determine over which pressure range the utilized model atmospheres and their extrapolations are collision dominated, i.e. the fluid assumption is valid. The validity of the hydrodynamic assumption is assessed via the Knudsen number $Kn = \lambda/L$, where λ is the mean free path and L is the characteristic length scale. For the hydrodynamic assumption to be valid, $Kn < 1$. For this model, the characteristic length scale is taken as the scale height. The mean free path can be calculated via

$$\lambda = \frac{1}{\sqrt{2}n\pi d^2} \quad (\text{A.1})$$

where d is the covalent radius of hydrogen: $d_H = 2.25 \times 10^{-12} \text{m}$ (Slater (1964)) and n is the number density of the local gas phase [cm^{-3}]. The scale height is derived from the assumption of hydrostatic equilibrium.

$$H_S = \frac{k_B T}{\mu m_H g} \quad (\text{A.2})$$

where T is the temperature of the local gas phase and $\mu=2.35$ [amu].

Debrecht et al. (2020) point out that the upper atmospheres will be affected by ionisation such that the mean free paths of the gas phase does change. Irradiation by the planet's host star is the most likely cause, but the interstellar radiation may already suffice to ionise the uppermost atmospheric layers (Rodríguez-Barrera et al. 2018).

To determine the Knudsen number limit for the ionised atmosphere, the mean free path is calculated as

$$\lambda = \frac{1}{\sigma n} \quad (\text{A.3})$$

where n is the number density of the local gas phase [m^{-3}] and σ is the cross sectional area [m^2] where $\sigma = 10^{-11}/T^2$ (Debrecht et al. (2020)). Figure A.1 shows the height of the atmosphere as a function of pressure, with vertical lines denoting the pressure at which the Knudsen number exceeds 1 for the molecular and ionised gas.

We also plot the minimum cross sectional area of the gas particles for which the gas is collision dominated throughout the entire pressure regime (ie. the upper pressure limit at which the gas is collision dominated is 3.58×10^{-15} bar) in figure A.3.

Furthermore, we include the collision cross-sectional area ($\sigma = 10^{-11}/T^2$) as a function of pressure in figure A.2.

Appendix B: Diffusive mixing

This appendix motivates a new approach how to measure the mass exchange timescale $\tau_{\text{mix}}(z)$ from the vertical component of a given velocity field $v_z(\mathbf{r}, t)$, where \mathbf{r} is the 3D position and t the time. This approach has been used in all STATICWEATHER models presented in this paper.

Appendix B.1. Mixing and diffusion

Let us assume we have two identical boxes of length Δz with cross section A touching each other, see Fig. B.1. The total

number of a certain kind of molecule in one of those boxes is

$$N = n A \Delta z \quad (\text{B.1})$$

where n [cm^{-3}] is the molecular particle density. From the 3D hydro model, we observe that matter moves up and down with some average (e.g. root-mean-square) velocity [cm/s] as

$$v = v_{z,\text{rms}} = \sqrt{\langle v_z^2 \rangle_t} = \sqrt{\langle v_z^2 \rangle_{\text{vol}}} \quad (\text{B.2})$$

which either involves a long-term average over a suitably long time t or a spatial average over a suitably large volume. Since we are interested in the stochastic part of the velocity field, we assume that there is no bulk motion here, i.e. $\langle v_z \rangle_t = \langle v_z \rangle_{\text{vol}} = 0$. In real application to a given hydrodynamic structure, this means that we first need to subtract the bulk motion before we can apply Eq. (B.2).

Because of the random mixing motions, molecules will go from box 1 to box 2 and vice versa. The associated mean particle fluxes [$\text{cm}^{-2}\text{s}^{-1}$] through the contact area A are

$$j_1 = n_1 v \quad \text{rightwards}, \quad (\text{B.3})$$

$$j_2 = n_2 v \quad \text{leftwards}. \quad (\text{B.4})$$

The change of the total number of molecules N_1 in the left box is

$$dN_1 = -j_1 A dt + j_2 A dt = (n_2 - n_1) v A dt \quad (\text{B.5})$$

$$\Rightarrow \frac{dn_1}{dt} = \frac{n_2 - n_1}{\Delta z} v \rightarrow -\frac{\partial n}{\partial z} v \quad (\text{B.6})$$

Diffusion with rate equations: The problem can be reformulated with rate constants $R = v/\Delta z$ [1/s], like a chemist would do

$$\frac{dn_1}{dt} = -n_1 R + n_2 R \quad (\text{B.7})$$

$$\frac{dn_2}{dt} = -n_2 R + n_1 R \quad (\text{B.8})$$

The mixing timescale: Let us assume box 1 is full, and box 2 initially has none of those molecules. How long would it take to empty box 1? From Eq. (B.7), with $n_2 \rightarrow 0$, we find $n_1(t) = n_1(0) \exp(-t/\tau_{\text{mix}})$ where

$$\tau_{\text{mix}} = \frac{1}{R} = \frac{\Delta z}{v} \quad (\text{B.9})$$

The same result is obtained when considering dN_2 in Eq. (B.5) for the right box

$$\frac{dn_2}{dt} = \frac{n_1 - n_2}{\tau_{\text{mix}}} \quad (\text{B.10})$$

where now index 1 refers to the ‘‘full’’ box, which ultimately provides the supply of fresh condensible material at some distance. In fact, solving the mixing ansatz Eq. (B.10) for the mixing timescale results in

$$\tau_{\text{mix}} = \frac{n_1 - n_2}{\frac{dn_2}{dt}} = \frac{n_1 - n_2}{-n_2 R + n_1 R} = \frac{1}{R} \quad (\text{B.11})$$

for any n_1 and n_2 .

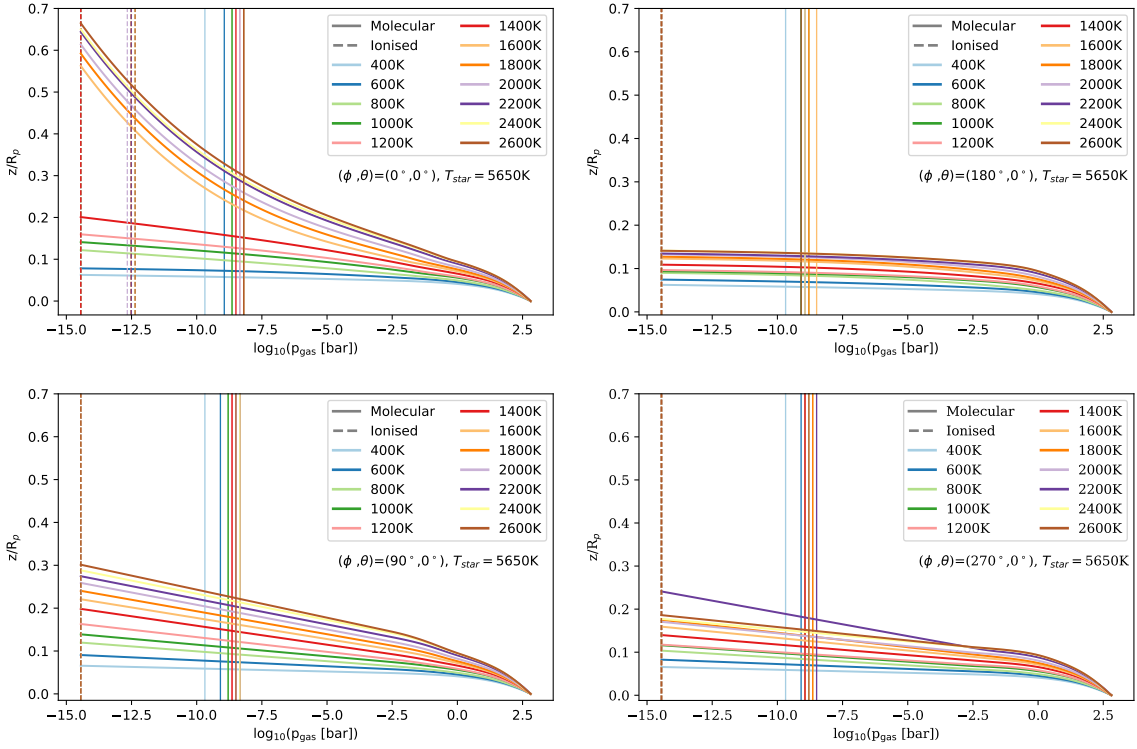


Fig. A.1. Height of the atmosphere as a function of pressure, with vertical lines denoting the pressure at which the Knudsen number exceeds 1. The solid vertical lines show the pressure limit for the molecular gas, and the dashed lines show the pressure limit for the fully ionised gas. The height profiles are shown for all planetary effective temperatures for the sub-stellar, anti-stellar, morning terminator and evening terminator points. All the models have $\log(g)=3$ [cgs] and orbit G5 stars.

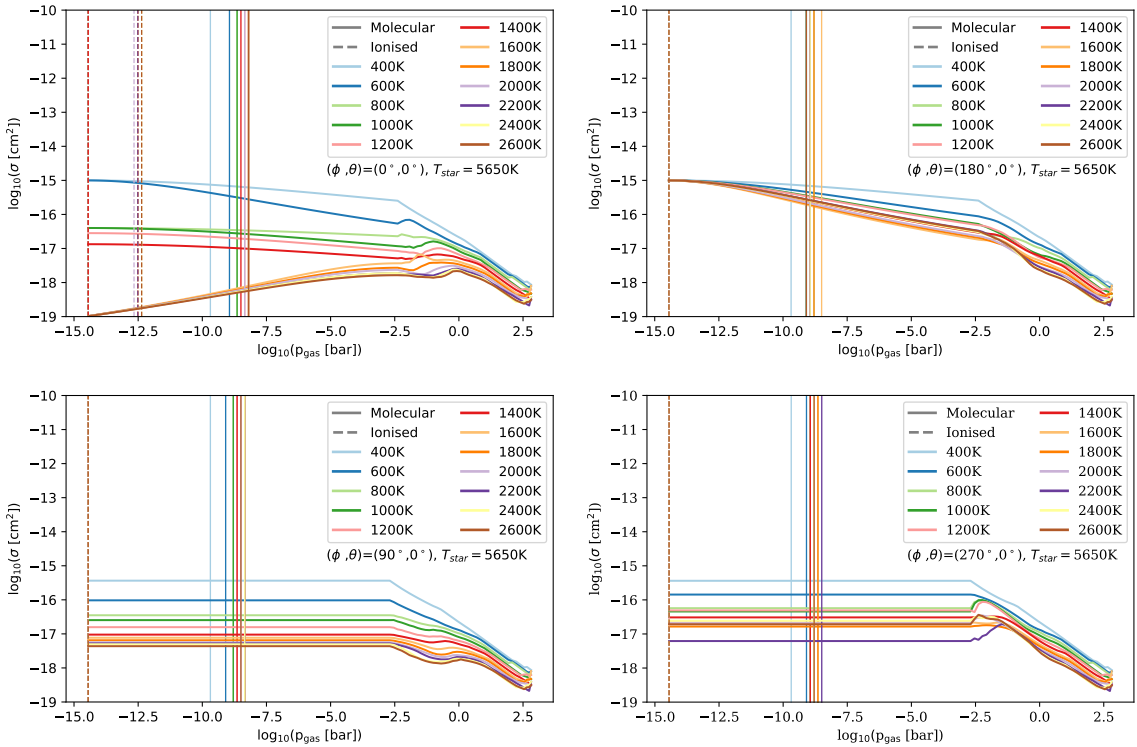


Fig. A.2. Cross sectional area of the gas particles as a function of pressure, with vertical lines denoting the pressure at which the Knudsen number exceeds 1. The solid vertical lines show the pressure limit for the molecular gas, and the dashed lines show the pressure limit for the fully ionised gas. The profiles are shown for all planetary effective temperatures for the sub-stellar, anti-stellar, morning terminator and evening terminator points. All the models have $\log(g)=3$ [cgs] and orbit G5 stars.

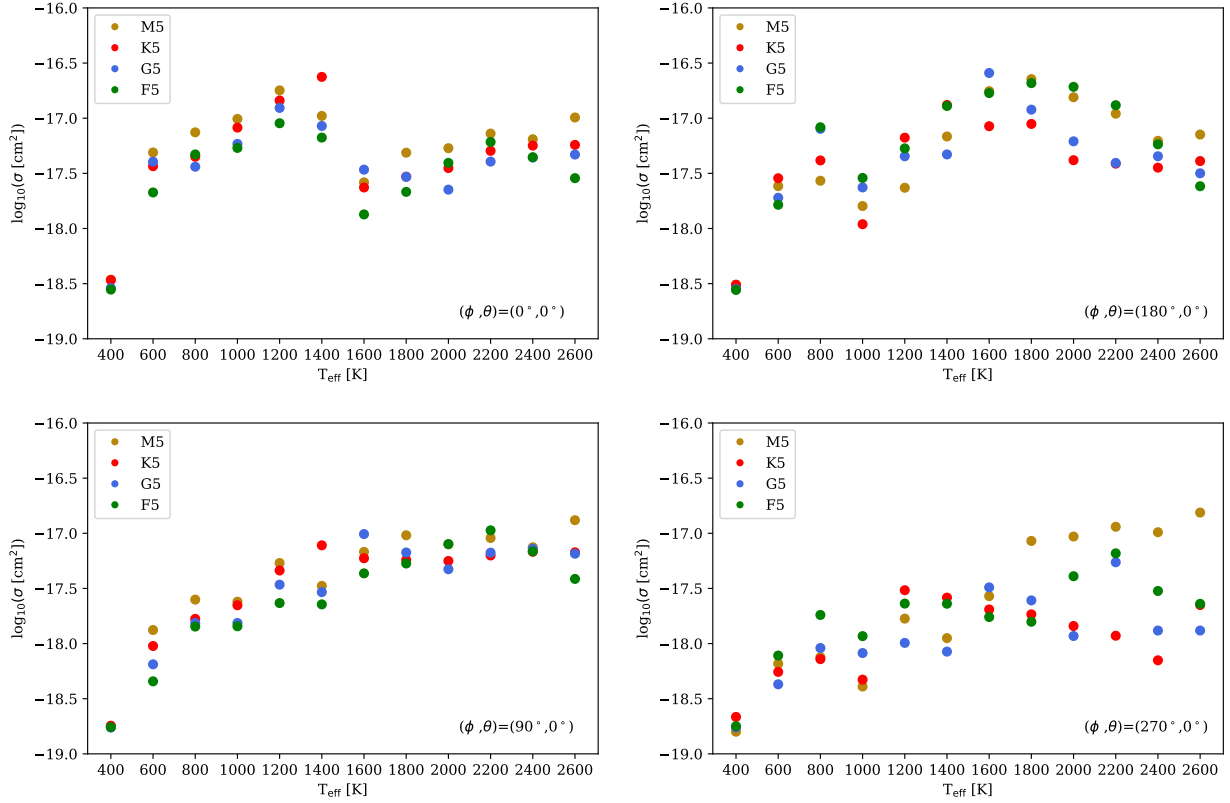


Fig. A.3. Cross sectional area of the gas particles for which the gas is collision dominated throughout the entire pressure regime as a function of planetary effective temperature for each stellar type. Plots are shown for the sub-stellar, anti-stellar, evening terminator and morning terminator points. All models have $\log(g)=3$ [cgs]. Note that this figure is for the uppermost data point only.

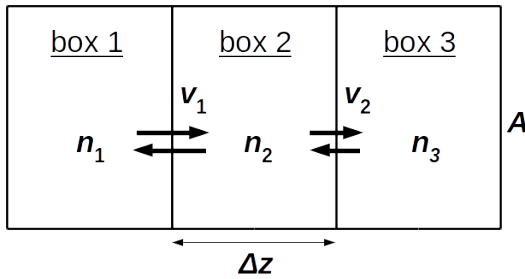


Fig. B.1. Diffusive mixing between three boxes.

Appendix B.2. A linear chain of boxes

Let us now repeat the same thought experiment for 3 boxes in a row as sketched in Fig. B.1. The rate equations in this case, with $R_1 = v_1/\Delta z$ and $R_2 = v_2/\Delta z$ are

$$\frac{dn_1}{dt} = -n_1 R_1 + n_2 R_1 \quad (\text{B.12})$$

$$\frac{dn_2}{dt} = n_1 R_1 - n_2 (R_1 + R_2) + n_3 R_2 \quad (\text{B.13})$$

$$\frac{dn_3}{dt} = -n_3 R_2 + n_2 R_2. \quad (\text{B.14})$$

Closer inspection of Eq. (B.13) shows the analogy to Fick's laws

$$\frac{dn_2}{dt} = \frac{n_1 - n_2}{\Delta z} v_1 + \frac{n_3 - n_2}{\Delta z} v_2 \quad (\text{B.15})$$

$$\rightarrow \frac{\partial}{\partial t} \left(\frac{\partial n}{\partial z} v \right) \Delta z = \frac{\partial}{\partial z} \left(D \frac{\partial n}{\partial z} \right), \quad (\text{B.16})$$

where we find the diffusion constant [cm^2/s] (velocity \times length) to be

$$D = v \Delta z. \quad (\text{B.17})$$

The meaning of Δz is a bit special in Eq. (B.17). The mixing motions typically have a certain intrinsic range ℓ , before the incoming particles actually have an effect on the concentration in the box. When $\Delta z \ll \ell$, those particles simply rush through, there is no time to mix with the ambient gas in the box. In the opposite case, when $\Delta z \gg \ell$, those particles only enrich the regions close to the surface A , but not in the entire box, the concentration gradient on the box is substantial, and that local enhancement at the surface should actually be taken into account when we determine the flux backwards to the originating cell, which we do not. Therefore, the only box thickness where the local Eq. (B.17) actually works fine is when

$$\text{Diffusion:} \quad \Delta z \approx \ell. \quad (\text{B.18})$$

Indeed, when determining diffusion constants, we must always make some assumption about ℓ , for example that ℓ is the mean free path for gas-kinetic diffusion, or ℓ is the scale height H_p for convective mixing.

To find the mixing timescale τ_{mix} for the 3-box experiment, we assume that the concentration n_2 in the sandwich box 2 adjusts quickly to n_1 and n_3 . Setting the time derivative in Eq. (B.13) to zero we find

$$n_2 = \frac{n_1 R_1 + n_3 R_2}{R_1 + R_2}. \quad (\text{B.19})$$

Generalising the derivation of τ_{mix} from the 2-box experiment,

$$\tau_{\text{mix}}^{-1} = -\frac{1}{n_1} \frac{dn_1}{dt} = -\frac{1}{n_1} (-n_1 R_1 + n_2 R_1), \quad (\text{B.20})$$

and using Eq. (B.19) we find

$$\tau_{\text{mix}} = \frac{R_1 + R_2}{R_1 R_2} \frac{1}{1 - n_3/n_1}, \quad (\text{B.21})$$

which, in the limiting case of $n_3 \rightarrow 0$, results in

$$\tau_{\text{mix}} \rightarrow \frac{1}{R_1} + \frac{1}{R_2} = \frac{\Delta z}{v_1} + \frac{\Delta z}{v_2}. \quad (\text{B.22})$$

Again, the same result is obtained when considering the right box (index 3) and using Eq. (B.19)

$$\tau_{\text{mix}} = \frac{n_1 - n_3}{\frac{dn_3}{dt}} = \frac{n_1 - n_3}{-n_3 R_2 + n_2 R_2} = \frac{\Delta z}{v_1} + \frac{\Delta z}{v_2}. \quad (\text{B.23})$$

This thought experiment can be extended to a linear chain of boxes of arbitrary length K . For each chain length, we consider the boundary particle densities n_1 and n_K to be given and assume that $n_2 \dots n_{K-1}$ can be calculated in their stationary limits. This is similar to the Maxwell daemon in nucleation theory, who would always collect the large clusters, break them up into monomers, and return them this way back to the gas phase. Here, we need a daemon who makes sure that n_K stays small, and n_1 stays large. That daemon would quickly transport the molecules arriving in the right box back to the left box, to create a stationary problem with constant diffusive fluxes through all interface areas. In our case, the daemon is dust formation and settling, causing a stationary situation.

Assuming $n_K \rightarrow 0$, the result is

$$\tau_{\text{mix}} = \frac{1}{R_1} + \frac{1}{R_2} + \dots + \frac{1}{R_{K-1}} = \frac{\Delta z}{v_1} + \frac{\Delta z}{v_2} + \dots + \frac{\Delta z}{v_{K-1}}. \quad (\text{B.24})$$

The same result is obtained for the mixing timescale of the right box

$$\tau_{\text{mix}} = \frac{n_1 - n_K}{\frac{dn_K}{dt}} = \dots = \frac{\Delta z}{v_1} + \frac{\Delta z}{v_2} + \dots + \frac{\Delta z}{v_{K-1}}. \quad (\text{B.25})$$

In the limiting case $\Delta z \rightarrow 0$, the final result is

$$\tau_{\text{mix}}(z) = \int_0^z \frac{1}{v(z')} dz', \quad (\text{B.26})$$

which shows that the result is independent of the choice of Δz (disregarding here the uncertainties in the actual numerical computation of that integral). To summarise:

- Equation (B.26) states an expression for the replenishment timescale τ_{mix} in consideration of a distant supply.
- The replenishment timescale is monotonic increasing with z , i.e. it always takes longer to replenish an atmospheric layer which is higher above the ground.
- There can be a bottleneck. If there is a layer between 0 and z where $v(z')$ is particularly slow, all regions above that layer should indeed receive very little mixing supply.
- If $v = \text{const}$, Eq. (B.24) agrees with the 2-box result (Eq. B.9) and the 3-box result (Eq. B.22), namely $\tau_{\text{mix}}(z) = z/v$ which had been used previously in `STATICWEATHER` (case $\beta = 1$).

Appendix C: Miscellaneous figures

We provide the optical depth plots for all host star classes for completeness in Figure C.1. Tables C.1 and C.2 list a selection of potentially favourable targets for a UV mission. The targets are selected based on being gas giant exoplanets with a host star effective temperature close to or hotter than that of the sun. The grid models of this work with host stars of F5 ($T_{\text{eff}} = 6500$ K) or G5 ($T_{\text{eff}} = 5650$ K) type are thus most applicable to such potential future UV missions.

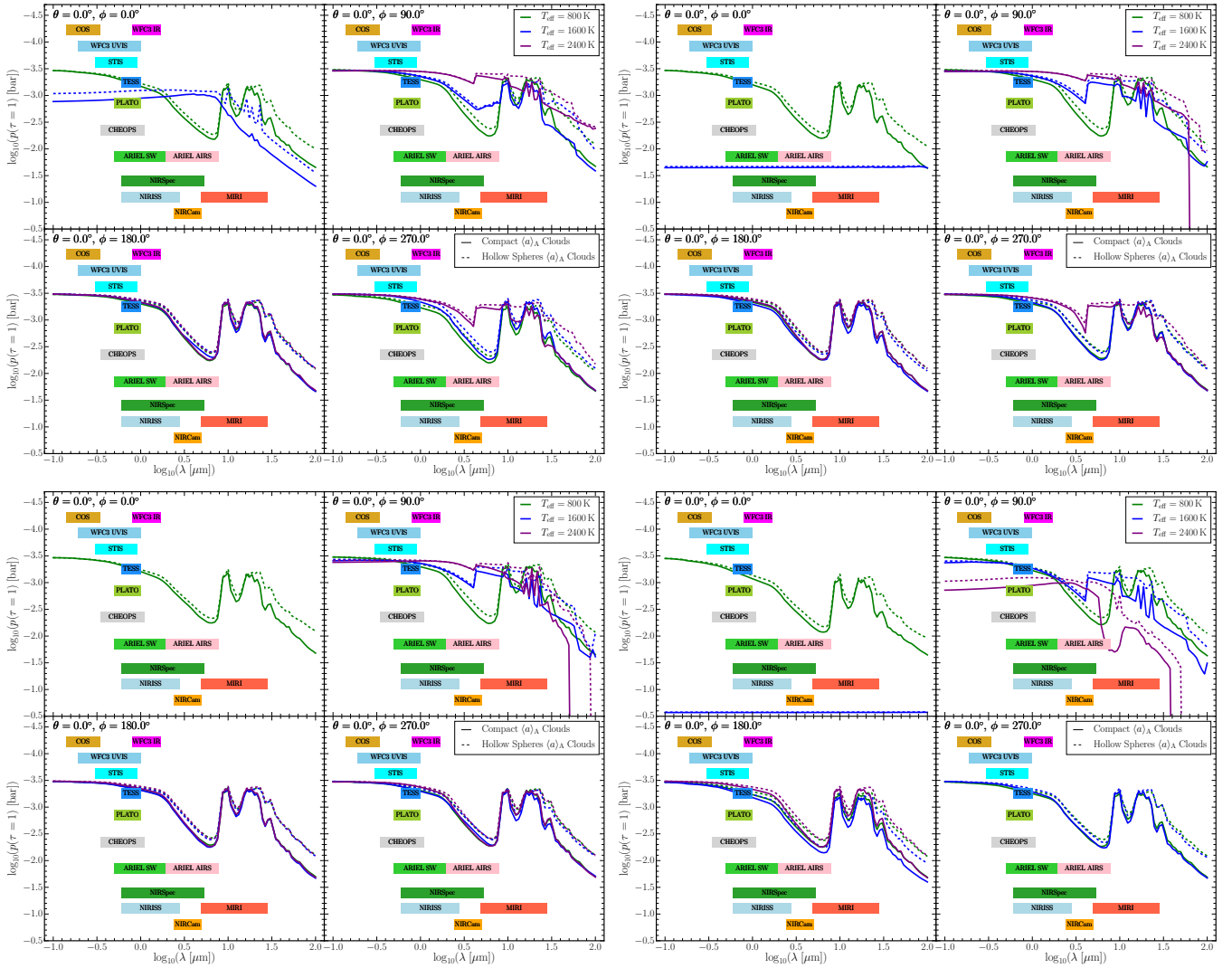


Fig. C.1. Wavelength-dependent pressure level at which the optical depth due to cloud particles becomes unity, $\tau = 1$, i.e. $p_{\text{gas}} = p(\tau_{\lambda} = 1)$, for a grid model planet with Upper Left: an F-type host star, Upper Right: a G-type host star, Lower Left: a K-type host star, and Lower Right: an M-type host star, each at $T_{\text{eff},p} = 800, 1600$ and 2400 K, $\log(g) = 3$ [cgs]

Table C.1. Physical and orbital parameters of potentially favourable exoplanet targets for a UV mission. The density, surface gravity and $\log_{10}(g)$ were calculated (alongside their respective errors) for each planet based on the mass and radius. All planets marked with * have $M_{\text{sin}(i)}$ instead of M . Planets marked with ** had their $T_{\text{eff,P}}$ calculated from Equ. 12 from Baeyens et al. (2022), with $A_B=0$ and $f=2$. Table C.2 list the corresponding host star parameters.

Planet	a [AU]	P [days]	$T_{\text{eff,P}}$ [K]	M_P [M_{Jup}]	R_P [R_{Jup}]	$\rho_{P,\text{bulk}}$ [g cm^{-3}]	$\log_{10}(g)$ [cm s^{-2}]
ups And b	0.05922166±0.00000020	4.617033±0.000023	1837 ⁺⁴⁶ ₋₆₃ **	0.6876±0.0044*			
tau Boo A b	0.049±0.003	3.3124568±0.0000069	1997 ⁺¹⁸⁶ ₋₁₈₉ **	4.32±0.04*			
61 Vir b	0.050201±0.000005	4.2150±0.0006	1397±44 **	0.016±0.002*			
51 Peg b	0.0527±0.0030	4.230785±0.000036	1557 ⁺¹⁴⁹ ₋₂₁₃ **	0.472±0.039*			
HD 179949 b	0.0443±0.0026	3.092514±0.000032		0.916±0.076*			
HD 75289 b	0.050±0.000*	3.509270±0.000064	1260	0.49±0.03*			
KELT-20 b	0.057±0.006	3.474119 ^{+0.000005} _{-0.000006}	2260±50	17	1.83±0.07		
HD 209458 b	0.04707 ^{+0.00045} _{-0.00047}	3.52474859±0.00000038	1484±18	0.682 ^{+0.014} _{-0.015}	1.359 ^{+0.016} _{-0.019}	0.3603 ^{+0.0104} _{-0.0118}	2.9807 ^{+0.0264} _{-0.0296}
HD 212301 A b	0.030±0.000	2.24571±0.00028	2195 ⁺²¹⁷ ₋₂₃₅ **	0.51±0.04*	1.07		
HD 149143 b	0.0530±0.0029	4.07182±0.00001	1756±285 **	1.33±0.15*			
HAT-P-7b	0.03813±0.00036	2.204737±0.000017	2733±21	1.806±0.036	1.510±0.020	0.6956±0.0211	3.3121±0.0274
WASP-18b	0.02087±0.00068	0.9414526 ^{+0.0000016} _{-0.0000015}	2413±44	10.4	1.191±0.038	8.163	4.279
WASP-103b	0.01985±0.00021	0.9255456±0.0000013	2489 ⁺⁶⁶ ₋₆₅	1.455 ^{+0.090} _{-0.091}	1.528 ^{+0.073} _{-0.047}	0.5408 ^{+0.0559} _{-0.0444}	3.2079 ^{+0.0916} _{-0.0762}
WASP-121b	0.02544 ^{+0.00049} _{-0.00050}	1.27492550 ^{+0.00000020} _{-0.00000025}	2720±8	1.183 ^{+0.064} _{-0.062}	1.865±0.044	0.2418 ^{+0.0164} _{-0.0161}	2.945 ^{+0.0636} _{-0.0621}

References: *ups And b*: Curiel et al. (2011), Stassun et al. (2019), Fuhrmann et al. (1998); *tau Boo A b*: Butler et al. (1997), Stassun et al. (2019), Borsa et al. (2015); *61 Vir b*: Vogt et al. (2010); *51 Peg b*: Butler et al. (2006), Keenan & McNeil (1989), Rosenthal et al. (2021); *HD 179949 b*: Butler et al. (2006), Rosenthal et al. (2021); *HD 75289 b*: Stassun et al. (2017), Udry et al. (2000); *KELT-20 b*: Talens et al. (2018); *HD 209458 b*: Bonomo et al. (2017), Evans et al. (2015), Stassun et al. (2017); *HD 212301 A b*: Stassun et al. (2017); *HD 149143 b*: Ment et al. (2018); *HAT-P-7 b*: Bonomo et al. (2017), Stassun et al. (2017), Berger et al. (2018), Morris et al. (2013); *WASP-18b*: Shporer et al. (2019), Salz et al. (2015), Southworth (2012); *WASP-103b*: Gillon et al. (2014), Bonomo et al. (2017), Southworth & Evans (2016); *WASP-121b*: Delrez et al. (2016), Mikal-Evans et al. (2019).

Table C.2. Physical parameters of the exoplanet host stars of potentially favourable targets for a UV mission.

Star	T_{eff} [K]	M_* [M_{\odot}]	R_* [R_{\odot}]	Spectral Type [Fe/H]	Planet
HD 9826	6105.510 ^{+127.253} _{-151.085}	1.150000 ^{+0.164999} _{-0.144399}	1.6364900 ^{+0.1059680} _{-0.0580015}	F8 V	0.09±0.06 ups And b
HD 120136	6466.2700 ^{+115.2650} _{-96.8038}	1.320000 ^{+0.243739} _{-0.184934}	1.4258800 ^{+0.0642849} _{-0.0504688}	F7 V	0.2642300±0.0199902 tau Boo A b
HD 115617	5577±33	0.942 +0.034-0.029	0.963±0.011	G5 V	-0.01 61 Vir b
HD 217014	5758.000 ^{+101.623} _{-119.624}	1.0300000 ^{+0.1666990} _{-0.0854185}	1.1756100 ^{+0.0673608} _{-0.0353276}	G2IV	0.2057±0.0598 51 Peg b
HD 179949	6168	1.21	1.2202±0.0375	F8 V	0.137 HD 179949 b
HD 75289	6117±16	1.29±0.10	1.23±0.02	G0	0.26 HD 75289 b
HD 185603	8980 ⁺⁹⁰ ₋₁₃₀	1.89 ^{+0.06} _{-0.05}	1.60±0.06	A2 V	-0.02±0.07 KELT-20 b
HD 209458	6065±50	1.119±0.033	1.155 ^{+0.014} _{-0.016}	G0 V	0.01 HD 209458 b
HD 212301 A	6239±24	1.55±0.16	1.16±0.02	F8V	0.18 HD 212301 A b
HD 149143	5856	1.20±0.20	1.44±0.08	G0	0.29 HD 149143 b
HAT-P-7	6449±129	1.510 ^{+0.040} _{-0.050}	1.991 ^{+0.084} _{-0.080}	F8	0.260±0.080 HAT-P-7b
WASP-18	6431±48	1.46±0.29	1.26±0.04	F6 IV-V	0.11±0.08 WASP-18b
WASP-103	6110±160	1.220 ^{+0.039} _{-0.036}	1.436 ^{+0.052} _{-0.031}	F8 V	4.22 ^{+0.12} _{-0.05} WASP-103b
WASP-121	6459±140	1.353 ^{+0.080} _{-0.079}	1.458±0.030	F6 V	0.13±0.09 WASP-121b

References: *ups And b*: Curiel et al. (2011), Stassun et al. (2019), Fuhrmann et al. (1998); *tau Boo A b*: Butler et al. (1997), Stassun et al. (2019), Borsa et al. (2015); *61 Vir b*: Vogt et al. (2010); *51 Peg b*: Butler et al. (2006), Keenan & McNeil (1989), Rosenthal et al. (2021), Stassun et al. (2019); *HD 179949 b*: Butler et al. (2006), Rosenthal et al. (2021); *HD 75289 b*: Stassun et al. (2017), Udry et al. (2000); *KELT-20 b*: Talens et al. (2018), Lund et al. (2017); *HD 209458 b*: Bonomo et al. (2017), Evans et al. (2015), Stassun et al. (2017), Stassun et al. (2019); *HD 212301 A b*: Stassun et al. (2017), Lo Curto et al. (2006); *HD 149143 b*: Ment et al. (2018); *HAT-P-7 b*: Bonomo et al. (2017), Stassun et al. (2017), Berger et al. (2018), Morris et al. (2013), Stassun et al. (2019); *WASP-18b*: Shporer et al. (2019), Salz et al. (2015), Southworth (2012), Stassun et al. (2019); *WASP-103b*: Gillon et al. (2014), Bonomo et al. (2017), Southworth & Evans (2016); *WASP-121b*: Delrez et al. (2016), Mikal-Evans et al. (2019), Stassun et al. (2019).